

**Search for Boosted Top-Antitop Quark Resonances in
Muon+Jets Events at 13 TeV Proton-Proton Collisions**

BY

Irving Daniel Sandoval Gonzalez
B.Sc., Instituto Politecnico Nacional, Mexico, 2011

THESIS

Submitted as partial fulfillment of the requirements
for the degree of Doctor of Philosophy in Physics
in the Graduate College of the
University of Illinois at Chicago, 2017

Chicago, Illinois

Defense Committee:

Cecilia E. Gerber, Chair and Advisor
Mark Adams
David Hofman
Corrinne Mills
James Unwin
Dmitri Denisov, Fermi National Accelerator Laboratory

This thesis is dedicated to my parents who are the main reason for this accomplishment. Their unconditional support and love throughout my life are the basis of all my achievements. By example, they taught me that with perseverance, patience, diligence, and dedication, I can succeed in doing anything I set as a goal. I will forever be grateful for all the sacrifices you have made to give me the best opportunities to succeed.

ACKNOWLEDGMENTS

First and foremost, I want to thank my advisor, Prof. Cecilia Gerber, for giving me the opportunity to join her research group since the beginning of my journey in graduate school. Not only was her advice and support a key factor for my professional development, but also her kindness and leadership inspired me to become a better scientist.

Dr. Heriberto Castilla, thank you for believing in me and encouraging me to pursue my postgraduate studies. Your support was immensely valuable.

I would like to thank the NSF-funded projects that financed my research assistantships and allowed me to participate in several workshops, conferences, and summer internships that enormously expanded my knowledge. Thanks to Consejo Nacional de Ciencia Y Tecnologia (CONACYT) for also supporting my studies.

The LHC Physics Center (LPC) at Fermilab provided me a workspace that facilitated a direct collaboration with the leading experts in my field of study, in particular with other members of the CMS collaboration. This was very important for my professional growth.

I am grateful that during my doctoral studies I got to meet dear friends with whom I shared so many learning experiences and who helped me get through challenging times. In particular, Dr. Paul Turner, with whom I shared countless hours in the same office and also several trips. He inspired me to learn more about hardware and to never stop being curious about new technologies. Also, Dr. Inga Silkworth, whom I shared a ride with to Fermilab almost every day. Chatting with her made the hour-long commute enjoyable. She mentored me through new tasks whenever I needed it and was always willing to help.

Finally, I thank my loved ones, who supported me and cheered me up when I needed it the most. Thanks Keaton for being so patient, understanding and caring. Thanks mom for your wise words and advice that each and every time cleared my mind whenever things got blurry. Thanks dad for giving me the strength I needed to continue and finish this journey.

TABLE OF CONTENTS

1	THE STANDARD MODEL OF PARTICLE PHYSICS AND BEYOND	1
1.1	The Standard Model of Particle Physics: Historical Background	1
1.2	The Standard Model of Particle Physics: Mathematical Foundations	3
1.3	Phenomenology	9
1.4	Beyond the Standard Model	11
1.4.1	The Top Quark Importance	13
1.4.2	Kaluza-Klein Gluons In The Randall-Sundrum Warped Extra-Dimension Model	14
1.4.3	Leptophobic Topcolor Z'	16
2	THE ANATOMY OF PROTON-PROTON COLLISIONS	18
2.1	Motivation To Employ Hadron Colliders	18
2.2	Proton-Proton Collisions	20
2.2.1	The Hard Scattering	20
2.2.2	Hadronization	25
3	EXPERIMENTAL SETUP	27
3.1	LHC	27
3.1.1	Accelerating proton beams to 6.5 TeV	29
3.2	The Compact Muon Solenoid (CMS) Detector	31
3.2.1	Tracker	33
3.2.2	Electromagnetic Calorimeter (ECAL)	34
3.2.3	Hadron Calorimeter (HCAL)	36
3.2.4	Superconducting Magnet and Yoke	38
3.2.5	Muon System	39
3.2.6	Trigger System	41
4	PARTICLE RECONSTRUCTION	43
4.1	The Particle Flow Algorithm	43
4.2	Particle Identification	46
4.3	Jets and Missing Transverse Energy Reconstruction	47
5	EVENT CHARACTERIZATION AND SIMULATION	51
5.1	Event Topology	51
5.2	SM backgrounds	53

TABLE OF CONTENTS (continued)

5.3	Simulated Samples	55
6	EVENT SELECTION	60
6.1	Data	60
6.2	Object Definition	60
6.3	Kinematic Event Selection	67
6.3.1	Muon+jets Channel	67
6.4	Corrections to the Simulated Events	68
6.4.1	Pile-up SF	68
6.4.2	Lepton ID SF	68
6.4.3	Trigger SF	69
6.4.4	b -tagging SF	71
6.4.5	top-tagging SF	71
6.5	Kinematic Distributions	73
7	BOOSTED DECISION TREES FOR W +JETS SUPPRESSION	76
7.1	Introduction to Decision Trees	76
7.1.1	Boosted Decision Tree (BDT)	78
7.2	BDT for W +jets Suppression	78
7.2.1	BDT Training, Optimization and Validation	79
7.2.2	BDT performance in Data and MC	84
8	EVENT RECONSTRUCTION AND FINAL BACKGROUND ESTIMATION . . .	88
8.1	Kinematic Reconstruction of the $t\bar{t}$ System	88
8.2	Final Event Selection and Categorization	91
8.3	Sources of Uncertainty and Background Estimation	92
9	STATISTICAL ANALYSIS	100
9.1	Bayesian Probability and Likelihoods	100
9.2	Statistical Modeling	101
9.2.1	Test Statistic	103
9.2.2	Limit Setting	104
9.3	Computation	104
10	RESULTS	106
11	SUMMARY AND OUTLOOK	113
A	RECONSTRUCTION OF THE NEUTRINO'S MOMENTUM	115
B	KINEMATIC DISTRIBUTIONS	117
C	SYSTEMATIC UNCERTAINTY TEMPLATES	125
	CITED LITERATURE	132

VITA	138
----------------	-----

LIST OF TABLES

5.1	SM cross sections (and the order at which they were obtained) of the background processes used in the analysis. The generator packages used to produce these samples are also listed. [69]	57
5.2	Values of the production cross section times branching ratio to $t\bar{t}$. On top, the NLO values for various Z' signal hypothesis with a relative decay widths ($\Gamma_{Z'}/M_{Z'} = 1\%, 10\%$ and 30%) [71], [72]. On the bottom left, the NLO values for the 1% Z' +jet model [36]. On the bottom right, the LO values for KK gluon excitations where the cross sections are multiplied by a factor of 1.3 to account for higher-order corrections [73].	58
6.1	top-mistag rates in data and MC and the corresponding SFs for AK8 jets in the W +jets control sample. The uncertainty is only statistical.	73
7.1	K-S test scores and p-values for the 10 variables used in the BDT for W +jets suppression.	87
8.1	Figure of Merit values for the different working points of the BDT for each of the categories.	92
8.2	List of systematic uncertainties considered in the statistical analysis.	95
8.3	Number of expected background events compared to the observed events in each category. The expected yields have been obtained after the MLE. The reported uncertainties on each background both the statistical error and the posterior uncertainties.	98
10.1	Expected and observed 95% CL lower mass limits for the Z' model with 1% relative widths.	107
10.2	Expected and observed 95% CL lower mass limits for the Z' model with 10% relative widths.	108
10.3	Expected and observed 95% CL lower mass limits for the Z' model with 30% relative widths.	109
10.4	Expected and observed 95% CL lower mass limits for the Z' +jet model.	110
10.5	Expected and observed 95% CL lower mass limits for the KK gluon model.	111
10.6	Expected and observed 95% CL upper mass limits for the three models studied in this analysis.	112

LIST OF FIGURES

1.1	The perturbation series containing some of the possible subprocesses in quark-antiquark scattering	8
1.2	Feynman diagram with loops which give infinite contributions to the perturbation series.	9
1.3	Summary of the fermionic and bosonic fields quanta and their associated quantum numbers and measured masses. Also shown are the interactions among them. [16]	12
1.4	Diagram of the UV and IR branes and the fields propagating through the fifth dimension [29].	15
2.1	Schematic representation of a proton-proton (dark green ovals) collision. The partons interact in an elastic (purple) and inelastic (red) collision. The outgoing partons from such interactions shower and hadronize (light green) [37].	21
2.2	Depending on the energy of the probe, Q^2 , the rich structure of the proton can be resolved [38].	21
2.3	Diagram of the DIS between an electron and a proton.	22
2.4	Parton Distribution Functions obtained in NNLO global analysis at a) $\mu^2 = 10 \text{ GeV}^2$ and b) $\mu^2 = 10^4 \text{ GeV}^2$ with $\alpha = 0.118$ [39].	23
2.5	Diagram of the structure of a generic hard scattering process [40]. Partons a and b interact, represented by the partonic cross section ($\hat{\sigma}$), to produce a new particle. The partonic cross section can be computed via pQCD.	24
2.6	Schematic representations of phenomenological models of hadronization. The string model (left), which treats all but the highest-energy gluons as field lines. These are attracted to each other due to gluon self-interaction and form a string of strong color field. The cluster model (right) assumes that gluons are split non-perturbatively to form color-singlet quark pairs and combinations of these form clusters. [41]	26
3.1	Schematic layout of the LHC accelerator chain. [43]	30
3.2	Schematic layout of the CMS detector.	32
3.3	Schematic cross section of of the CMS tracking system. [44]	33
3.4	Schematic cross section of of the electromagnetic calorimeter. [44]	35
3.5	Schematic cross section of the hadron calorimeter. [44]	37
3.6	Schematic cross section of of the intensity of the magnetic field in the CMS detector. [44]	39

LIST OF FIGURES (continued)

3.7	Layout of one quadrant of the CMS apparatus showing the Muon System and its sub-components. [44]	40
3.8	Schematic of the structure of the L1 trigger system.	41
3.9	Representation of the HLT paths. Starting from the L1 information, a sequence of filter modules and producer modules that reconstruct physics objects select events of interest.	42
4.1	Diagram of the particle flow reconstruction	44
4.2	Nassi-Schneiderman diagram of the structured particle flow identification process	48
4.3	Comparison between the Anti- k_T and k_T algorithms that define a jet [60]	50
5.1	Pie chart that shows the different branching fractions of the top-antitop quark pair. This analysis covers the μ +jets channel (light green), corresponding to about 15% of the branching fraction.	52
5.2	Resolved (left) and boosted (right) topologies of the top-antitop quark decay products. This analysis considers events where jets could be collimated forming "fat" jets and leptons that could be merged within a neighboring jet.	53
5.3	Theoretical predictions and observed cross sections for different SM processes at different \sqrt{s} achieved at the LHC [61].	54
5.4	Invariant mass of the $t\bar{t}$ system at generator level for the signal models considered in the analysis: (a) Z' boson with a relative width of 1%, (b) Z' boson with a relative width of 10%, (c) Z' boson with a relative width of 30%, (d) Kaluza-Klein excitation of a gluon. The distributions are normalized to unity.	59
6.1	CMS integrated luminosity for proton-proton collisions at $\sqrt{s} = 13$ TeV in 2016	61
6.2	Factorized JEC approach where each level of correction takes care of a different effect. The levels of correction are applied sequentially in the shown order.	63
6.3	Diagram of the characteristic parameters used for b -tagging	64
6.4	Hadronic decays of: (a) $t\bar{t}$ and (b) NTMJ dijet events. The cells are colored according to how the jet is divided into three subjets. The square indicates the total jet direction, the circles indicate the two subjets direction and the crosses indicate the three subjet directions. The discriminating variable τ_{32} measures the relative alignment of the jet energy along the crosses compared to the circles [78].	66
6.5	Effect of the Pile-up reweighting on a simulated $t\bar{t}$ sample after the baseline selection has been applied. The distributions have been scaled to the same area to highlight the shape comparison.	69
6.6	Scale Factors applied to the MC samples to take into account differences for the muon ID efficiency. These are given as a function of the muon p_T and η .	70

LIST OF FIGURES (continued)

6.7	Scale Factors applied to the MC samples to take into account differences for the muon HLT efficiency. These are given as a function of the muon p_T and η .	70
6.8	Data/MC distributions for the AK8 jets with $p_T > 500$ GeV and $ \eta < 2.4$. In the CR used for the top-mistag rate measurement: (from top to bottom) jet p_T , jet η , jet mass. Plots for the μ +jets before any top-tagging requirement (after the top-tagging requirements) CR are shown on the left (right). The bottom plot of each figure shows the ratio of data over MC.	72
6.9	Data/MC comparison for (a) muon p_T , (b) muon η , (c) leading jet p_T , (d) leading jet η , (e) sub-leading jet p_T and (f) subleading jet η . The yields of the background processes are normalized to data using scale factors described in 8.2 and the signal MC samples are normalized to a cross section of 1 pb. The shaded band represents the MC statistical uncertainty and the uncertainty on the SM cross section.	74
6.10	Data/MC comparison for (g) p_T^{miss} , (h) jet multiplicity, (i) ΔR_{min} and (j) $p_{T,rel}$. The yields of the background processes are normalized to data using scale factors described in 8.2 and the signal MC samples are normalized to a cross section of 1 pb. The shaded band represents the MC statistical uncertainty and the uncertainty on the SM cross section.	75
7.1	Schematic of a decision tree. This algorithm recursively partitions the data such that the events with the same labels are grouped together.	77
7.2	Separation between background and signal events of the variables used for the BDT training: (a) No. of jets, (b) $\overline{\Delta R_{min}(\ell, j) \times p_T(j)}$, (c) $\overline{\Delta R_{min}(\ell, j)}$, (d) $\overline{p_{T,rel}(\ell, j)}$, and (e) S_{33} . The distributions are normalized to the total number of events of each sample. The variables denoted with a bar are normalized by the mass of the reconstructed $t\bar{t}$ system to avoid introducing a mass bias during the BDT training.	80
7.3	Separation between background and signal events of the variables used for the BDT training: (f) CSV score of leading jet, (g) $\overline{M(j_1)}$, (h) CSV score of sub-leading jet, (i) $\overline{M(j_2)}$, and (j) $\overline{S_T}$. The distributions are normalized to the total number of events of each sample. The variables denoted with a bar are normalized by the mass of the reconstructed $t\bar{t}$ system to avoid introducing a mass bias during the BDT training.	81
7.4	Score map of pairs of hyper-parameters used in the BDT training. On the left, the score is shown as a function of the ada-boost vs. the number of trees. On the right, the score is shown as a function of the minimum samples per leaf vs. the maximum depth per tree.	82
7.5	Schematic of a k -fold validation process. The data is partitioned in k complementary subsets, the training is done in $k - 1$ subsets and then tested on the remaining subset. This process is repeated until each the BDT is tested on each of the k subsets. For each subset, the accuracy of the BDT is measured.	83

LIST OF FIGURES (continued)

7.6	ROC curves for each of the 10 folds use to validate the performance of the BDT. All folds are in agreement with each other, showing a solid BDT training. The mean AUC was found to be 0.95.	83
7.7	BDT classifier output distributions for signal and background events. Compatibility between dots (testing data) and histograms (training data) indicates that overtraining is not a problem.	84
7.8	Data/MC comparison for the variables used in the BDT. The variables denoted with a bar are normalized by the mass of the reconstructed $t\bar{t}$ system. The yields of the background processes are normalized to data using scale factors described in 8.2 and the signal MC samples are normalized to a cross section of 1 pb. The shaded band represents the MC statistical uncertainty and the uncertainty on the SM cross section.	85
7.9	Data/MC comparison for the variables used in the BDT. The variables denoted with a bar are normalized by the mass of the reconstructed $t\bar{t}$ system. The yields of the background processes are normalized to data using scale factors described in 8.2 and the signal MC samples are normalized to a cross section of 1 pb. The shaded band represents the MC statistical uncertainty and the uncertainty on the SM cross section.	86
7.10	Data/MC comparison of the BDT response. The yields of the background processes are normalized to data using scale factors described in 8.2 and the signal MC samples are normalized to a cross section of 1 pb. The shaded band represents the MC statistical uncertainty and the uncertainty on the SM cross section.	87
8.1	Data/MC comparison of the $\chi^2_{t\bar{t}}$ distribution after the baseline selection. The shoulder around 100 is due to events with a failed reconstructed W . The yields of the background processes are normalized to data using scale factors described in 8.2 and the signal MC samples are normalized to a cross section of 1 pb. The shaded band represents the MC statistical uncertainty and the uncertainty on the SM cross section.	90
8.2	Comparison of the expected upper limits on the cross section times branching fraction for a narrow Z' for different BDT working points and categorization options.	93
8.3	Comparison of the expected upper limits on the cross section times branching fraction for a narrow Z' for different $\chi^2_{t\bar{t}}$ thresholds. The limits remain stable, but at higher masses a cut on 30 proves to be the optimal choice. . .	93
8.4	Post-fit values of the nuisance parameters of the background model. The fit parameters are expressed as deviations from their pre-fit values (zero), in units of the corresponding prior uncertainty. The 1σ and 2σ bands of each parameter are shown. On the top left the fit was done using only the SR. On the top right the fit was done using only the CR. On the bottom, both CR and SR were used.	97

LIST OF FIGURES (continued)

8.5	Data/MC comparison of the $M_{t\bar{t}}$ distributions for the 0T (top) and 1T (bottom) categories. The events pass the BDT-T working point and $\chi^2_{t\bar{t}} < 30$. The yields of the background processes are normalized to data using scale factors obtained by the MLE and the signal MC samples are normalized to a cross section of 1 pb. The shaded band represents the MC statistical uncertainty and the uncertainty on the SM cross section.	99
10.1	Expected and observed 95% CL limits on the production cross section times branching ratio of the narrow Z' model.	107
10.2	Expected and observed 95% CL limits on the production cross section times branching ratio of the wide Z' model.	108
10.3	Expected and observed 95% CL limits on the production cross section times branching ratio of the extra-wide Z' model.	109
10.4	Expected and observed 95% CL limits on the production cross section times branching ratio of the Z' +jet model.	110
10.5	Expected and observed 95% CL limits on the production cross section times branching ratio of the KK gluon model.	111
B.1	Data/MC comparison of for events passing the baseline selection, after cutting on the $\chi^2_{t\bar{t}}$ and BDT discriminators. Distributions are shown separately the 0T category (left) and 1T category on the right. The background distributions are obtained from the MLE. The error associated to the background expectation includes the MC statistical uncertainty and post-fit uncertainties on the SM cross sections. The signal templates are normalized to a cross section of 1 pb.	118
B.2	Data/MC comparison of for events passing the baseline selection, after cutting on the $\chi^2_{t\bar{t}}$ and BDT discriminators. Distributions are shown separately the 0T category (left) and 1T category on the right. The background distributions are obtained from the MLE. The error associated to the background expectation includes the MC statistical uncertainty and post-fit uncertainties on the SM cross sections. The signal templates are normalized to a cross section of 1 pb.	119
B.3	Data/MC comparison of for events passing the baseline selection, after cutting on the $\chi^2_{t\bar{t}}$ and BDT discriminators. Distributions are shown separately the 0T category (left) and 1T category on the right. The background distributions are obtained from the MLE. The error associated to the background expectation includes the MC statistical uncertainty and post-fit uncertainties on the SM cross sections. The signal templates are normalized to a cross section of 1 pb.	120

LIST OF FIGURES (continued)

B.4	Data/MC comparison of for events passing the baseline selection, after cutting on the $\chi^2_{t\bar{t}}$ and BDT discriminators. Distributions are shown separately the 0T category (left) and 1T category on the right. The background distributions are obtained from the MLE. The error associated to the background expectation includes the MC statistical uncertainty and post-fit uncertainties on the SM cross sections. The signal templates are normalized to a cross section of 1 pb.	121
B.5	Data/MC comparison of for events passing the baseline selection, after cutting on the $\chi^2_{t\bar{t}}$ and BDT discriminators. Distributions are shown separately the 0T category (left) and 1T category on the right. The background distributions are obtained from the MLE. The error associated to the background expectation includes the MC statistical uncertainty and post-fit uncertainties on the SM cross sections. The signal templates are normalized to a cross section of 1 pb.	122
B.6	Data/MC comparison of for events passing the baseline selection, after cutting on the $\chi^2_{t\bar{t}}$ and BDT discriminators. Distributions are shown separately the 0T category (left) and 1T category on the right. The background distributions are obtained from the MLE. The error associated to the background expectation includes the MC statistical uncertainty and post-fit uncertainties on the SM cross sections. The signal templates are normalized to a cross section of 1 pb.	123
B.7	Data/MC comparison of for events passing the baseline selection, after cutting on the $\chi^2_{t\bar{t}}$ and BDT discriminators. Distributions relevant to the T1 category are shown. The background distributions are obtained from the MLE. The error associated to the background expectation includes the MC statistical uncertainty and post-fit uncertainties on the SM cross sections. The signal templates are normalized to a cross section of 1 pb.	124
C.1	$\pm 1\sigma$ systematic variation on the $M_{t\bar{t}}$ distribution in $t\bar{t}$ MC events. Plots are shown for the two final categories in the muon channel: 1T on the left and 0T on the right. The nominal distribution (black line) is plotted with its statistical uncertainty, the $+1\sigma$ shift up (red) and -1σ shift down (blue) templates account for differences in both shape and normalization with respect to the nominal sample.	126
C.2	$\pm 1\sigma$ systematic variation on the $M_{t\bar{t}}$ distribution in $t\bar{t}$ MC events. Plots are shown for the two final categories in the muon channel: 1T on the left and 0T on the right. The nominal distribution (black line) is plotted with its statistical uncertainty, the $+1\sigma$ shift up (red) and -1σ shift down (blue) templates account for differences in both shape and normalization with respect to the nominal sample.	127

LIST OF FIGURES (continued)

C.3	$\pm 1\sigma$ systematic variation on the $M_{t\bar{t}}$ distribution in $t\bar{t}$ MC events. Plots are shown for the two final categories in the muon channel: 1T on the left and 0T on the right. The nominal distribution (black line) is plotted with its statistical uncertainty, the $+1\sigma$ shift up (red) and -1σ shift down (blue) templates account for differences in both shape and normalization with respect to the nominal sample.	128
C.4	$\pm 1\sigma$ systematic variation on the $M_{t\bar{t}}$ distribution in a narrow 3 TeV Z' MC sample. Plots are shown for the two final categories in the muon channel: 1T on the left and 0T on the right. The nominal distribution (black line) is plotted with its statistical uncertainty, the $+1\sigma$ shift up (red) and -1σ shift down (blue) templates account for differences in both shape and normalization with respect to the nominal sample.	129
C.5	$\pm 1\sigma$ systematic variation on the $M_{t\bar{t}}$ distribution in a narrow 3 TeV Z' MC sample. Plots are shown for the two final categories in the muon channel: 1T on the left and 0T on the right. The nominal distribution (black line) is plotted with its statistical uncertainty, the $+1\sigma$ shift up (red) and -1σ shift down (blue) templates account for differences in both shape and normalization with respect to the nominal sample.	130
C.6	$\pm 1\sigma$ systematic variation on the $M_{t\bar{t}}$ distribution in a narrow 3 TeV Z' MC sample. Plots are shown for the two final categories in the muon channel: 1T on the left and 0T on the right. The nominal distribution (black line) is plotted with its statistical uncertainty, the $+1\sigma$ shift up (red) and -1σ shift down (blue) templates account for differences in both shape and normalization with respect to the nominal sample.	131

LIST OF ABBREVIATIONS

AK	Anti- κ_T
BSM	Beyond the Standard Model
BDT	Boosted Decision Tree
CERN	European Organization for Nuclear Research
CL	Confidence Level
CMS	Compact Muon Solenoid
CR	Control Region
CSC	Cathode Strip Chamber
CSV	Combined Secondary Vertex
CSVM	Combined Secondary Vertex, Medium Working Point
DIS	Deep Inelastic Scattering
DT	Decision Tree
ECAL	Electromagnetic Calorimeter
p_T^{miss}	Missing Transverse Momentum
GSF	Gaussian-Sum Filter
HB	Hadronic Calorimeter Barrel
HCAL	Hadronic Calorimeter
HE	Hadronic Calorimeter Endcap
HLT	High Level Trigger
HO	Hadronic Calorimeter Outer Barrel
ISR	Initial State Radiation
JEC	Jet Energy Correction
JER	Jet Energy Resolution
KK	Kaluza-Klein
L1	Level-1 Trigger
LHC	Large Hadron Collider

LIST OF ABBREVIATIONS (continued)

LO	Leading Order
MVA	Multivariate Analysis
MLE	Maximum-Likelihood Estimation
NLO	Next-to Leading Order
NNLO	Next-to-next-to Leading Order
NTMJ	Non-Top Multi-Jet
PDF	Parton Distribution Function
PF	Particle Flow
pp	proton-proton
pQCD	perturbative QCD
PS	Proton Synchrotron
PSB	Proton Synchrotron Booster
p_T	Transverse Momentum
QCD	Quantum Chromodynamics
QFT	Quantum Field Theory
QED	Quantum Electrodynamics
ROC	Read Out Chip
RPC	Resistive Plate Chamber
SC	Supercluster
SF	Scale Factor
SM	Standard Model
SPS	Super Proton Synchrotron
SR	Signal Region
$t\bar{t}$	top-antitop quark pair
TEC	Tracker End Cap
TIB	Tracker Inner Barrel
TID	Tracker Inner Disk
TOB	Tracker Outer Barrel

SUMMARY

A search for new heavy resonances decaying into top-antitop quark pairs is performed using proton-proton collisions at a center of mass energy of 13 TeV. The datasets correspond to an integrated luminosity of 35.9 fb^{-1} and were recorded by the Compact Muon Solenoid detector at The European Organization for Nuclear Research, CERN. The invariant mass spectrum of the boosted top-antitop quark system is the observable employed to probe the existence of such resonances. The analysis is optimized for events where the top quarks have a large Lorentz-boost resulting in non-isolated leptons and collimated jets from the semileptonic decay of the top quark pairs ($t\bar{t} \rightarrow W^+bW^-\bar{b} \rightarrow q_1\bar{q}_2b\ell\bar{\nu}_\ell\bar{b}$). In particular, only events where the lepton is a muon are considered. The optimization relies mostly in the application of machine learning algorithms and substructure variables that balance background reduction and signal acceptance. The results show that the Standard Model background predictions are in agreement with the observed data. Thus, a Bayesian Statistical Model is applied to set 95% Confidence Level upper limits on the production cross section times branching ratio of the selected two benchmark models; the Randall-Sundrum model that predicts Kaluza-Klein excitation of gluons, and the extended gauge model that predicts the existence of a leptophobic Topcolor Z' .

1. THE STANDARD MODEL OF PARTICLE PHYSICS AND BEYOND

A theory with the goal of reducing all natural phenomena to a finite set of basic laws and predicting experimental observations has been one of the biggest challenges in science. The Standard Model (SM) is, within limitations of our current ability, a consistent and computable theory that has successfully explained most of the observed natural phenomena among fundamental particles. This model has been the closest attempt to achieving such a goal.

In this chapter a historical review, based on [1], of the experimental evidence that led to the development of the model is summarized. Then, based on [2], the mathematical formalism of the model is described. Next, some phenomenological facts are introduced and included in the description of the SM. To finalize, an introduction to the motivation of theories beyond the SM (BSM) is presented and in particular the importance of the top quark in searching for BSM phenomena is emphasized.

1.1 The Standard Model of Particle Physics: Historical Background

Philosophers of ancient times wondered what we and everything around us were made of and how these components interacted with each other. Back in the fifth century BC, Democritus and Leucippus conceived the atomic concept of matter. They postulated that these building blocks of matter would be uncuttable, or as we say these days, fundamental. But it wasn't until the nineteenth century that scientists revisited the concept and gradually established the reality of atoms. The scientific community soon realized that what was before considered fundamental was not; subcomponents of the atom were

discovered. Electrons were first observed by J.J.Thomson, and later on Ernest Rutherford showed that there was also a heavy nucleus. Eventually, with Rutherford's work, it was also confirmed that the nucleus itself is made out of subcomponents: protons and neutrons.

These early atomic experiments revealed a very unexpected richness in the structure of nature that forced physicists to develop more sophisticated theories of the natural world. Max Planck concluded that light is emitted in multiples of a fundamental quantum energy (\hbar), which was later confirmed by experiments corroborating Albert Einstein's explanation of the photoelectric effect. As a consequence Niels Bohr suggested the quantum theory of the atom and then Louis de Broglie made the next major conceptual advance in the evolving quantum theory by proposing the duality of particles and waves. Following De Broglie's ideas, Erwin Schrödinger introduced the particle wave-function. Simultaneously and independently, Werner Heisenberg postulated the uncertainty principle that rules the quantum universe. Having just developed a rather sophisticated picture of the electronic wave-function of the atom, it was soon realized that there was something else missing and so Wolfgang Pauli introduced another quantum number, later on named "spin", and postulated the so-called exclusion principle that categorizes particles into two groups: fermions and bosons. At the same time as Schrödinger and Heisenberg were formulating their respective theories of quantum mechanics, Paul Dirac was attempting the same task; however, he wanted the theory to be consistent with Einstein's special relativity. An immediate consequence of predicting the relativistic relationship between energy and momentum was that his equation allowed the existence of both positive and negative energy particles, the later ones named antiparticles.

Having accepted that a particle can be thought of as a wave-function extending throughout space, introducing the idea that such wave-function corresponds to a particular frequency excitation of a field and may be localized to a greater or lesser extent depending on its interactions was not a great leap. Using the idea of quantum fields, it was then

possible to calculate probabilities of physical processes that could be measured in the laboratory such as particle reaction cross sections, particle lifetimes, etc. It was then turn for Richard Feynman to derive a set of rules that specify the propagation of the fields as the sum of increasingly complex subprocesses involving the quanta of the interacting fields. Each subprocess could be represented in a space-time diagram referred to as a Feynman diagram. The theory that emerged from these rules is known as Quantum Electrodynamics (QED) [3] - [4].

During this physics revolution, it was also observed that there were some new forces in nature beyond the two familiar gravitational and electromagnetic forces. First, it was noticed that a new force must exist in order to bind protons and neutrons within the nucleus and that it should be independent of the electric charge. This new force received the name of "strong force". Later on, the decay of the neutron was experimentally observed and at that point it could not be explained by the known forces, so it was inferred that a different force must exist, the so-called "weak force".

As more experiments became available newer particles started being detected, and an attempt to categorize such a large number of new particles lead to an appreciation of the need for a more fundamental pattern of order. This led to the idea of quarks. To describe their interactions QED was extended to Quantum Chromodynamics (QCD) [5]- [6]. All of these efforts and compilation of theories lead to the development of the SM of particle physics within the Quantum Field Theory (QFT) framework [7].

1.2 The Standard Model of Particle Physics: Mathematical Foundations

Planck's constant (\hbar) and the speed of light (c) are so deeply embedded in the formulation of relativistic QFT that it is standard to set them to unity and so it will be the case from now on. Hence, with this convention, all physical quantities of interest have units which are powers of mass in eV .

Lagrangian Formulation and Symmetries

QFT is the framework employed to describe the interactions of fundamental particles by taking into account their relativistic and quantum-mechanical features. Within this framework all entities are described by fields propagating in a 4-D Minkowski space, therefore, they must have suitable transformation properties under the Lorentz group. The aim of such formulation is to be able to compute probabilities of creation and destruction of the fields' quanta. The first step to achieve this goal is to formulate the mechanisms of interactions between fields. To do so, we are guided by the principle on which all mechanics can be derived: Hamilton's principle. This principle states that the evolution of any system is such that the action, S , of the system is minimized. In Newtonian mechanics, the action is simply given by the time-integral of the Lagrangian, L , of the system, but since we are dealing with fields interacting locally, the system is described through the Lagrangian density \mathcal{L} . Hence, in order to keep the Lorentz invariance of the system we rewrite the action as $S = \int dx^4 \mathcal{L}$.

In the world of physics, symmetries are linked closely to the dynamics of the systems under study, more specifically to invariance under a certain coordinate transformation. For instance; if there is symmetry with respect to time, we know that energy is conserved; when there is symmetry under space translations of the system, linear momentum is conserved; when the system is symmetric under Lorentz boosts, the angular momentum of the system is conserved. Emmy Noether made this connection and stated that for every continuous symmetry of a Lagrangian there is a quantity which is conserved [8]. To express this mathematically, consider the following infinitesimal space-time and gauge transformations:

$$x'^{\mu} = x^{\mu} + \epsilon \frac{\partial x^{\mu}}{\partial \epsilon} + \dots \approx x^{\mu} + \epsilon \tau^{\mu} \quad , \quad \phi' = \phi + \epsilon \frac{\partial \phi}{\partial \epsilon} + \dots \approx \phi + \epsilon \xi, \quad (1.1)$$

where x^μ and τ^μ are coordinate four vectors, and ϕ and ξ are scalar fields, while ϵ is the infinitesimal change. The theorem states that if the action $S = \int dx^4 \mathcal{L}(x^\mu, \phi, \partial^\mu \phi)$ is invariant under the previous infinitesimal transformations and if it is also an extremal, then $\partial_\mu j^\mu = 0$, where j^μ is a Noether current given by

$$j^\mu = \frac{\partial \mathcal{L}}{\partial(\partial_\mu \phi)} \xi + (\partial_\nu \phi \frac{\partial \mathcal{L}}{\partial(\partial_\mu \phi)} - g_\nu^\mu \mathcal{L}) \tau^\nu = p^\mu \xi - T_\nu^\mu \tau^\nu. \quad (1.2)$$

Hence, if the \mathcal{L} describing the theory is invariant under a continuous group of local transformations, or equivalently that there is a conserved Noether current, then the theory is said to be a gauge theory. The interaction of matter fields is described by such gauge theories by imposing local gauge invariance of the type $U(\epsilon) = e^{ig\epsilon(x^\mu)}$, which can be represented by group theory.

The easiest case is when we consider the simplest group, $U(1)$, applicable to QED, a theory for free fermions that automatically requires an interaction term in the Lagrangian density with bosonic fields and whose locally gauge invariant Lagrangian reads:

$$\mathcal{L}_{U(1)} = i\bar{\psi}\gamma^\mu \partial_\mu \psi - m\bar{\psi}\psi - q\bar{\psi}\gamma^\mu \psi A_\mu - \frac{1}{4}F^{\mu\nu}F_{\mu\nu} = \mathcal{L}_{1/2} + \mathcal{L}_1, \quad (1.3)$$

where $F^{\mu\nu} = \partial^\mu A^\nu - \partial^\nu A^\mu$ is the well known Maxwell tensor and A^μ is the needed gauge field to keep gauge invariance. In order to keep the gauge invariance the mass term of the bosonic field, $A^\mu A_\mu$, needs to vanish. We can further associate the terms in the $U(1)$ Lagrangian as follows:

- The first term, $i\bar{\psi}\gamma^\mu \partial_\mu \psi$, corresponds to the kinetic term for the fermionic field.
- The second term, $m\bar{\psi}\psi$, is the fermionic mass term.
- Whereas the third term, $q\bar{\psi}\gamma^\mu \psi A_\mu$, represents the Noether current coupling to the $U(1)$ gauge field.
- Lastly, the fourth term, $\frac{1}{4}F^{\mu\nu}F_{\mu\nu}$, is associated to the kinetic energy of the gauge field.

If we now consider the free Lagrangian density for two interacting matter fields and consider a gauge transformation on them, given by $U = e^{iH} = e^{i\theta} e^{i\vec{\tau} \cdot \vec{\alpha}}$, where τ_i is the i -th Pauli matrix, corresponding to the $U(1) \otimes SU(2)$ group, the Lagrangian density that is locally invariant under $SU(2)$ is given by

$$\mathcal{L}_{SU(2)} = i\bar{\psi}\gamma^\mu\partial_\mu\psi - \bar{\psi}M\psi - q\bar{\psi}(\gamma^\mu\vec{\tau})\psi \cdot \vec{W}_\mu - \frac{1}{4}F^{\mu\nu}F_{\mu\nu}, \quad (1.4)$$

where in this case $F^{\mu\nu} = \partial^\mu\vec{W}^\nu - \partial^\nu\vec{W}^\mu - 2q(\vec{W}^\mu \times \vec{W}^\nu)$ and the \vec{W}^μ are the 3 introduced new vector fields that were needed to keep local invariance. The fact that a cross term, $\vec{W}^\mu \times \vec{W}^\nu$, is present has profound consequences because it means that the gauge fields carry charge and couple to themselves. The essential difference between $U(1)$ and $SU(2)$ is the Abelian structure of the former versus non Abelian group structure of the latter. Notice that this $SU(2)$ Lagrangian has three conserved Noether currents $j_i^\mu = q\bar{\psi}\gamma^\mu\tau_i\psi$, one for each $SU(2)$ gauge field, which in turn correspond to one of the three Pauli matrices of the $SU(2)$ algebra. In the same way as we did with the $U(1)$ Lagrangian, we can describe the terms in the $SU(2)$ Lagrangian as follows:

- The first term, $i\bar{\psi}\gamma^\mu\partial_\mu\psi$, corresponds to the kinetic term for the fermionic fields.
- The second term, $m\bar{\psi}\psi$, is the fermionic mass term.
- Whereas the third term, $q\bar{\psi}(\gamma^\mu\vec{\tau})\psi \cdot \vec{W}_\mu$, represents the Noether current coupling to the $SU(2)$ gauge fields.
- Lastly, the fourth term, $\frac{1}{4}F^{\mu\nu}F_{\mu\nu}$, is associated to the kinetic energy of the gauge fields.

Similarly, for three matter fields, the free QCD Lagrangian that is invariant under a transformation, $U = e^{iH} = e^{i\theta} e^{i\vec{\Lambda} \cdot \vec{\alpha}}$, where Λ_i is the i -th Gell-Mann matrix elements of the $SU(3)$ algebra is given by

$$\mathcal{L}_{SU(3)} = i\bar{\psi}\gamma^\mu\partial_\mu\psi - \bar{\psi}M\psi - q\bar{\psi}(\gamma^\mu\vec{\Lambda})\psi \cdot \vec{G}_\mu - \frac{1}{4}F^{\mu\nu}F_{\mu\nu}, \quad (1.5)$$

where we have introduced the eight new gauge fields, G_μ^1, \dots, G_μ^8 , to keep it locally invariant and in this case, $F^{\mu\nu} = \partial^\mu \vec{G}^\nu - \partial^\nu \vec{G}^\mu - 2q(\vec{G}^\mu \times \vec{G}^\nu)$.

Perturbation Theory

Thus far the interactions of one, two, or three matter fields have been described. In order to represent the destruction and creation of their quanta, one must consider a regime where the magnitude of their interaction is small with respect to the free field Lagrangians. In this perturbative regime, the interaction terms can be treated as small corrections to the free field Hamiltonian, where each subprocess can be represented in a Feynman diagram. These diagrams allow to conceptualize particle interactions: the transitions between initial and final states mediated by the interchange of virtual particles transferring the momentum and quantum numbers at the vertices of the diagram. Each of the possible diagrams represents a term in a perturbation theory expansion of physical amplitudes where the expansion parameter corresponds to the coupling constant, generically denoted by α , associated to the interacting fields. An example of some of the possible quark-antiquark scattering diagrams can be seen in Fig 1.1. To estimate the amplitude, \mathcal{M} , of a process, all of the individual subprocesses expressed in terms of the number of vertices appearing must be added,

$$\mathcal{M} = \sum_i \alpha^i m_i, \quad (1.6)$$

in this notation m_i corresponds to the i -th order diagram. The probability of occurrence P of the physical process under study with initial $|i\rangle$ and final states $|f\rangle$ can be estimated:

$$P = |\langle f | \mathcal{M} | i \rangle|^2. \quad (1.7)$$

This probability may then be restated as the cross section σ of two colliding particles

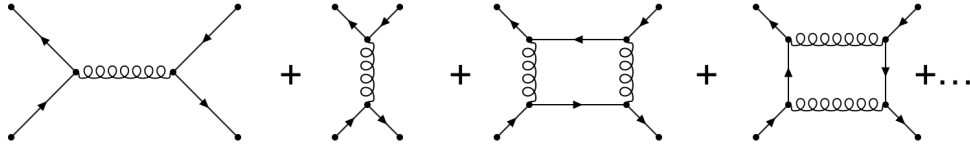


Figure 1.1: The perturbation series containing some of the possible subprocesses in quark-antiquark scattering .

$$\sigma = \int \frac{P}{\Phi} d\Omega, \quad (1.8)$$

where Φ is the scattering-state flux and $d\Omega$ the parameter space where the amplitude was derived.

It should also be pointed out that the dynamics within any subprocess of the individual field quanta of the perturbation expansion are not completely constrained by energy or momentum conservation. This is allowed by Heisenberg's uncertainty principle and is known as a set of virtual processes. They form intermediate states of elementary particle reactions, that despite not being observed, they need to be taken into account and compute their probability of occurrence and add them all up. Fig. 1.2 shows an example of a diagram with virtual loops that would need to be considered to compute second order terms for quark-quark scattering. In 1949, Feynman, Dyson and Tomonaga showed that the infinite contributions of these loops can be cancelled out by a mathematical proof known as renormalization [9]. This is achieved via the so-called "beta function" that encodes the running of a coupling parameter at different energy scales of the given physical process denoted by μ .

$$\beta(\alpha) = \mu \frac{\partial \alpha}{\partial \mu}. \quad (1.9)$$

If the beta function is positive then the coupling increases with energy like in QED. On the other hand, specifically in non-Abelian theories like QCD, the beta function can be negative and, furthermore, it can decrease logarithmically giving rise to a phenomenon called "asymptotic freedom". This will have a special role in Chapter 2 where the anatomy

of proton-proton collisions is described. Conversely, when the coupling increases with decreasing energy then one can no longer rely on perturbation theory.

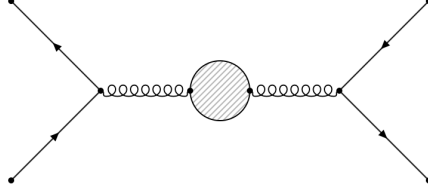


Figure 1.2: Feynman diagram with loops which give infinite contributions to the perturbation series.

Summarizing all of the above, the mathematical formulation can be described as follows: A Lagrangian formulation is employed to specify the form of interaction between the fields and using the variational principle yields to the equations of motion of the fields. The perturbation principle then approximates the equations of motion by a series of Feynman diagrams which show the possible subprocesses between initial and final states involving quanta which can be calculated to estimate the probabilities of physical events such as cross sections or lifetimes of particles, etc.

1.3 Phenomenology

Phenomenology forms a bridge between the Lagrangian formulation of these interacting fields and the experimental observations. For instance, fermionic fields also depend on spin-related Lorentz invariant quantity called chirality [10] and can be expressed as linear combination of their left- and right-handed chirality states

$$\psi = \psi_L + \psi_R. \quad (1.10)$$

Critically, no right-handed neutrinos (left-handed antineutrinos) have been experimentally observed, indicating an apparent chiral asymmetry in nature.

Furthermore, the weak gauge bosons, W_i , not only carry the $SU(2)$ charge but also the $U(1)$ electric charge Q . This implies that weak and electromagnetic interactions mix. Hence, the electromagnetic $U_Q(1)$ generator is constructed from a linear combination of the $SU(2)$ generator τ_3 , and a separate independent $U_Y(1)$ generator Y called hypercharge, such that

$$Q = \tau_3/2 + Y/2. \quad (1.11)$$

Thus, $U_Q(1)$ would be a subgroup of $SU_L(2) \otimes U_Y(1)$. Additionally, these fermionic fields manifest in three generations with identical quantum numbers, each consisting of two leptons and two quarks with identical quantum numbers but with different masses:

$$\begin{bmatrix} u & \nu_e \\ d & e \end{bmatrix}, \begin{bmatrix} c & \nu_\mu \\ s & \mu \end{bmatrix}, \begin{bmatrix} t & \nu_\tau \\ b & \tau \end{bmatrix}.$$

To summarize, the SM is a gauge field theory which is based on the symmetry group $SU_{QCD}(3) \otimes SU_L(2) \otimes U_Y(1)$, where the transformations of the group act on the fields. This group has $8 + 3 + 1 = 12$ generators [11]. The first eight generators correspond to the QCD theory of strong interactions based on the $SU(3)$ group of the color charge. The bosons associated to those generators are the gluons (g), which interact with the matter fields that come in color triples of quarks: red, green or blue (q_R, q_G, q_B). Quarks and gluons are the only fundamental particles that interact through the strong force. The electroweak (EW) interactions are described by the chiral $SU_L(2) \otimes U_Y(1)$ symmetry. Leptons and quarks interact through the electroweak force via the remaining four bosons associated to the last four generators: W^+ , W^- , Z^0 and γ . Because 3 of these bosons are not massless, this symmetry is said to be spontaneously broken to the QED group $U_Q(1)$. To generate masses for these gauge fields, we must introduce a scalar field with a gauge symmetric potential whose ground state is shifted away from the origin of the scalar field. This implies that the ground state must be degenerate. Choosing a peculiar ground state breaks the symmetry, this mechanism was introduced by R. Brout, F. Englert, and P.

Higgs [12], [13], and is known as the “Higgs mechanism”. By introducing this mechanism and the vacuum expectation value, $v \approx 246 \text{ GeV}$ (also called electroweak scale), the mass of the fermions is generated via the Yukawa couplings. Moreover, this mechanism allows flavor mixing among fermions [14]- [15]. The Cabibbo-Kobayashi-Masakawa (CKM) matrix contains information on the strength of these flavor-changing weak decays, where the strong interaction eigenstates are expressed as linear combination of the quarks in the weak eigenstates:

$$\begin{bmatrix} d' \\ s' \\ b' \end{bmatrix} = \begin{bmatrix} V_{ud} & V_{us} & V_{ub} \\ V_{cd} & V_{cs} & V_{cb} \\ V_{td} & V_{ts} & V_{tb} \end{bmatrix} \begin{bmatrix} d \\ s \\ b \end{bmatrix}. \quad (1.12)$$

A summary with the observed bosons and fermions of the SM can be seen in Fig. 1.3.

1.4 Beyond the Standard Model

The discovery of the Higgs boson [17] - [18] at the LHC was a great success of the SM because it was the last missing piece in the puzzle. However, its observed mass is rather unclear as quantum loop-level corrections should have made it much heavier, of the order of 10^{18} GeV (Planck mass). This is known as the “hierarchy problem”. To reconcile this observation, an almost perfect cancellation of the loop-level corrections with the tree-level contributions, also called “fine-tuning”, is required.

Moreover, the following are reasons why the SM is believed to be incomplete:

- The fact that there is a mass gap of at least 6 orders of magnitude among the fundamental particles.
- The observation of neutrino oscillations.
- It does not incorporate gravity.
- The existence of dark matter and dark energy.
- It does not provide an answer to the strong CP problem in QCD.

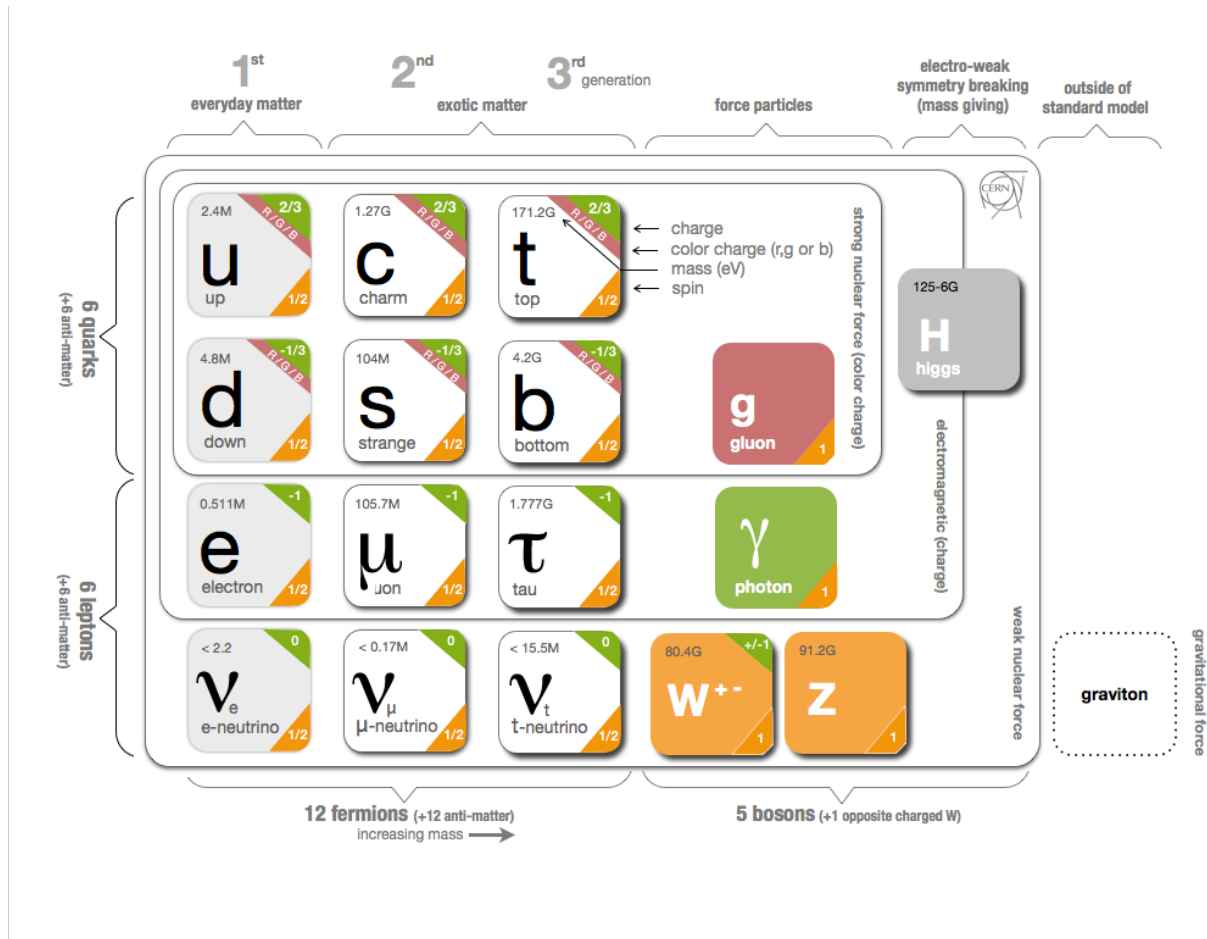


Figure 1.3: Summary of the fermionic and bosonic fields quanta and their associated quantum numbers and measured masses. Also shown are the interactions among them. [16]

1.4.1 The Top Quark Importance

The top quark holds promise in revealing physics BSM due to its very peculiar properties, such as:

- Top quark loops are the largest contributions to the quadratic divergence of the SM Higgs mass, since it has the largest Yukawa couplings among fermions.
- Its mass is remarkably close to the EW scale, $m_t = 173.34 \pm 0.76 \text{ GeV} \approx v/\sqrt{2}$ [19].
- The dominant decay channels for a top quark will be through the weak charged currents, with the partial width given by

$$\Gamma(t \rightarrow W^+ q) = \frac{|V_{tq}|^2 m_t^3}{16\pi v^2} \left(1 - \frac{M_W^2}{m_t^2}\right)^2 \left(1 + 2\frac{M_W^2}{m_t^2}\right) \left[1 - \frac{2\alpha_s}{3\pi} \left(\frac{2\pi^2}{3} - \frac{5}{2}\right)\right], \quad (1.13)$$

where the subsequent decay of W to the final state leptons and light quarks is well understood.

- Also, since $|V_{tb}| \gg |V_{td}|, |V_{ts}|$, the top-quark will predominantly decay into a b-quark.
- And perhaps the most significant aspect of the decay is that

$$\Gamma(t \rightarrow W^+ q) \approx 1.5 \text{ GeV} \approx \frac{1}{0.5 \times 10^{-24} \text{ s}} > \Lambda_{QCD} \approx 200 \text{ MeV}, \quad (1.14)$$

which implies that the top quark will promptly decay via the electroweak interaction before QCD sets in for hadronization, meaning that no SM hadronic bound states would be observed.

The most striking signal for new physics in the top-sector could be via the resonant production of a heavy intermediate state, $X \rightarrow t\bar{t}$. Examples of such heavy resonances include pseudoscalar Higgs bosons [20], new gauge bosons [21]- [22], Kaluza-Klein excitations of gluons and gravitons [23]- [24], Technicolor-like dynamical states [25], etc. Analyses at the LHC have searched for these resonances, in particular the most recent

ones by CMS [26] and ATLAS [27], and have set sub-picobarn limits on the production cross section times branching ratio in the mass ranges of 0.5 and 4 TeV for the Topcolor Z' and KK gluons. These two models are chosen as benchmark models in this thesis and will be described in further detail below.

1.4.2 Kaluza-Klein Gluons In The Randall-Sundrum Warped Extra-Dimension Model

The Randall-Sundrum I (RS1) model [28] is a higher-dimensional mechanism that was designed for solving the hierarchy problem where the weak scale is generated from a large scale of order of the Planck scale through an exponential hierarchy. The framework of this model involves a slice of the AdS_5 space which can be summarized as a 5-D Lorentzian space whose fifth dimension is compact, such that the metric is the known four-dimensional metric multiplied by a warp factor which rapidly changes as a function of the fifth dimension:

$$ds^2 = e^{-2kr_c y} \eta_{\mu\nu} dx^\mu dx^\nu + r_c^2 dy^2, \quad (1.15)$$

where k is a scale factor of the order of Planck's scale, x^μ are the familiar four dimensions, while $0 \leq y \leq \pi$ is the coordinate for the 5th dimension which is a finite interval whose size is set by the compactification radius r_c and $e^{-2kr_c y}$ is the warp factor. Due to the warp factor, the relationship between the 5-D and 4-D mass scales depends on the location in the extra dimension. At $y = 0$ the high energy density "UV/Planck" brane is localized, whereas the low energy density IR/TeV brane is at $y = \pi$. The metric described above can be explained due to the energy differential between these two branes that gravitationally warps the bulk space as seen in Fig.1.4.

Given these spacetime dynamics the fermion mass hierarchy can be explained by allowing the SM fields to propagate along the extra dimension, and we can generically write the field as

$$\psi(x^\mu, y) = \sum_n^\infty \psi_n(x^\mu) f^n(y). \quad (1.16)$$

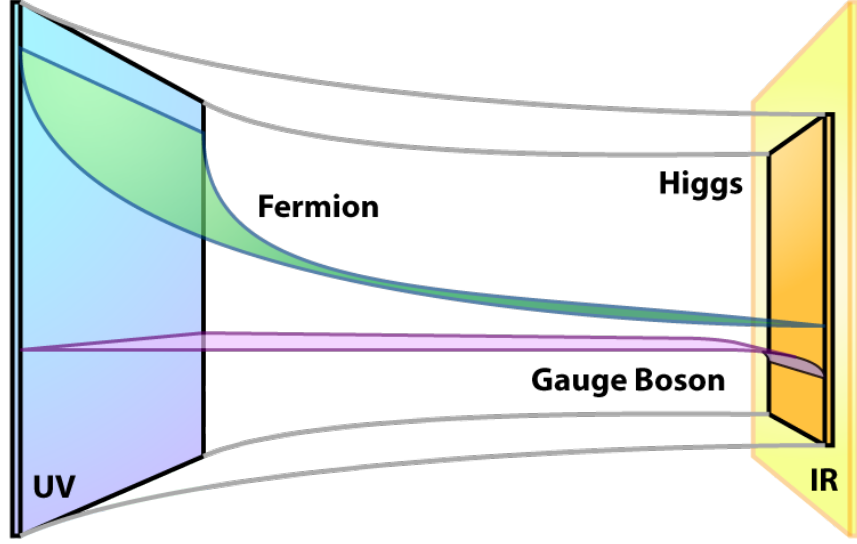


Figure 1.4: Diagram of the UV and IR branes and the fields propagating through the fifth dimension [29].

It should be noted that the geometry of the fifth dimension imposes boundary conditions, similar to the quantum-mechanical particle in a box, on the fifth dimensional component of the bulk wave-functions, $f^n(y)$, where only discretized momentum states are allowed. By integrating over the fifth dimension we obtain the SM Lagrangian augmented by an infinite number of successively more massive copies of the bulk fields. These are called Kaluza-Klein (KK) modes. An additional consequence of this model with warped geometry is that the four momentum is not conserved and so the number of KK-modes can vary in time.

The lightest KK excitations are those of the gauge bosons. Of these, the KK gluons (g_{KK}), because of their larger couplings, are the most interesting to analyze and searches for these are likely to be the most promising probes [30]. Furthermore, they couple predominantly to the right-handed top-quark and, consequently, the branching ratio is more than 90% for $g_{KK} \rightarrow t\bar{t}$.

At leading order the g_{KK} production takes place via annihilation of light quarks, to which the coupling of the g_{KK} is suppressed. Thus, the cross section is small especially

since electroweak precision constraints require the mass of the g_{KK} to be no less than $2 - 3 \text{ TeV}$.

1.4.3 Leptophobic Topcolor Z'

The high mass of the top quark presents a theoretical challenge to models of technicolor [31], [32] and composite Higgs [33], and in these models it is necessary to generate the top mass with a mechanism different from the Higgs. Top-color [34] models can generate a large top quark mass through the formation of a dynamical top-quark condensate: a bosonic state formed by a bound top-antitop pair that is generated by a new strong gauge force coupling preferentially to the third generation. Top-color proposes an additional broken symmetry, this time in the strong force sector where the $SU_{QCD}(3)$ gauge group is embedded into a larger structure $SU_2(3) \otimes SU_1(3)$ with couplings h_1 and h_2 ($h_1 \gg h_2$) that couple to the first two generations and to the third generation respectively. The symmetry breaking,

$$SU_2(3) \otimes SU_1(3) \rightarrow SU_{QCD}(3), \quad (1.17)$$

produces a massive color octet of bosons, often called top gluons, which couple mainly to bottom-quark pairs and top-quark pairs. Clearly, these models require another component to enhance the formation of the top-quark condensate, while blocking the formation of the bottom-quark condensate since we know that the b-quark is light. This tilting mechanism introduces a neutral gauge boson, Z' , with an attractive interaction between the top-quark pairs while exerting a repulsive interaction between the bottom-quark pairs. There are many ways to engineer the tilting with a new Z' , in fact in the literature there are four main models (Model I, II, III and IV) [35]. In this thesis we use as a benchmark model the Z' corresponding to Model IV, where the top-color tilting is constructed with a

leptophobic interaction. The width of this boson is given by

$$\Gamma(Z' \rightarrow t\bar{t}) = \frac{\alpha \cot^2(\theta_H) M_{Z'}}{8 \cos^2(\theta_W)} \left(\sqrt{1 - \frac{4m_t^2}{M_{Z'}^2}} \left(2 - 5 \frac{m_t^2}{M_{Z'}^2} \right) + 4 \right), \quad (1.18)$$

where $\theta_{H,W}$ are mixing angles, α is the strong coupling constant and $m_t, M_{Z'}$ are the masses of the top-quark and Z' boson. It should be noted that, in this model, the cross section increases as the width does and that the minimum possible width is of less interest. Hence, in this thesis we will focus on Z' of different relative width sizes, $\Gamma/M_{Z'}$; 1%, 10% and 30% and will be labeled respectively as narrow, wide and extra-wide. In different models, the dominant production of such resonances does not appear at the tree level, but rather it occurs at the one-loop level in association with an extra jet [36]. Without the additional jet, the resonance can still be produced off-shell, which gives a sizable contribution at low masses. This work also studies the production of a Z' boson with 1% relative width in association with an additional jet, referred as Z' +jet from now on.

2. THE ANATOMY OF PROTON-PROTON COLLISIONS

Physicists have exploited the well known relationship between energy and mass to probe the existence of speculated particles. This principle has been employed on several experimental variations based on the sought after goal.

The aim of this chapter is to give a motivation of the employment of hadron colliders to produce new particles, followed by a detailed description of the anatomy of proton-proton collisions.

2.1 Motivation To Employ Hadron Colliders

The vast majority of experiments in particle physics use beams of particles that can be controlled by the experimenter. Initially, these experiments had the beam directed onto a target that was stationary in the laboratory, called fixed-target. A physical quantity that measures the amount of energy available to create new particles is the center-of-mass energy of the system, \sqrt{s} , with

$$s = (p_t + p_b)^2, \quad (2.1)$$

where p_t is the four-momentum of the target and p_b of the beam. When searching for new particles a large center-of-mass energy is required, and this reveals a big disadvantage of fixed-target experiments since in this case

$$\sqrt{s} = (m_b^2 + m_t^2 + 2m_tE_b)^{1/2}, \quad (2.2)$$

and thus the center-of-mass energy only increases proportionally to $\sqrt{E_b}$. To overcome this limitation, two beams of particles traveling in opposite directions are made to collide at a small or zero crossing angle. If the particles in the beams have the same mass and laboratory energy E_L , then it can be easily shown in this case that

$$\sqrt{s} = 2E_L. \quad (2.3)$$

Thus, the center-of-mass energy increases linearly with the energy of the accelerated particles, making this option a better way to achieve higher center-of-mass energies compared to fixed-target experiments.

The particles in the beams reach the required energies for collision via accelerators. These could be of two types: linear or cyclic. In a linear accelerator (linac), charged particles pass through a series of metal pipes that are connected to alternate terminals of a radio frequency (R.F) oscillator or cavities. By changing the direction of the alternator, the particles passing through the pipe will be accelerated on their way between the exit of one pipe and the entry of the next. Proton linacs of this type are typically used in bigger experiments to inject beams with a moderate energy into a more powerful machine, usually a synchrotron, which is a cyclic accelerator. The principle behind cyclic accelerators is analogous to that of a linac except that the acceleration takes place in a near circular orbit rather than a straight line. In order to bend the trajectory of the charged particles –so that they follow the circular path– a set of bending magnets are used. The beam of particles reaches the desired energy by passing several times through the same R.F cavities.

In a cyclic accelerator there are two caveats that one has to consider. The first is that since colliding particles will be circulating over and over, they must be stable. This limits the interactions that can be studied. The second is that since the particles travel in a circular orbit, they continuously emit radiation, called synchrotron radiation. Furthermore, the amount of energy emitted by this process for a relativistic particle goes as $1/m^4$; hence,

for an electron beam the losses are severe and the need to compensate for these losses by large amounts of R.F power limits the energies for electron synchrotrons. Since the late 70's, when physicists were hunting the electroweak bosons, the community leaned towards using hadron colliders over lepton colliders despite the fact that the collision would be somewhat more messy. This brings us now into describing the physics involved in the anatomy of proton-proton collisions.

2.2 Proton-Proton Collisions

The framework employed to study the scattering processes at high energy hadron colliders is QCD because it describes the strong interactions between quarks and gluons. There are two types of scattering: hard and soft. The former type of scattering produces new particles and can be predicted with precision using perturbative QCD (pQCD), whereas the latter is dominated by non-pQCD effects and is not as well understood.

The anatomy of a proton-proton collision can be visualized in Fig. 2.1, where the two incoming protons have a hard scattering that produces a top-antitop quark pair, which then hadronizes. The hard scattering is also accompanied by secondary soft scattering, often referred to as pile-up (PU). In the next sections these processes will be discussed.

2.2.1 The Hard Scattering

Just like the 1909 scattering experiment that proved the existence of the atomic nucleus, the rich structure of the proton was also exposed using the same experimental approach. High-energy electrons were employed to measure the probability of scattering off the proton with large energy transfers and into large angles. It can be seen that depending on the energy of the electron, more or less of the proton structure can be resolved, Fig. 2.2. Deep Inelastic Scattering (DIS) played a key role in determining the partonic structure of the proton. In a DIS between an electron and a proton, $ep \rightarrow e + X$, the electron with four-momentum k emits a highly energetic off-shell photon with transfer momentum q

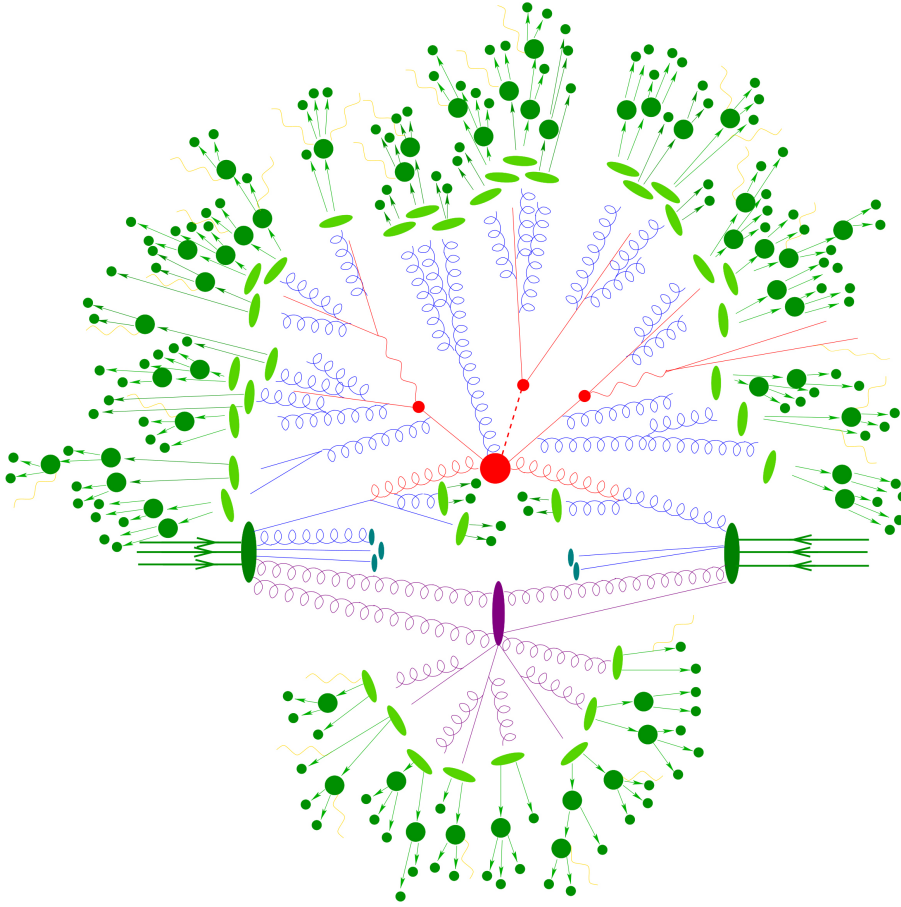


Figure 2.1: Schematic representation of a proton-proton (dark green ovals) collision. The partons interact in an elastic (purple) and inelastic (red) collision. The outgoing partons shower and hadronize (light green) [37].

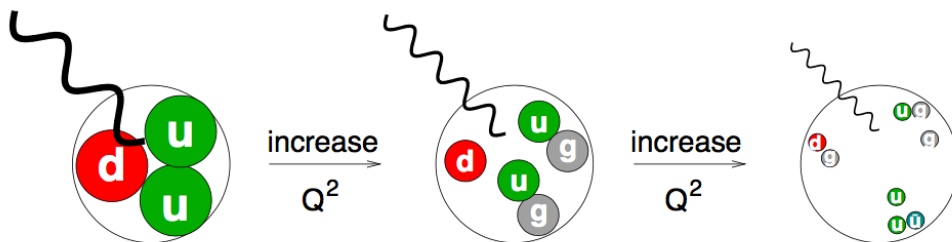


Figure 2.2: Depending on the energy of the probe, Q^2 , the rich structure of the proton can be resolved [38].

which then interacts with the proton carrying four-momentum p , as can be seen Fig 2.3. It can be shown that the differential cross section of the process is [38]

$$\frac{d^2\sigma}{dx dQ^2} = \frac{4\pi\alpha}{2xQ^4} (1 + (1 + y^2)F_2(x, Q^2) - y^2 F_1(x, Q^2)) , \quad (2.4)$$

where: α is the electromagnetic coupling constant, $Q^2 = -q^2$, $x = Q^2/(2p \cdot q)$,

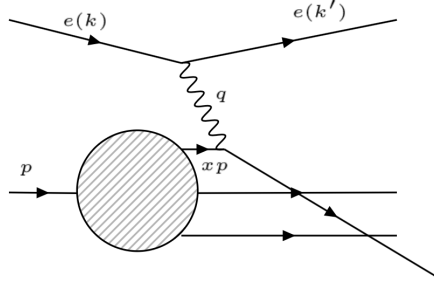


Figure 2.3: Diagram of the DIS between an electron and a proton.

$y = (q \cdot p)/(k \cdot p)$ are the standard kinematic variables of the quark-parton-model used for DIS calculations, and F_2, F_1 are the proton structure functions that encode the interaction between the photon and the proton. It should be noted that these functions are not calculable in pQCD. In contrast, a unique characteristic of QFT which allows the perturbative approach useful in QCD is the asymptotic freedom concept mentioned in Chapter 1. Asymptotic freedom is a necessary condition for the validity of the parton model because it allows hadrons to be considered made out of point-like constituents and it provides a very simple way of calculating scattering cross sections. To perform such calculations it is important to know how the hadron's momentum is distributed among its partons; the Parton Distribution Functions (PDFs) represent the probability densities to find a parton carrying a momentum fraction x at an energy scale Q^2 .

The dependence of these PDFs on Q^2 can be quantitatively predicted by the QCD evolution equations derived by Dokshitzer, Gribov, Lipatov, Altarelli and Parisi (DGLAP) in the 1970's, in the domain where perturbative approximations can be applied. The DGLAP

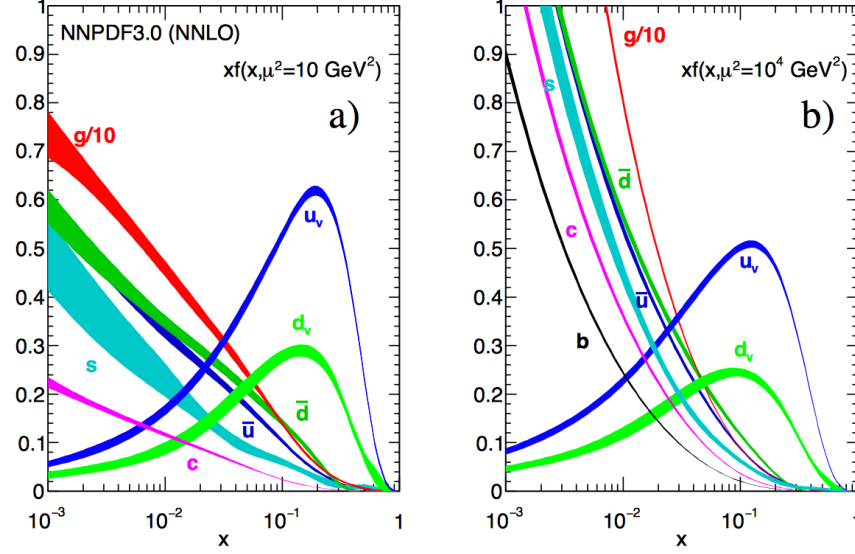


Figure 2.4: Parton Distribution Functions obtained in NNLO global analysis at a) $\mu^2 = 10 \text{ GeV}^2$ and b) $\mu^2 = 10^4 \text{ GeV}^2$ with $\alpha = 0.118$ [39].

equations have been formulated at different order of approximation relative to different powers of α , usually named as Leading-Order (LO), Next-to-Leading-Order (NLO) and Next-to-Next-Leading-Order (NNLO).

To zeroth order in α_s , the structure functions can be expressed directly in terms of the non-perturbative PDFs, $f_{a/A}$, of a quark of flavor a in a hadron of type A and the corresponding convoluted coefficient $C_{i,\alpha}$

$$F_i(x, Q^2) = \sum_{\alpha=q,g} C_{i,\alpha} f_{a/A}(x, Q^2) \quad . \quad (2.5)$$

In the Björken limit, $Q^2 \rightarrow \infty$, the PDFs become scale independent and the picture in which the photon interacts with point-like free quarks is valid and thus $F_i(x, Q^2) \rightarrow F_i(x)$. In this limit, Drell and Yan pointed out that the parton model ideas could be extended to certain processes in hadron-hadron collisions. The cross section of two hadrons A and B producing a particle X , as represented in Fig.2.5, can be expressed as

$$\sigma_{A+B \rightarrow X} = \int dx_a dx_b f_{a/A}(x_a) f_{b/B}(x_b) \hat{\sigma}_{a+b \rightarrow X} \quad , \quad (2.6)$$

where $\hat{\sigma}_{a+b \rightarrow X}$ is the partonic cross section and can be computed via pQCD.

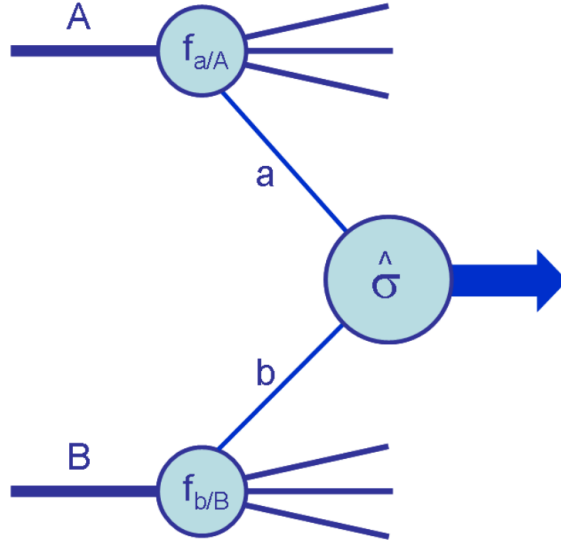


Figure 2.5: Diagram of the structure of a generic hard scattering process [40]. Partons a and b interact, represented by the partonic cross section ($\hat{\sigma}$), to produce a new particle. The partonic cross section can be computed via pQCD.

However, problems arise in these calculations when perturbative corrections from real and virtual gluon emissions are considered. In particular, the convergence of the perturbative expansion gets spoiled by large logarithms due to gluons emitted collinearly with the incoming quarks. It was later realized that such divergences could be absorbed via the DGLAP equations. The key point is that all of the logarithms that appear in the Drell-Yan corrections can be factored into renormalized PDFs. And, most importantly what the factorization theorem showed was that this is a general feature of hard scattering processes. Therefore, the cross section of the two hadrons A and B producing particle X is in fact

$$\sigma_{A+B \rightarrow X} = \int dx_a dx_b f_{a/A}(x_a, \mu_F^2) f_{b/B}(x_b, \mu_F^2) [\hat{\sigma}_0 + \alpha(\mu_R) \hat{\sigma}_1 + \alpha^2(\mu_R) \hat{\sigma}_2 + \dots]_{a+b \rightarrow X}, \quad (2.7)$$

where μ_F is the factorization scale that separates the long- and short-distance physics, and μ_R is the renormalization scale for the QCD running coupling. It is sensible to choose

μ_F and μ_R of the order of the typical momentum scales of the hard scattering process, $\mu_F = \mu_R = Q \approx M_X$.

2.2.2 Hadronization

Following the hard scattering, it is important to understand the propagation of the resulting partonic final states. The primary partons that emerged from the scattering develop into multi-parton cascades or showers by multiple gluon bremsstrahlung. These showers tend to develop along the directions of the primary partons to some distance ($\approx 10^{-15}$ m) where color confinement kicks in and the formation of hadrons out of these initial partons occurs. This process is called hadronization. These color-neutral hadrons produced in collimated sprays are referred as to jets.

This process is not perturbatively calculable and thus several models aim to describe the mechanisms of such hadron formation. The main current models are the cluster and string hadronization [41]. In the cluster model, gluons are split non-perturbatively after the parton shower to color-singlet quark pairs, combinations of these are then assumed to form clusters which then undergo simple isotropic decays to pairs of hadrons. The string model is based on the dynamics of a relativistic string that represents the color flux between the initial radiation quark pair. The string produces a linear confinement potential and then breaks ups into hadrons via quark pair production. A schematic representation of these models can be seen in Fig. 2.6. These models are used in the event generator simulations that will be described in Chapter 5.

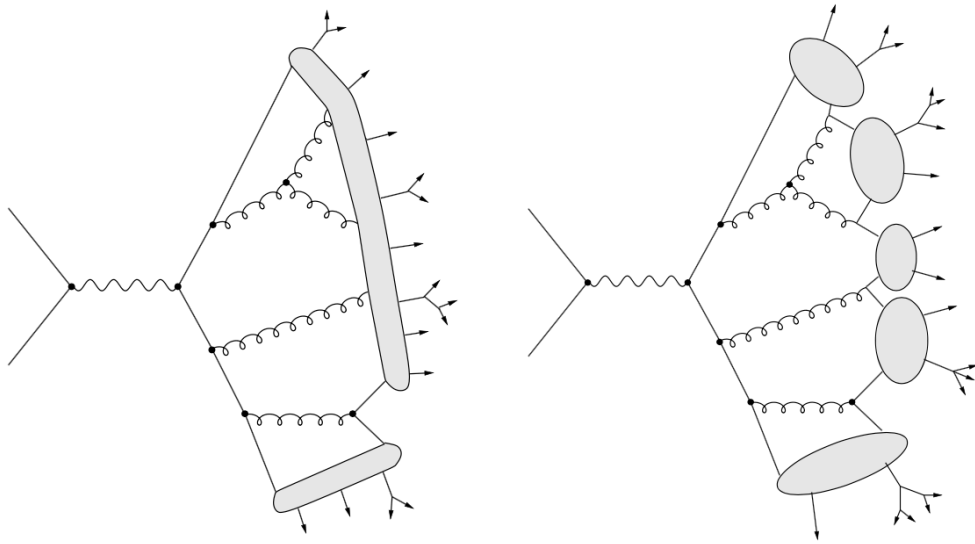


Figure 2.6: Schematic representations of phenomenological models of hadronization. The string model (left), which treats all but the highest-energy gluons as field lines. These are attracted to each other due to gluon self-interaction and form a string of strong color field. The cluster model (right) assumes that gluons are split non-perturbatively to form color-singlet quark pairs and combinations of these form clusters. [41]

3. EXPERIMENTAL SETUP

As mentioned in Chapter 2, particle accelerators are the tool physicists use to study processes that are rare and whose probabilities vary as function of the available energy. The Large Hadron Collider (LHC), located at CERN, has played a central role in Particle Physics. In this chapter we discuss what makes this powerful machine so special. Furthermore, we describe how the products of the proton-proton collisions are detected using the Compact Muon Solenoid (CMS) experiment.

3.1 LHC

The LHC has approximately 27 km in circumference to accelerate protons and ions in counter rotating beams at nearly the speed of light. The protons circulate around the ring in well-defined bunches as a consequence of the R.F scheme of the accelerator. In ideal conditions each of the two proton beams has about 2808 bunches, each containing 100 billion protons. The bunch spacing of 25 ns corresponds to each bunch crossing at an interaction point 40 million times per second. The number of events per second that are generated in the LHC is given by

$$N_{process} = L\sigma_{process}, \quad (3.1)$$

where $\sigma_{process}$ is the cross section of the process under study. The units used to measure the cross section are barns ($1 \text{ b} = 10^{-28} \text{ m}^2$). L represents the machine luminosity, which

depends solely on the beam parameters [42]:

$$L = \frac{N_b^2 n_b \nu_{rev} \gamma_r F}{4\pi \epsilon \beta} \quad (3.2)$$

- N_b represents the number of particles per bunch
- n_b is the number of bunches per beam
- ν_{rev} is the revolution frequency of the beams
- γ is the relativistic factor
- ϵ is the normalized transverse beam emittance
- β is the well-known beta function at the collision point and roughly describes the width of the beam squared divided by the emittance
- F is a geometric luminosity reduction due to the crossing angle at the interaction points.

The LHC has a design luminosity of $10^{34} \text{ cm}^{-2} \text{ s}^{-1}$. To increase the probability of the protons to interact, the LHC squeezes the maximum number of particles in the smallest amount of space around the interaction regions where the detectors are located. These challenging conditions are achieved by four key elements in the LHC:

Vacuum

Particles circulate in a vacuum tube where the pressure is approximately 10^{-13} atm because collisions with gas molecules should be avoided. Vacuum is also used for cryo-magnets and for helium distribution.

Magnets

About 9600 magnets: dipoles, quadrupoles, sextupoles, etc. are used in the LHC. Each magnet contributes to optimizing the particles trajectory and most importantly to constraining their motion to circular paths by bending the multi-TeV beams around the

ring. The dipoles are very special because the maximum energy that can be achieved in the LHC is directly proportional to their strength. These superconducting electromagnets are able to provide the very high magnetic field of 8.3 T over their full length of 15 m by allowing 11,850 A of current to flow through. In order to achieve the superconducting level, the extremely low temperature of 1.9 K is maintained at the LHC.

Cryogenics

Not only is the LHC one of the most empty places in the planet, but also the LHC is one of the coldest places too. In fact, it is the largest cryogenic system in the entire world. To reach the extremely low temperature of 1.9 K, super-fluid Helium is pumped in the system. About 120 T of helium are needed, with roughly 75% of it used in the magnets and the rest in pipes and refrigerator units.

Cavities

As mentioned in Chapter 2, the main role of the LHC r.f cavities is to keep the bunches of particles tightly squeezed to ensure maximum luminosity and to accelerate them. The bunch size is not constant around the ring, as a bunch circulates the ring, it gets squeezed and expanded. The bunches are a few centimeters long and a few millimeters wide as they circulate, but get ultimately squeezed to $16 \mu\text{m}^2$ at the interaction points.

3.1.1 Accelerating proton beams to 6.5 TeV

Protons in the LHC must go through a series of stages before they reach their final energy before the collision. Fig 3.1 shows the layout of the LHC complex. Both proton beams start in a bottle of hydrogen. The hydrogen is fed into an ion source, called Duo-plasmatron, where a cathode filament strips off their electrons. The resulting protons are then injected into a linear accelerator (LINAC2) that accelerates them to an energy of 50 MeV. After that, the beam of protons is fed into the Proton Synchrotron Booster (PBS)

that further accelerates them to an energy of 1.4 GeV, followed by the Proton Synchrotron (PS) where they reach an energy of 25 GeV and lastly to the Super Proton Synchrotron where they are accelerated to 450 GeV. When they reach this energy, the proton beam is split into the two beam pipes of the LHC with one of them circulating clockwise and the other counterclockwise. The LHC then accelerates both beams to their final energy of 6.5 TeV.

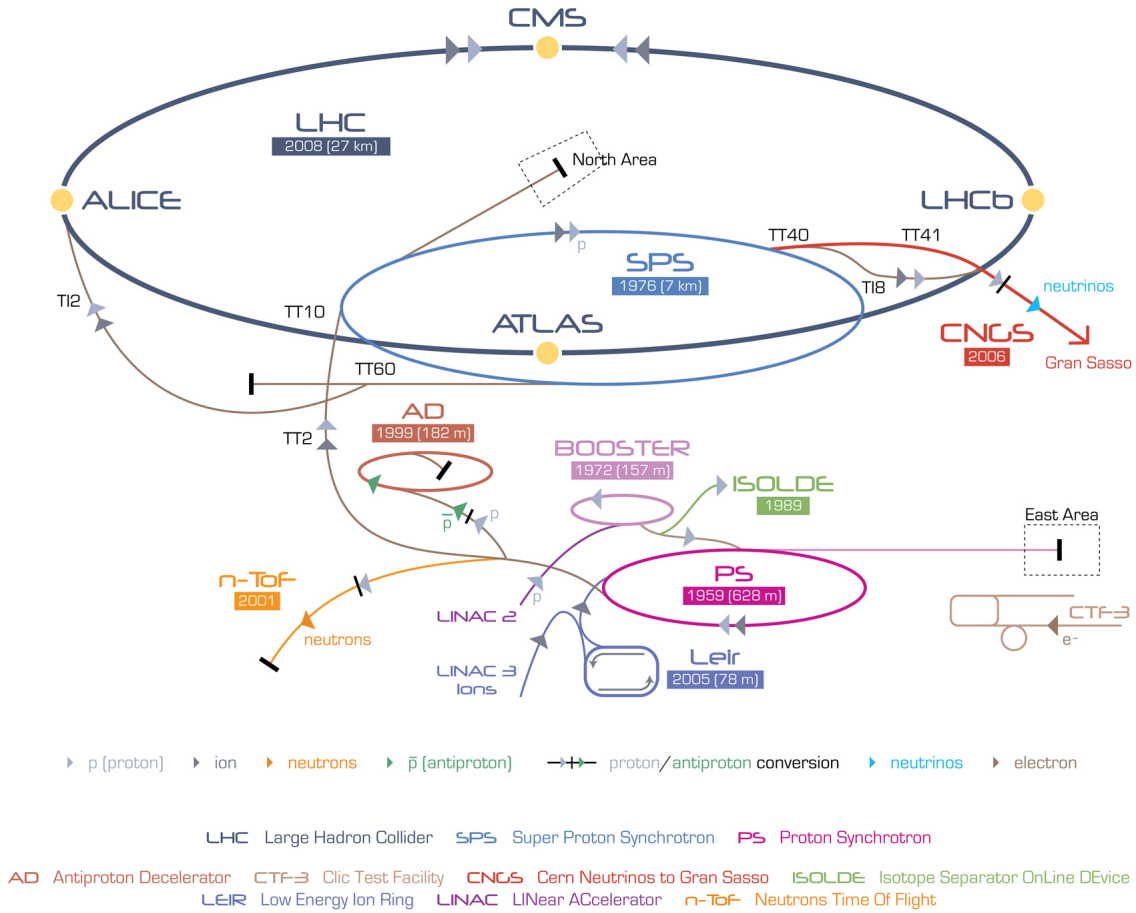


Figure 3.1: Schematic layout of the LHC accelerator chain. [43]

The total proton-proton cross section at $\sqrt{s} = 13$ TeV is roughly 100 mb. At design luminosity the general-purpose detectors observe an event rate of approximately 109 inelastic events/s.

3.2 The Compact Muon Solenoid (CMS) Detector

The CMS detector [44] is one of the two multi-purpose detector experiments at CERN, the other being ATLAS [45]. Having two independent experiments allows physicists to cross-check results, and enhances competition and collaboration. This detector was designed to study proton-proton collisions at $\sqrt{s} = 14 \text{ TeV}$ and instantaneous luminosities up to $10^{34} \text{ cm}^{-2}\text{s}^{-1}$.

The design of the CMS detector was based on achieving excellence in the following:

- Muon identification and momentum resolution that allows to unambiguously determine the charge of muons
- Charge-particle momentum resolution and reconstruction
- Electromagnetic energy resolution with high angular coverage
- Hadron calorimeter with large hermetic geometric coverage and fine segmentation

Fig 3.2 shows a schematic layout of the apparatus. The main features of it are: a high-field solenoid, a full-silicon-based tracking system, a homogenous electromagnetic calorimeter, a sampling hadron calorimeter, and a muon system. Before describing each component, the coordinate system of this detector needs to be explained.

Coordinate System

The cylindrical shape of the CMS detector is symmetrical around the beam line. It has an approximate radius of 7.5 m and a total length of 22 m. The experiment uses a Cartesian coordinate system whose origin is centered in the nominal collision point. The x -axis points towards the center of the LHC ring, the y -axis points upwards, and the z -axis points along the direction of the beam parallel to the cylinder axis. Due to the cylindrical symmetry of the apparatus, it is better to adopt a set of coordinates more suitable for physics measurements (ρ, ϕ, η) , where ρ is the radial distance from the beam

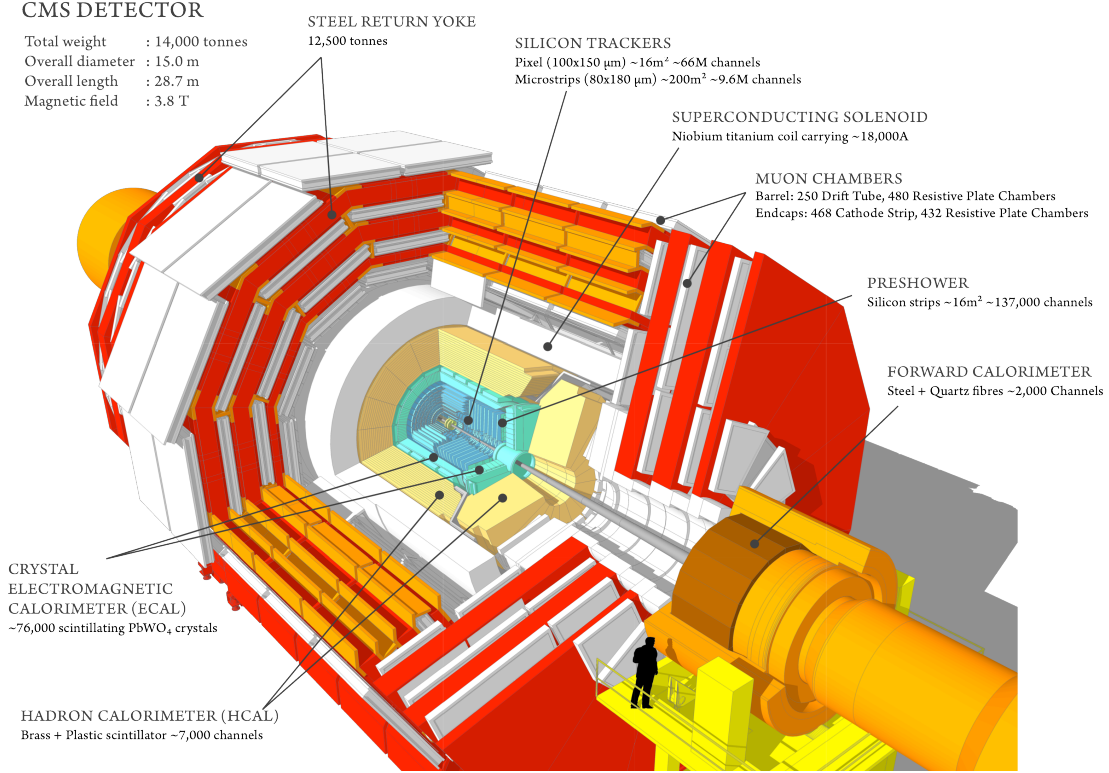


Figure 3.2: Schematic layout of the CMS detector.

axis, ϕ is the azimuthal angle with respect to the x -axis and η is the pseudo-rapidity given by $\eta = -\ln(\tan \frac{\theta}{2})$, where θ is the polar angle with respect to the z -axis. The reason why η is used as a coordinate is because it is a good approximation to a Lorentz boost invariant quantity along the beam axis used very frequently in Particle Physics called rapidity, $\zeta = \frac{1}{2} \ln \left(\frac{E+p_z}{E-p_z} \right)$, where E is the energy of the particle and p_z is the z -component of its momentum. The spacial separation between two particles in the detector, $\Delta R = \sqrt{\Delta\phi^2 + \Delta\eta^2}$, is another Lorentz boost invariant variable widely used. Finally, it is important to define the transverse components of energy and momentum given that the total energy is conserved in the transverse plane. These quantities are respectively given by $E_T = E \sin \theta$ and $p_T = \sqrt{p_x^2 + p_y^2}$.

The components of the CMS detector from the innermost to the outermost are described next.

3.2.1 Tracker

The inner tracking system provides a very precise, robust and efficient measurement of the trajectories of charged particles [46]. A schematic cross section of the CMS tracker is seen in Fig. 3.3. This sub-detector is made entirely of silicon and it consists of two parts; the pixel tracker at the very core, dealing with the highest intensity of particles; and silicon micro-strip detectors, surrounding the pixel tracker. This system covers a pseudo-rapidity range $|\eta| < 2.5$.

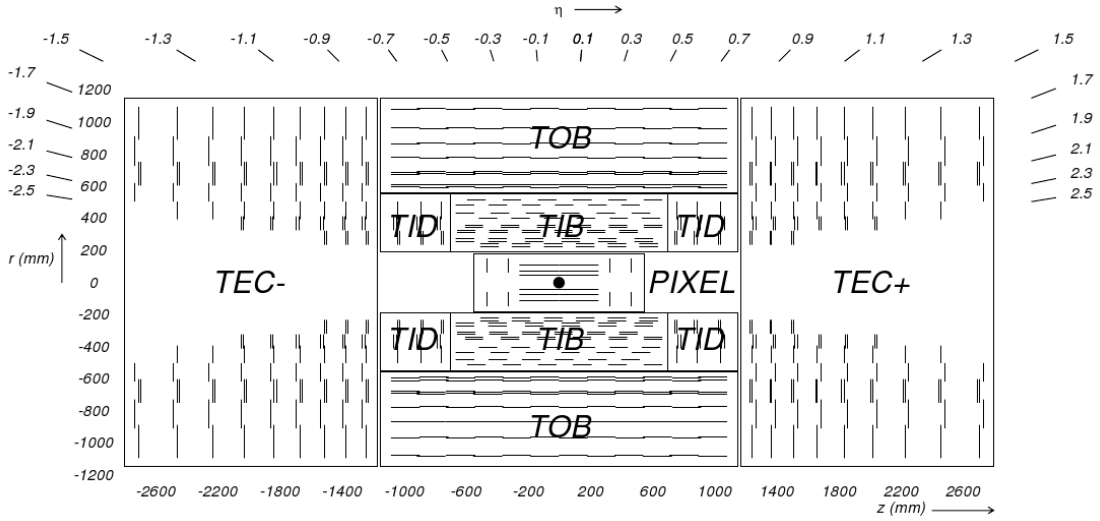


Figure 3.3: Schematic cross section of the CMS tracking system. [44]

Pixel Detector

The pixel system is the closest detector to the interaction point. It is responsible for precisely measuring tracks needed for vertex reconstruction. A radiation tolerant design was needed due to the vicinity to the interaction region, very high track rate and particle fluences. For this reason the sensor technology was chosen to be an $n+$ pixel on $n-$ substrate that allows partial depleted operation even at very high particle fluences.

This system is subdivided into two components: barrel (BPIX) and forward (FPix) regions. BPIX consists of 3 barrel layers located at a mean radii of 4.4 cm, 7.3 cm and

10.2 cm, all of them having a total length of 53 cm. This subcomponent contains about 768 detector modules. Each module consists of 8 to 16 read-out-chips with 52×80 pixels of size $100 \times 150 \mu\text{m}^2$ each, which are bump-bonded to the sensor. BPIX has 48 million pixels covering a total area of 0.78 cm^2 . FPIX, on the other hand, consists of 2 end-cap disks on each side at $|z| = 34.5 \text{ cm}$ and $|z| = 46.5 \text{ cm}$. The FPIX subcomponent is made out of 672 modules which corresponds to 18 million pixels in a total area of 0.28 cm^2 .

Silicon Strip Tracker

The sensor elements in the strip tracker are *p-on-n* type micro-strips. The system is subdivided into three components: the tracker outer barrel (TOB), the tracker end-caps (TEC) and the tracker inner barrel and disks (TIB/TID). The TIB subsystem consists of four concentric cylinders placed at radii of 25.5 cm, 33.9 cm, 41.85 cm, and 49.8 cm respectively from the beam axis and they extend to $|z| = 70.0 \text{ cm}$. The two innermost layers consist of double-sided modules with a strip pitch of $80 \mu\text{m}$, while the outer two layers consist single-sided modules with a strip pitch of $120 \mu\text{m}$. The TIDs are three disks placed between $z = 80 \text{ cm}$ and $z = 90 \text{ cm}$. All disks consist of three rings which span the radius from roughly 20 cm to 50 cm. The TOB is a single mechanical wheel that supports 688 self-contained sub-assemblies, called rods. Four identical disks joined by three outer and three inner cylinders compose the wheel. Finally, the TECs are made out of 9 disks that extend radially from 22 cm to 113.5 cm and from 124 cm to 280 cm along the z -axis. The 3 innermost rings have a thickness of $320 \mu\text{m}$, while the 6 outer ones have a thickness of $500 \mu\text{m}$.

3.2.2 Electromagnetic Calorimeter (ECAL)

The ECAL [47] is a hermetic and homogeneous calorimeter. The key assets of this system are its fine granularity, high energy resolution, and radiation resistance. It measures the energies of the emerging particles by using lead tungstate crystals that scintillate

when electrons and photons pass through it, this means that it produces light in proportion to the particle's energy. These crystals were chosen because they emit light in fast, short, and well-defined photon spurts that allow for a precise, fast and compact detector. The crystal cross section is approximately 0.0174×0.0174 in the $\eta - \phi$ coordinates and has a length of 23.0 cm that corresponds to 25.8 X_0 (radiation lengths).

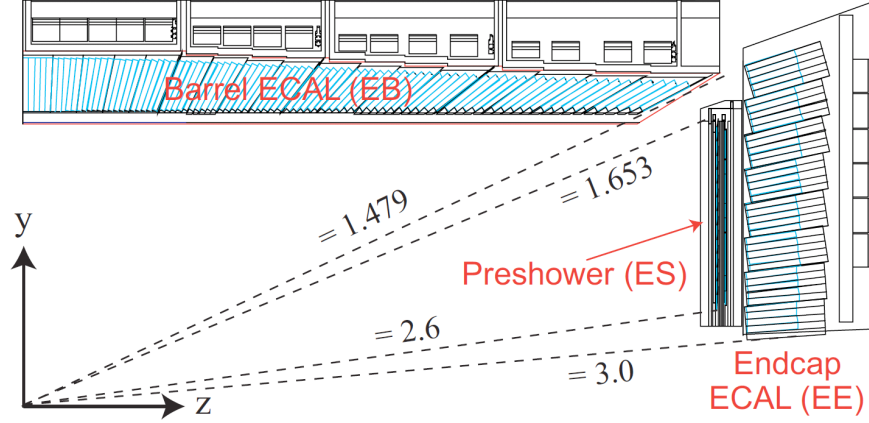


Figure 3.4: Schematic cross section of the electromagnetic calorimeter. [44]

This system consists of three parts: barrel (EB), pre-shower (ES) and end-caps (EE), as shown schematically in Fig 3.4. The EB consists of 61,200 of these crystals and is mounted in the central barrel part, covering the pseudo-rapidity range $|\eta| < 1.479$. The barrel granularity is 360-fold in ϕ and (2×85) -fold in η . The ES is placed in front of the EE and its main aim is to identify neutral pions and electrons against minimum ionizing particles. This pre-shower detector is a sampling calorimeter of lead radiators that initiate the electromagnetic showers and strip silicon sensors to measure the deposited energy and the transverse shower profile; its total thickness is 20 cm. The EE components are located at $|z| = 315$ cm and cover a rapidity range of $1.479 < |\eta| < 3.0$ and contain 7,324 components on each side.

The ECAL energy resolution is given by:

$$\left(\frac{\sigma}{E}\right)_{ECAL}^2 = \frac{2.8\%}{\sqrt{E(\text{GeV})}} + \left(\frac{12\%}{E(\text{GeV})}\right)^2 + (0.30\%)^2. \quad (3.3)$$

The first term of this formula is the stochastic term that reflects the event-to-event fluctuations in the lateral shower containment, the photo-statistics and the fluctuations in the energy deposited in the pre-shower regions. The second term reflects the non-uniformity of the longitudinal light collection, some internal calibration errors and the leakage of energy from the crystals. The last term reflects the sources of noise such as, electronics, digitalization, and pileup.

3.2.3 Hadron Calorimeter (HCAL)

The HCAL [48] detector is used to measure the energy of hadrons and indirectly provides measurement of the presence of non-interacting particles such as neutrinos. This system, just like the ECAL, is a hermetic detector that makes sure to capture the full extent of the emerging particles. The HCAL is a sampling calorimeter that finds particles' positions and energies using alternating layers of absorbing material followed by tiles of plastic scintillator. The hadronic energy resolution of the barrel ECAL + HCAL combination is given by

$$\left(\frac{\sigma}{E}\right)_{HCAL+ECAL} = \frac{a}{\sqrt{E(\text{GeV})}} \oplus b, \quad (3.4)$$

where a corresponds to a stochastic term and b to a constant. The values of these constants depend on the region, for the barrel $a = 0.847$ and $b = 0.074$, while in the endcaps $a = 1.98$ and $b = 0.09$.

Fig 3.5 shows that the HCAL consists of four sub-detectors: the barrel (HB), the endcap (HE), the outer (HO) and the forward (HF) hadron calorimeters.

HB

The HB sub-detector covers the pseudorapidity range $|\eta| < 1.3$. It consists of 36 identical azimuthal wedges that are aligned parallel to the beam axis. The wedges are made of flat brass absorber plates, but for structural strength the innermost and outermost plates are made of stainless steel. In between absorber plates, the plastic scintillator is divided

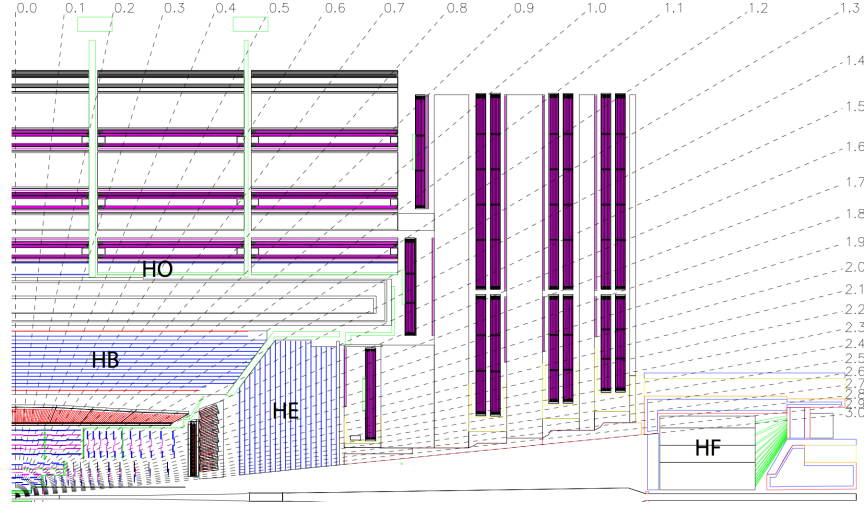


Figure 3.5: Schematic cross section of the hadron calorimeter. [44]

into 16 sectors, allowing a granularity of 0.087^2 in the $\eta - \phi$ coordinate system. The interaction lengths, λ_I , provided by this sub-detector are 5.82 at $|\eta| = 0$ all the way to 10.6 for $|\eta| = 1.3$.

HE

The HE sub-detector covers a substantial portion of the pseudorapidity range, $1.3 < |\eta| < 3$, containing about 34% of the particles produced in the final state. Due to the high fluence of particles in this region, it is capable of handling high counting rates while being radiation hard. Also, because the calorimeter is inserted into the ends of a 4-T solenoidal magnet, the absorber is made out of a non magnetic material, C26000 cartridge brass, that is able to fully contain the hadronic showers. The design of the absorber geometry is driven by the need to minimize the cracks between HB and HE and to provide self-supporting hermetic construction. The brass pates are 7.9 cm-thick with 0.9 cm gaps that accommodate the scintillators. This sub-detector provides about 10 interaction lengths and a granularity $\Delta\eta \times \Delta\phi = 0.087^2$ for $|\eta| < 1.6$ and 0.17^2 for $|\eta| \leq 1.6$.

HO

In the barrel region ($|\eta| < 1.3$), the combined power of the EB and HB does not provide sufficient containment for hadronic showers; the HO sub-detector's job is to ensure their full containment. This sub-detector is located outside the superconducting magnet and inside the Muon Barrel system. The sizes and positions of the HO components are positioned such that they roughly match with the layers of the HB to make towers of the same granularity. With this added layer, the total depth of the calorimeter system is thus extended to at least $11.8 \lambda_I$.

HF

The HF system, located in the region $3.0 < |\eta| < 5.0$, experiences extremely large particle fluxes – more than all other components together. Its design was guided by the necessity to survive severe conditions and for a long time. The active material in this system are quartz fibers that were especially chosen due to their radiation hardness. This calorimeter consists of a series of steel absorbers with grooves where the fibers are inserted. The geometry of it is essentially a cylindrical steel structure with an outer radius of 130 cm and 165 cm and it is located at $|z| = 112$ cm from the interaction point.

3.2.4 Superconducting Magnet and Yoke

The CMS magnet [49] is the largest superconducting magnet ever constructed and it is the central device around which the experiment is built. Its job is to bend the paths of charged particles to facilitate their momentum measurement. The CMS magnet is a solenoid – a magnet made of coils of wire that produce a uniform magnetic field when electricity flows through them. The solenoid is 6 m in diameter and 12.5 m in length and it provides a 3.8 Tesla magnetic field intensity that is 10^5 times stronger than the Earth's. Fig.3.6 shows the intensity of the field across the full detector. The tracker and both calorimeter detectors (ECAL and HCAL) fit inside of the magnet coil, which bends the

particles' path allowing a better resolution of their momenta. The magnetic flux is returned through a 10^4 t yoke, which is composed by 11 large elements, 6 end-cap disks and 5 barrel wheels. The yoke also serves as structural material to host the muon system.

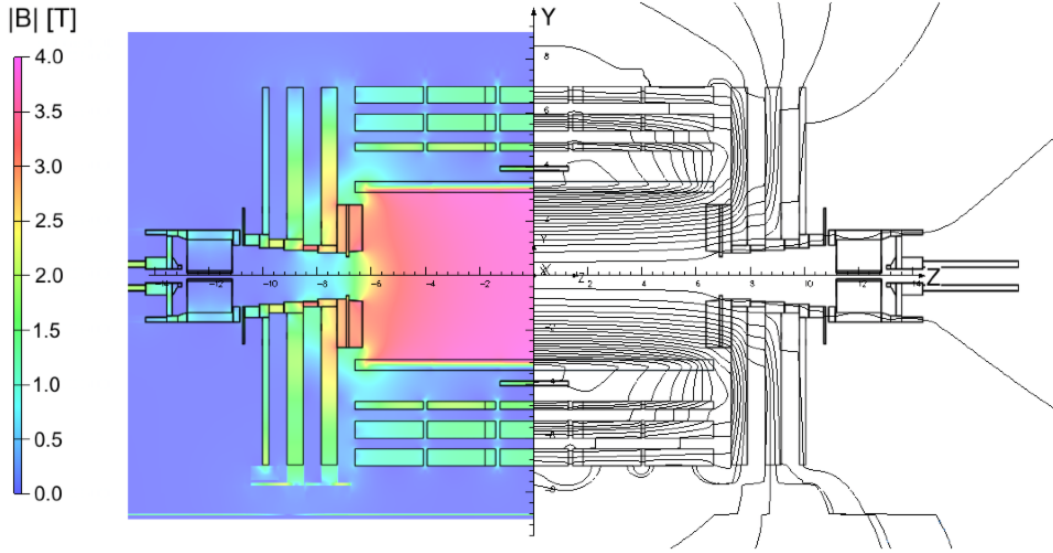


Figure 3.6: Schematic cross section of of the intensity of the magnetic field in the CMS detector. [44]

3.2.5 Muon System

This sub-detector [49] is a very powerful tool for recognizing signatures of rare physics processes. It is placed at the very edge of the experiment because muons, unlike most particles, are not stopped by the calorimeters. The muon system has 3 main functions: momentum measurement, muon identification and triggering. It is designed to be able to reconstruct the momentum and charge of muons over the full kinematic range of the LHC.

Just like the other sub-detectors it consists of a barrel and end-cap components. In the barrel region, where the muon rate is low, 250 drift tubes (DTs) are located among the layers of the return yoke and they cover the pseudorapidity region $|\eta| < 1.2$. While in the end-cap region, $0.9 < |\eta| < 2.4$, where the muon rates and background levels are high and the magnetic field is non-uniform, Cathode Strip Chambers (CSCs) are used due to

their fast response time, fine segmentation, and radiation hardness. In addition to the DTs and CSCs, Resistive Plate Chambers (RPCs) are also located in both sub-systems. They provide robust pattern recognition for rejection of non-muon backgrounds and efficient matching of hits even to the extent of the inner tracker. Fig 3.7 shows the layout of the different sub-systems.

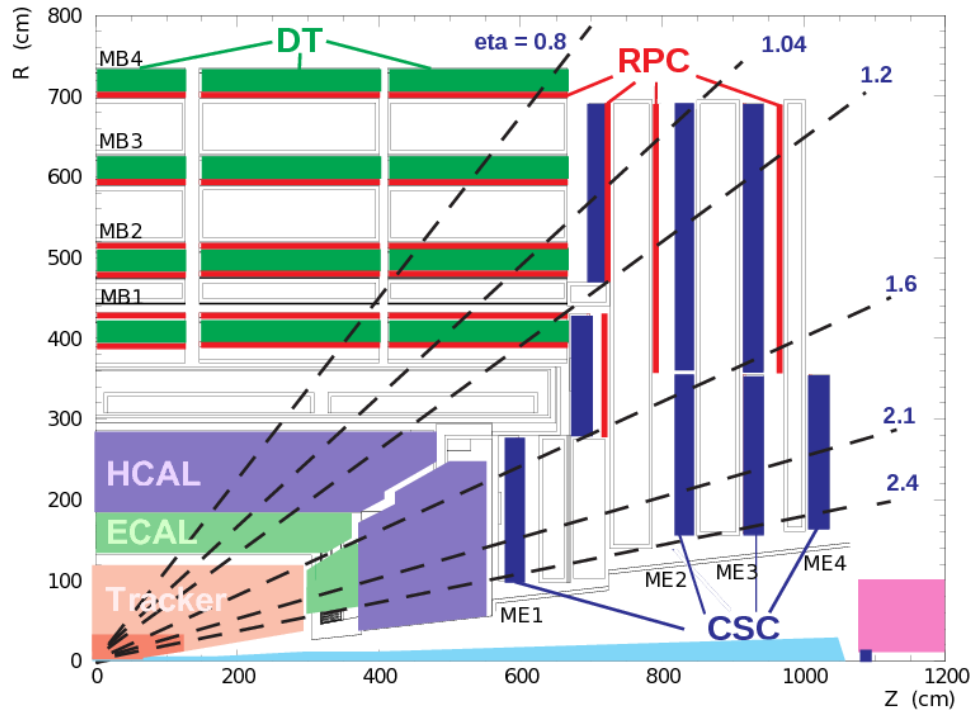


Figure 3.7: Layout of one quadrant of the CMS apparatus showing the Muon System and its sub-components. [44]

The relative momentum resolution, $\Delta p/p$, of the muon system combined with the tracking information is roughly 2% and 6% in the barrel and end-caps, respectively, for muons with $20 < p_T < 100$ GeV. Above this threshold and up to 1 TeV the resolution is better than 10% in the barrel region than in the end-cap.

3.2.6 Trigger System

Thus far the physical sub-components of the CMS apparatus have been described, but another key element of this experiment is its ability to combine the information of the sub-detectors and be able to only select potentially interesting events.

The trigger system [50] is responsible of filtering the energetic head-on interactions out from the low-energy collisions. The triggering happens on a two-level process, the Level-1 (L1) trigger and the High Level Trigger (HLT), which are described next.

L1 Trigger

The L1 trigger [51] is an extremely fast process that finds signs of events with large amounts of energy or unusual combinations of the raw information provided by the sub-detectors. It selects 10^5 events from the 10^9 available every second. The L1 system consists of two main parts that process the information from the calorimeters and muon system separately, Fig. 3.8. Each of these parts receive in input trigger primitives from different sub-detectors and their outputs are combined to produce different physics objects: muons, electrons, photons, jets, and energy sums. By using their momentum, position, isolation and quality, the micro Global Trigger [52] performs the final L1 trigger decision.

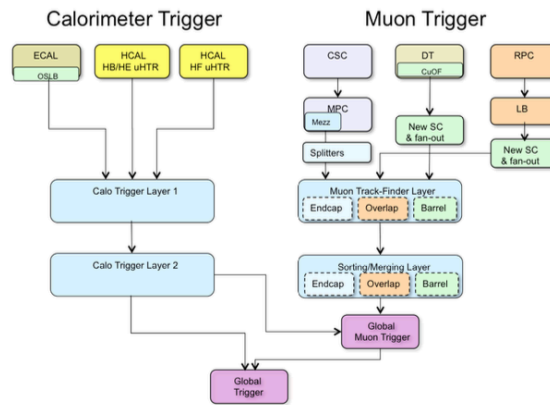


Figure 3.8: Schematic of the structure of the L1 trigger system.

HLT

The second level, the HLT [53], synchronizes the information from the different parts of the detector a quick recreation of the event through a farm of more than a thousand commercial processors.

Each HLT trigger path is a sequence of filtering, reconstructing, and selecting steps of increasing complexity. The HLT starts from the L1 candidate, then it filters events using the full granularity data from the sub-detectors, followed by the reconstruction of physics objects that are based on sophisticated offline-quality reconstruction algorithms, Fig. 3.9.

This system only selects 100 events per second out of the 10^5 provided by the L1 system. Events are then grouped into a set of non-exclusive streams according to the HLT decisions.

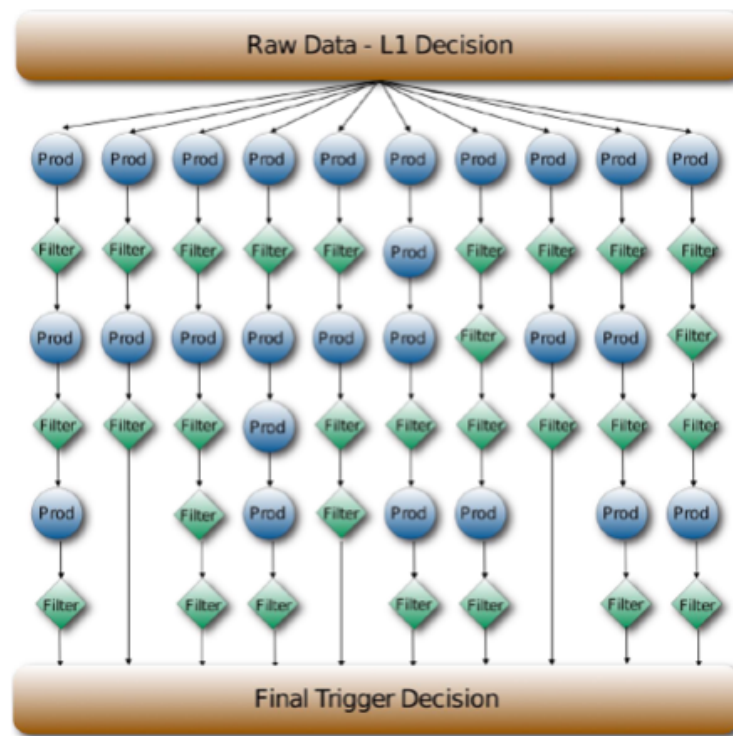


Figure 3.9: Representation of the HLT paths. Starting from the L1 information, a sequence of filter modules and producer modules that reconstruct physics objects select events of interest.

4. PARTICLE RECONSTRUCTION

Detecting the products of proton-proton collisions is the first step to find out whether or not top-antitop quark pair resonances exist. The next step is to use the information of all of the CMS detectors to reconstruct the underlying events.

In this chapter the algorithms used by CMS to reconstruct final-state particles are described. Then, the methodology used to identify physics objects of interest is discussed.

4.1 The Particle Flow Algorithm

The Particle Flow (PF) algorithm [54] deployed in the CMS experiment serves to identify and reconstruct each individual particle emerging from the proton-proton collisions by compiling all of the information that the sub-detectors provide.

For this algorithm to be successful, it is crucial that the CMS apparatus provides: excellent tracking efficiency and purity, the ability to resolve the calorimeter energy deposits of neighboring particles, as well as an unambiguous way to match charged-particle tracks to calorimeter deposits. The building blocks of the algorithm are tracks and clusters of energy. Fig.4.1 shows an overview of the PF algorithm, which is described below.

Tracking

The PF algorithm uses a Combinatorial Track Finder (CTF) software [55] filter to produce the collection of reconstructed tracks. This collection is produced by multiple iterations of the CTF sequence in a process called iterative tracking [56]. In a nutshell, the initial iterations search for tracks that are easy to find, after each iteration, hits associated

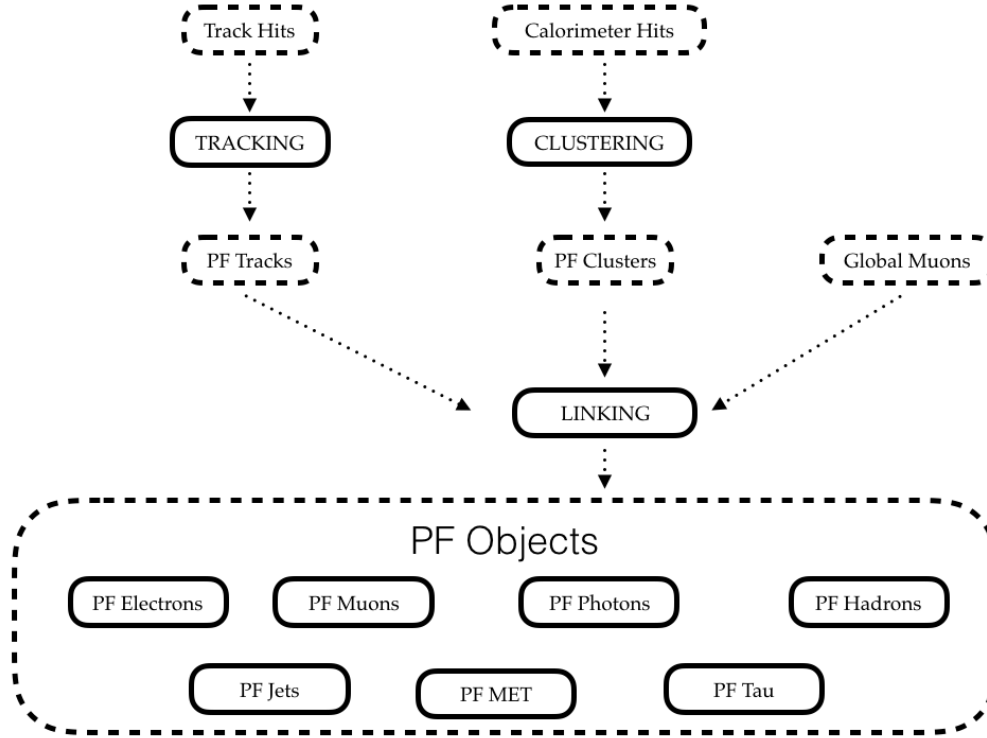


Figure 4.1: Diagram of the particle flow reconstruction

with reconstructed tracks are removed to simplify subsequent iterations. Each iteration consists of four steps: seed generation, track-finding, track-fitting and track selection. These steps are described next.

The seed generation provides initial track candidates using only 2 or 3 hits in the tracker. To generate the seeds two elements are needed: seeding layers and tracking regions. The seeding layers are pairs or triplets of tracker layers in which hits are found. The tracking regions specify track parameters like its p_T and its maximum transverse and longitudinal distances of the closest approach to the beam spot. Next, the track finding module of the CTF algorithm uses the trajectory seeds and then builds track candidates by adding hits from successive tracker layers. After a collection of tracks has been produced, the track-fitting module of the CTF algorithm provides the best trajectory of the track using the Kalman filter and smoother algorithm [57]. Finally, the track selection module sets quality flags and only selects tracks that meet certain specified criteria. This algorithm

is so efficient that even particles with p_T as low as 150 MeV, and created as far as 50 cm from the interaction point are reconstructed with as little as 1% fake contamination. The resulting tracks correspond to the PF track collection.

Clustering

The clustering algorithm is designed to perform the following: detect and measure the energy and direction of stable neutral particles; separate these neutral particles from energy deposits from charged hadrons; reconstruct and identify electrons and all accompanying radiated photons; and help with the energy measurement of charged hadrons of high p_T or low-quality tracks.

This algorithm recognizes individual deposits of energy from charged and neutral particles by exploiting the high granularity of the calorimeters. It can distinguish energy depositions that are close together. The clustering is performed separately in each of the calorimeters giving rise to a collection of clusters. The clustering procedure can be summarized as follows:

- Find all hits in the calorimeter that exceed a certain energy threshold, the one with the greatest energy deposit becomes the seed.
- Grow the cluster by grouping the seed with the remaining neighboring hits
- Determine the final energy and position of the cluster with an iterative procedure [58]

The resulting clusters correspond to the PF Cluster collection.

Before the linking step we need to define a global muon. It is defined when hits in the muon system are matched to those reconstructed in the inner tracking system using the Kalman filter technique.

Linking

Once all of the PF tracks and clusters and global muons have been identified, the link algorithm is responsible of reconstructing the final state objects. This algorithm must reconstruct each single particle, while getting rid of any possible double counting from different sub-detectors.

This link algorithm is performed for each pair of elements (PF Cluster, PF track, or global muon) in the event and for each of them a distance is defined and used to quantify the quality of the link. This produces blocks of elements that could be linked directly or indirectly. Due to the high granularity of the CMS sub-detectors, blocks typically contain at most three elements, and constitute simple inputs for the particle identification process.

A link between a PF track and a PF cluster occurs as follows. First, the track is extrapolated from the last measured hit in the tracker to the PS and then to the ECAL and then to the HCAL. If the extrapolated position is within the selected PF cluster boundaries, the link is done. Similarly, a link between ECAL and HCAL clusters is established when the cluster position in the more granular calorimeter is within the cluster envelope in the less granular calorimeter. Finally, a link between a track in the muon system and a track in the tracker is established when the global fit between the two returns an acceptable χ^2 (goodness of fit) [44]. If more than one fit between multiple tracks is available, the one with the smallest χ^2 is selected.

4.2 Particle Identification

Starting with a block of the PF collections produced by the linking algorithm, the last step is to produce the physics objects of interest: muons, electrons, photons, hadrons and missing transverse energy. This is done as following:

- Identify and remove muons: First, each global muon can become a PF muon when its combined momentum is compatible (within three standard deviations) with that

determined from the sole tracker information. The corresponding track is then removed from the block.

- Identify and remove electrons: Each track is pre-identified by exploiting the tracker as a pre-shower because electrons tend to produce short tracks and lose energy by Bremsstrahlung on their way to the calorimeters. These pre-identified tracks are then refit with a Gaussian-Sum Filter [59] to follow their trajectories to the ECAL. The final identification is performed by combining tracking and calorimeter variables. Each identified electron gives rise to a PF electron. Then the corresponding tracks and ECAL clusters are removed from further processing.
- Identify and remove hadrons: Each of the remaining tracks can give rise to a PF hadron, if the calorimeter energy linked to those tracks is compatible the hadron is identified and the associated tracks and clusters are removed.
- Identify and remove converted and prompt photons: The remaining ECAL clusters not linked to any track are associated to photons.
- Identify and remove neutral hadrons. The remaining HCAL clusters not linked to any track are associated to photons.

Fig 4.2 shows a Nassi-Schneiderman diagram that shows the identification process.

4.3 Jets and Missing Transverse Energy Reconstruction

After getting the list of identified hadrons emerging from the proton-proton collision, the next step is to define a jet. Jets are defined by the algorithm that creates them. There are two main jet algorithms: cluster-based and cone-based. The former algorithm starts from all of the hadrons and leptons available and then perform an iterative pair-wise clustering to build larger objects using either geometric or kinematic properties. While cone algorithms seek to find geometric regions which maximize the momentum in a given area or shape. The jet algorithm used in this work is a clustering one and it is described below:

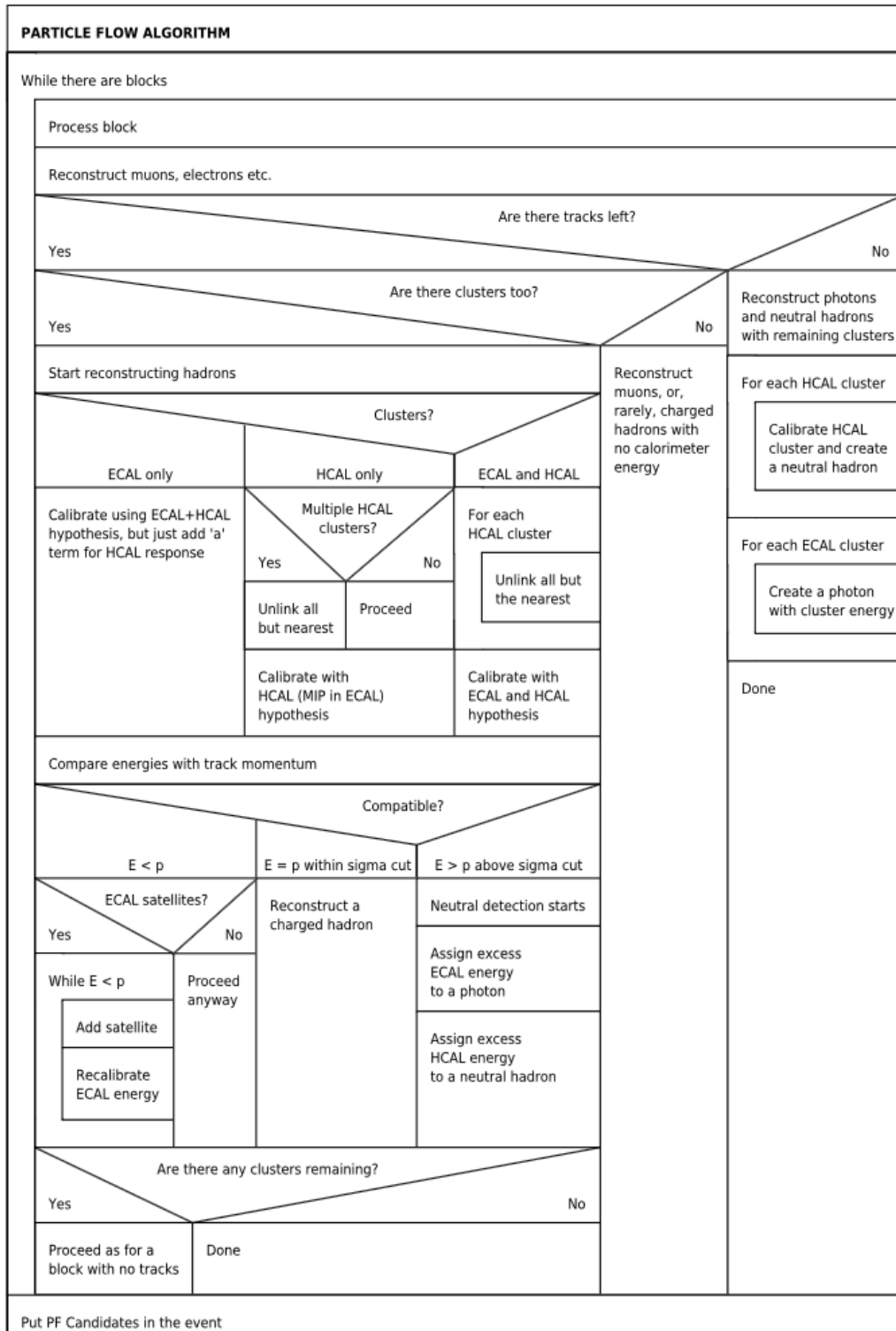


Figure 4.2: Nassi-Schneiderman diagram of the structured particle flow identification process

- First, define a distance $d_{i,j}$ between two objects i, j :

$$d_{i,j} = \min(d_{i,B}^p, d_{j,B}^p) \Delta R_{i,j}^2 / R^2 \quad (4.1)$$

where $d_{i,B}$ is the distance between object i and the beam direction B , p is an integer number, R is the chosen cone radius and ΔR is the geometric separation defined in Chapter 3.2.

- Then, find the smallest between $d_{i,j}$ and $d_{i,B}$
- If $d_{i,j}$ is the smallest then recombine i, j , else if $d_{i,B}$ is the smallest then i is the jet axis.

If $p = -1$, the algorithm receives the name of Anti- k_T (AK) [60], whereas $p = 1$ refers to the k_T algorithm. It should be pointed out that it is called k_T because in most literature $d_{iB} = k_{T_i}^2$ refers to the squared transverse component of particle i 's momentum. The AK algorithm successively merges objects with relative high p_T and soft hadrons will be merged around the harder ones. If two hard jets are close by, the energy will then be shared based on the specified cone radius. One of the best qualities of this method is that the shape of the jet gets unaffected by soft radiation, which is a key factor for the subtraction of the underlying event. All of these properties can be more clearly seen in Fig 4.3 , where a comparison of the jet definitions AK and k_T is shown. In this work we use jets defined by the AK algorithm.

Finally, due to the large pseudorapidity coverage of the CMS detector, precise tests of 2D momentum conservation in the plane perpendicular to the direction of beams can be performed. Therefore, any measured significant imbalance in transverse momentum can be considered as signature of weakly interacting particles which typically leave the detector without a trace. This quantity is determined from the vector sum over energy

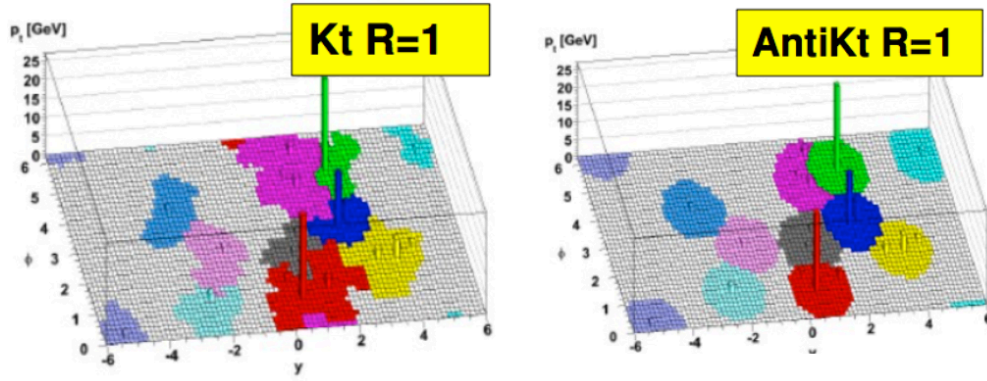


Figure 4.3: Comparison between the Anti- k_T and k_T algorithms that define a jet [60] .

deposits in calorimeter towers

$$\vec{E}_T = - \sum_n (E_n \sin \theta_n \cos \phi_n \hat{x} + E_n \sin \theta_n \sin \phi_n \hat{y}) \quad (4.2)$$

This quantity is often referred to as MET. Similarly, the missing transverse momentum, $p_T^{miss} = \left| \vec{p}_T^{miss} \right|$, is equivalent to the missing transverse energy when the missing particles are massless.

5. EVENT CHARACTERIZATION AND SIMULATION

Searching for top-antitop quark pair resonances (signal) requires to know beforehand which SM processes (background) would generate the same final state objects than such resonances would. Thus, the production rate of the background and signal events and their expected topologies are described in this chapter. Furthermore, the simulation of both events is also discussed.

5.1 Event Topology

The searches for a heavy resonance that decays into a top-antitop quark pair ($X \rightarrow t\bar{t} \rightarrow W^+bW^-\bar{b}$) can be performed in different ways depending on the final states of the decay products and their kinematic topology.

Since the top-quark decays most of the time into a W boson and a b quark, its decay channels are dictated by the way the W boson decays, either hadronically ($W \rightarrow q\bar{q}$) or leptonically ($W \rightarrow \ell\nu_\ell$). Hence, for the top-antitop quark pair there are three channels of decay modes: the "hadronic" or "all-jets" channel is where both W bosons decay hadronically, the "dileptonic" channel is where both W bosons decay leptonically, and the "semileptonic" or "lepton+jets" channel is where one W decays hadronically and the other leptonically. The latter is the channel chosen to perform this analysis due to its balance between branching fraction and its signal-to-noise ratio. Furthermore, in this work only the case where the lepton is a muon is considered (muon+jets channel). This channel covers approximately 15% of the top-antitop quark pair production, as seen in Fig. 5.1.

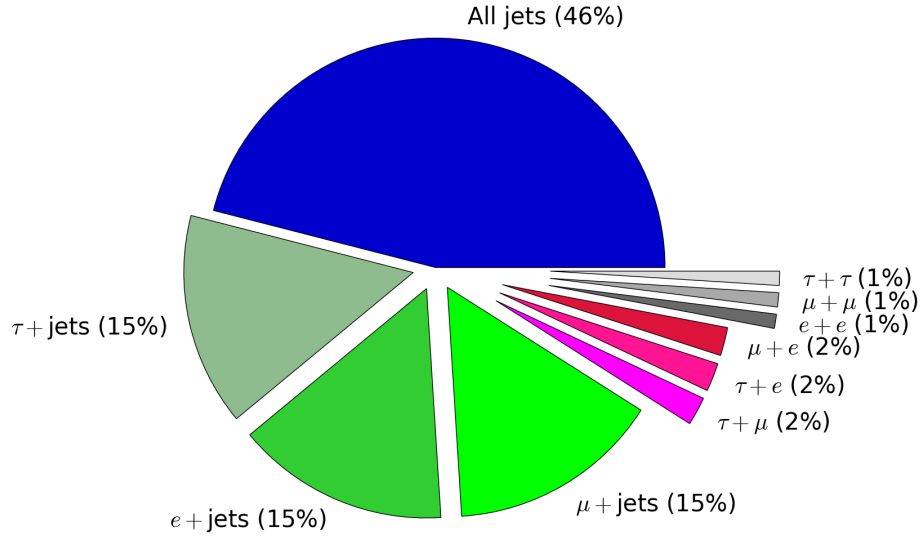


Figure 5.1: Pie chart that shows the different branching fractions of the top-antitop quark pair. This analysis covers the μ +jets channel (light green), corresponding to about 15% of the branching fraction.

Boosted Topology

Not only do the decay products characterize the strategy of the analysis but also their kinematics define it. At the threshold energy for top-antitop quark pair production, the top-quarks' decay products appear well separated in the detector. This is often called a "resolved topology". On the other hand, for a heavy resonance with mass well above the previous threshold, the top-antitop quark pair will be produced with a large Lorentz boost, $\gamma = E/m$, resulting in a high level of collimation of the decay products, with an approximate separation $\Delta R \approx 2/\gamma$. This is often called a "boosted topology". This work is optimized to search for top-antitop quark resonances in these boosted conditions. Fig. 5.2 shows schematically the differences between these two topologies. In this boosted topology we expect to have exactly one muon, missing transverse energy and at least two jets as final state objects.

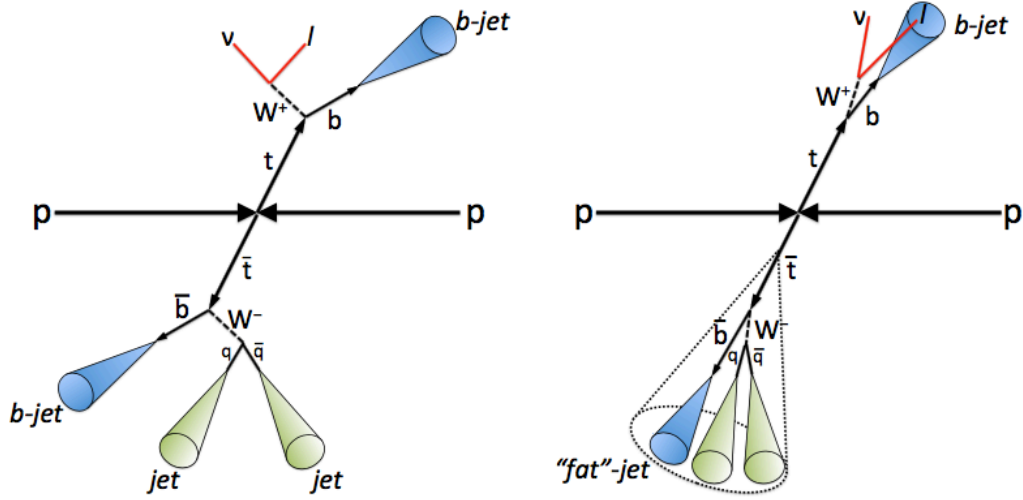


Figure 5.2: Resolved (left) and boosted (right) topologies of the top-antitop quark decay products. This analysis considers events where jets could be collimated forming "fat" jets and leptons that could be merged within a neighboring jet.

5.2 SM backgrounds

As mentioned in Chapter 2, the expected cross sections of the SM processes at $\sqrt{s} = 13 \text{ TeV}$ can be computed to different orders of precision. For example, Fig. 5.3 shows the NLO cross sections for different processes within the SM as a function of \sqrt{s} . This information is necessary in order to estimate the amount of background events.

When searching for new particles it is crucial to understand all of possible sources of background events. The processes that can mimic the signature of a heavy top-antitop quark resonance that decays semileptonically are the following:

- SM $t\bar{t}$ Production

It is the most important irreducible background process. It is dominantly produced by gluon fusion and in a less extent by quark annihilation.

- W +jets Production

This is the second most important irreducible background. These events arise when a W boson is produced in association with quarks or gluons. The W boson then decays leptonically and the quarks then hadronize.

lepton along with secondary hadronic activity (Z +jets) at the interaction point can fake a signal event.

- QCD Multi-jet (QCD) Production

These background events arise from parton processes like: $qq \rightarrow qq$, $q\bar{q} \rightarrow q\bar{q}$, $gg \rightarrow gg$, etc. They could fake a signal event by producing enough hadronic activity and when b or c quarks decay and produce a charged lepton and a neutrino.

5.3 Simulated Samples

In order to fully predict the observed events by the CMS apparatus it is necessary to have a full simulation of them: starting from their generation at the hard interaction, followed by the hadronization process, and finishing with the interactions of the final states particles with the detector components.

The simulated events can be generated using Monte Carlo techniques, this is why we generally refer to the simulated samples as Monte Carlo (MC) samples. There are event generator softwares that can generate the hard scattering, or parton showers, or the hadronization process, or all.

- POWHEG [62], [63] implements NLO calculations of hard events and can also perform the subsequent parton shower model.
- MADGRAPH [64] implements LO calculations and serves as input into the full generation chain. It is particularly useful to compute matrix elements associated with new processes.
- PYTHIA 8 [65] is a self-contained and standalone package that can generate end-to-end high energy physics processes. It contains a library of hard interactions, models for the initial- and final-state parton showers that takes into account beam remnants, as well as string fragmentation and particle decays.

The final-state particles produced by these event generators are then fed into the CMS software (CMSSW) environment [66] where they first go through a detailed GEANT4-

based simulation [67] of the CMS detector, followed by the modeling of the detector electronics' response, called digitalization.

The background MC samples used in this work are summarized in Table 5.1 . They were all generated at the center-of-mass energy of 13 TeV using the NNPDF 3.0 PDF parametrizations [68]. Moreover, they include the simulation of additional inelastic proton-proton interactions within the same bunch crossing ("in-time" PU) and the additional contribution in the signal readout from the previous and next bunch crossing ("out-of-time" PU) which are assumed to be 25 ns apart from the main bunch crossing. Also, it can be noticed that some of these MC samples are binned in p_T , where p_T is the summed momentum of all the final state partons in the matrix element.

Similarly for the benchmark BSM MC signal samples, Table 5.2 summarizes their information. MADGRAPHv5 is used to generate generic high-mass resonances: a model with a Z' boson with same left- and right-handed coupling to fermions, and masses between 0.5 TeV and 5 TeV. The Z' boson decays into $t\bar{t}$ in all generated events. The width of the resonances is set to 1%, 10% and 30% of the Z' boson mass, as mentioned in 1.4.3. The parton showering is modeled with PYTHIA. For the Z' models considered, we use the NLO cross sections.

PYTHIA 8 is used to generate a KK excitation of a gluon. These samples are also generated with resonance masses between 0.5 TeV and 5 TeV. The branching fraction of the resonance state into top quark pairs is about 94%, but they depend on the specific KK coupling parameters. For the studied model, the respective PYTHIA parameters are set to the default values , except the coupling of the KK gluon to the right-handed top quarks which has been set to 5 [70]. The LO cross sections for the KK gluons are obtained from PYTHIA 8; these values are multiplied by a K-factor of 1.3 to account for higher-order corrections.

Backgrounds

Process	$\sigma(\sqrt{s} = 13 \text{ TeV}) [\text{pb}]$	Order	Generator
$t\bar{t}$	831.76	(NNLO)	(POWHEG-PYTHIA8)
W+Jets ($p_T < 250$)	676.300	(NLO)	(MADGRAPH-PYTHIA8)
W+Jets ($250 < p_T < 400$)	23.94	(NNLO)	(MADGRAPH-PYTHIA8)
W+Jets ($400 < p_T < 600$)	3.0310	(NNLO)	(MADGRAPH-PYTHIA8)
W+Jets ($600 < p_T$)	0.452	(NNLO)	(MADGRAPH-PYTHIA8)
Single Top, s-channel	3.36	(approx. NNLO)	(POWHEG-PYTHIA8)
Single Top, t-channel	44.33	(approx. NNLO)	(POWHEG-PYTHIA8)
Single Top, tW-channel	35.6	(approx. NNLO)	(POWHEG-PYTHIA8)
Single AntiTop, t-channel	26.38	(approx. NNLO)	(POWHEG-PYTHIA8)
Single AntiTop, tW-channel	35.6	(approx. NNLO)	(POWHEG-PYTHIA8)
DY ($H_T < 200$)	139.40	(NLO)	(MADGRAPH-PYTHIA8)
DY ($200 < H_T < 400$)	40.990	(NNLO)	(MADGRAPH-PYTHIA8)
DY ($400 < H_T < 600$)	5.678	(NNLO)	(MADGRAPH-PYTHIA8)
DY ($600 < H_T < 800$)	1.36	(NNLO)	(MADGRAPH-PYTHIA8)
DY ($800 < H_T < 1200$)	0.6759	(NNLO)	(MADGRAPH-PYTHIA8)
DY ($1200 < H_T < 2500$)	0.1160	(NNLO)	(MADGRAPH-PYTHIA8)
DY ($25000 < H_T$)	0.0026	(NNLO)	(MADGRAPH-PYTHIA8)
WW	118.7	(NLO)	(PYTHIA8)
WZ	47.13	(NLO)	(PYTHIA8)
ZZ	16.523	(NLO)	(PYTHIA8)
QCD ($H_T < 200$)	1712000	(NLO)	(MADGRAPH-PYTHIA8)
QCD ($200 < H_T < 400$)	347700	(NNLO)	(MADGRAPH-PYTHIA8)
QCD ($400 < H_T < 600$)	32100	(NNLO)	(MADGRAPH-PYTHIA8)
QCD ($600 < H_T < 800$)	6831	(NNLO)	(MADGRAPH-PYTHIA8)
QCD ($800 < H_T < 1200$)	1207	(NNLO)	(MADGRAPH-PYTHIA8)
QCD ($1200 < H_T < 2500$)	119.9	(NNLO)	(MADGRAPH-PYTHIA8)
QCD ($25000 < H_T$)	25.24	(NNLO)	(MADGRAPH-PYTHIA8)

Table 5.1: SM cross sections (and the order at which they were obtained) of the background processes used in the analysis. The generator packages used to produce these samples are also listed. [69]

Fig. 5.4 shows the invariant mass distribution, Eq. 8.3, of the generated top-antitop quark system of these signal samples. Notice that the wider the resonance the more off-shell production at lower masses occurs.

Z' boson with $\Gamma/M = 1\%$ width			Z' boson with $\Gamma/M = 10\%$ width			Z' boson with $\Gamma/M = 30\%$ width		
$M_{Z'}$ [GeV]	$\sigma(\sqrt{s} = 13 \text{ TeV}) \cdot \text{BR}$ [pb]		$M_{Z'}$ [GeV]	$\sigma(\sqrt{s} = 13 \text{ TeV}) \cdot \text{BR}$ [pb]		$M_{Z'}$ [GeV]	$\sigma(\sqrt{s} = 13 \text{ TeV}) \cdot \text{BR}$ [pb]	
500	56.26983	(NLO)	500	517.74035	(NLO)	500	1281.32347	(NLO)
750	12.99911	(NLO)	750	126.05118	(NLO)	750	345.90321	(NLO)
1000	4.24671	(NLO)	1000	42.24246	(NLO)	1000	122.17487	(NLO)
1250	1.67078	(NLO)	1250	17.03858	(NLO)	1250	51.51389	(NLO)
1500	0.74006	(NLO)	1500	7.74129	(NLO)	1500	24.46373	(NLO)
1750	0.35479	(NLO)	1750	3.82201	(NLO)	1750	12.66093	(NLO)
2000	0.17980	(NLO)	2000	2.00723	(NLO)	2000	6.99950	(NLO)
2250	0.09496	(NLO)	2250	1.10600	(NLO)	2250	4.08126	(NLO)
2500	0.05178	(NLO)	2500	0.63398	(NLO)	2500	2.48821	(NLO)
2750	0.02896	(NLO)	2750	0.37621	(NLO)	2750	1.57672	(NLO)
3000	0.01659	(NLO)	3000	0.23030	(NLO)	3000	1.03387	(NLO)
3250	0.00961	(NLO)	3250	0.14504	(NLO)	3250	0.69914	(NLO)
3500	0.00566	(NLO)	3500	0.09387	(NLO)	3500	0.48624	(NLO)
3750	0.00337	(NLO)	3750	0.06237	(NLO)	3750	0.34698	(NLO)
4000	0.00203	(NLO)	4000	0.04254	(NLO)	4000	0.25352	(NLO)

Z' boson + jet with $\Gamma/M = 10\%$ width

$M_{Z'}$ [GeV]	$\sigma(\sqrt{s} = 13 \text{ TeV}) \cdot \text{BR}$ [pb]	
500	8.5700	(NLO)
750	1.8555	(NLO)
1000	0.5449	(NLO)
1250	0.1919	(NLO)
1500	0.0739	(NLO)
2000	0.0138	(NLO)
2500	0.0030	(NLO)
3000	0.00077	(NLO)
3500	0.00020	(NLO)
4000	0.00005	(NLO)

KK gluon

$M_{g_{KK}}$ [GeV]	$\sigma(\sqrt{s} = 13 \text{ TeV}) \cdot \text{BR}$ [pb]	
500	275.9	(LO)
750	62.41	(LO)
1000	20.05	(LO)
1250	7.92	(LO)
1500	3.519	(LO)
2000	0.9528	(LO)
2500	0.3136	(LO)
3000	0.1289	(LO)
3500	0.05452	(LO)
4000	0.02807	(LO)

Table 5.2: Values of the production cross section times branching ratio to $t\bar{t}$. On top, the NLO values for various Z' signal hypothesis with a relative decay widths ($\Gamma_{Z'}/M_{Z'} = 1\%, 10\%$ and 30%) [71], [72]. On the bottom left, the NLO values for the 1% Z' +jet model [36]. On the bottom right, the LO values for KK gluon excitations where the cross sections are multiplied by a factor of 1.3 to account for higher-order corrections [73].

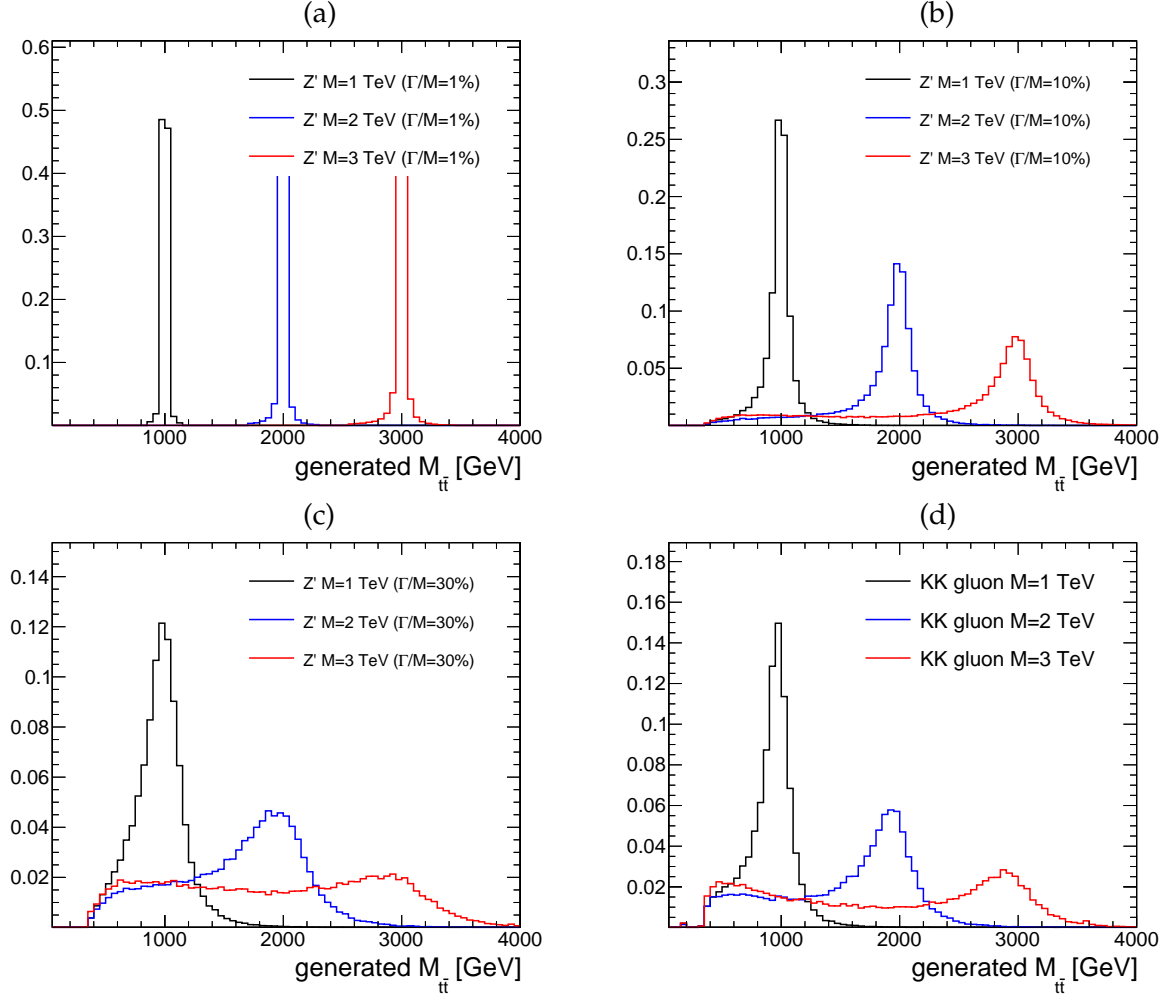


Figure 5.4: Invariant mass of the $t\bar{t}$ system at generator level for the signal models considered in the analysis: (a) Z' boson with a relative width of 1%, (b) Z' boson with a relative width of 10%, (c) Z' boson with a relative width of 30%, (d) Kaluza-Klein excitation of a gluon. The distributions are normalized to unity.

6. EVENT SELECTION

Now that we have given the motivation to search for top-antitop quark resonances, described the experimental set up used to search for them, discussed how to use the detected particles to reconstruct the event, introduced the expected topology of the final state objects, and mentioned the sources of background events, we must now discuss the technicalities of the data analysis.

In this chapter, the dataset used in this work is presented. Then, the physics objects used in this analysis are defined, followed by a description of the kinematic selection employed to filter events of interest. Finally, the corrections applied to MC events to fully emulate the conditions on which the analyzed data was recorded are listed.

6.1 Data

In 2016, the CMS experiment recorded 37.76 fb^{-1} of proton-proton collisions at $\sqrt{s} = 13 \text{ TeV}$. This work only considers the dataset that passes data-quality certification, which corresponds to 35.9 fb^{-1} . Fig. 6.1 shows the delivered, recorded and validated integrated luminosity as a function of time.

6.2 Object Definition

The event reconstruction is based on the PF algorithm described in Chapter 4. In the following paragraphs a more detailed description of the objects used in this analysis is presented.

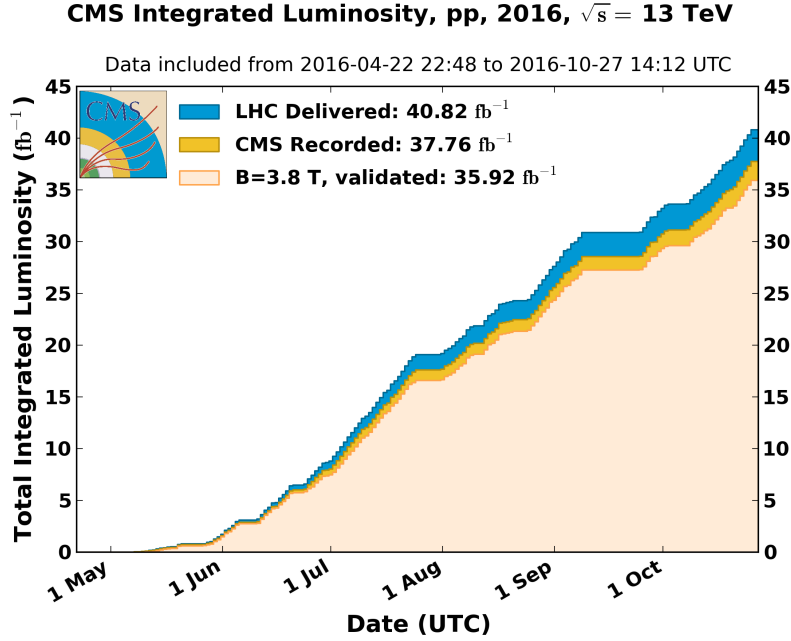


Figure 6.1: CMS integrated luminosity for proton-proton collisions at $\sqrt{s} = 13$ TeV in 2016

Primary Vertex

Primary vertices are reconstructed by clustering tracks with a deterministic annealing algorithm [74], where each vertex candidate must satisfy: $\sqrt{x^2 + y^2} < 2$ cm, $|z| < 24$ cm and the number of tracks used to reconstruct the vertex should be less than four. The vertex candidate with the highest $\sum_i p_T^2(\text{track}(i))$ of clustered objects is identified as the primary vertex.

Muons

The muon candidates used in this analysis are required to satisfy the so-called "Tight" identification (ID), which corresponds to the following:

- The candidate is reconstructed as a global muon
- The candidate is a PF reconstructed muon
- $\chi^2 < 10$ of the global muon track fit
- At least one muon chamber hit included in the global muon track

- Muon segments in at least two muon stations
- At least one hit in the pixel tracker
- To guarantee a good p_T measurement, at least 5 tracker layers must have hits
- The transverse impact parameter and the longitudinal distance of the muon inner track with respect to the primary vertex should be less than 0.2 cm and 0.05 cm, respectively.

This identification criteria provides a high efficiency for prompt muons and a very good rejection rate for non-prompt ones. It should also be pointed out that due to the fact that prompt muons that decay from the high p_T top quarks are expected to be in the near vicinity of the decay products of the b quark decay, no isolation requirements are applied.

Jets and Missing Transverse Energy

Two jet collections are employed in this analysis. Jets are reconstructed with the AK algorithm but for two different choices of the cone parameter $R = 0.4$ (AK4) and $R = 0.8$ (AK8). The AK8 jets are exclusively used to identify jets associated to the hadronic decay leg of the system, whereas AK4 jets can be used for both hadronic and leptonic legs. Both collections are built using all of the PF candidates not marked as pileup-hadrons.

The reconstructed jets have to undergo a series of calibration steps that take into account several experimental constraints like the detector response. Jet Energy Corrections (JEC) enable the proper mapping of the measured jet energy to the energy of the particles. The JEC are applied to the reconstructed jets' 4-momenta by a coefficient that depends on the jets' p_T and η . The first step (JEC-L1) of the JEC is to remove from the jet any extra energy coming from pileup interactions. Then, the reconstructed jets have to be corrected for the non-uniform response of the detector in the η direction (JEC-L2). Next, the non-uniform p_T dependence of the detector response must also be taken into account (JEC-L3). Finally, the so-called residuals (JEC-L2L3) apply a residual calibration in data to fix small differences between the observed and the simulated jets. These levels of correc-

tion can be seen in Fig 6.2. All levels of jet energy corrections are applied in this analysis. In addition, the jet p_T resolution (JER) is relatively poor compared to many other physics

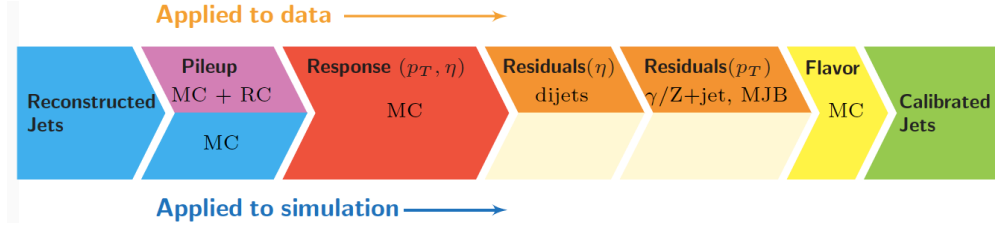


Figure 6.2: Factorized JEC approach where each level of correction takes care of a different effect. The levels of correction are applied sequentially in the shown order.

objects and the biases caused by smearing can be important for steeply falling spectra and for resonances decays. Jets are corrected for JEC before deriving the JER corrections. The measurement of this correction is an extension of the methods used for the JEC, but instead of looking at the mean of the response distribution, this time the width is the important quantity.

Finally, the jet energy corrections mentioned above are propagated to the missing transverse energy as follows:

$$\vec{E}_{corrected} = \vec{E}_{raw} + \sum_i p_{T,i,raw} - \sum_i p_{T,i,corrected} - \sum_i \vec{O}_{PU} \quad (6.1)$$

Jet Tagging

The CMS collaboration has developed several algorithms that allow to identify or tag the flavor of the jets, i.e., which quark started the hadronization. The two tagging algorithms in this work are "*b*-tagging" and "top-tagging".

To discriminate between *b*- and light-jets, a variety of reconstructed objects such as tracks, vertices and identified leptons can be used. The long lifetime of the *b* quark, allowing it to travel several millimeters before decaying, is a key property exploited for *b*-tagging. This allows to reconstruct a secondary vertex.

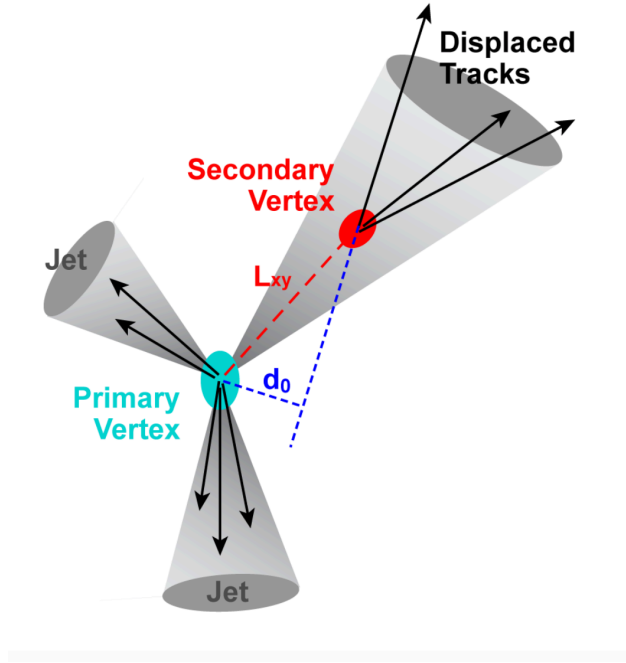


Figure 6.3: Diagram of the characteristic parameters used for b -tagging

The b -tagging algorithms require well-reconstructed tracks of high purity and specific requirements are imposed in addition to the selection applied in the tracking step during track reconstruction:

- At least eight hits must be associated with the track,
- At least two hits are required in the pixel system, since track measurements in the innermost layers provide most of the discriminating power
- A loose selection on the track impact parameters L_{xy} and d_0 , defined as the transverse and longitudinal distance to the primary vertex at the point of closest approach in the transverse plane, Fig. 6.3. These are used to further increase the fraction of well-reconstructed tracks and to reduce the contamination by decay products of long-lived particles, e.g. neutral kaons.

The Combined Secondary Vertex (CSV) algorithm combines the information of the displaced tracks with the information of the secondary vertices associated to the jet using a multivariate technique [75]. An updated version of this algorithm (CSVv2) [76] is the one employed in this work to b -tag jets. The CSV discriminator variable produced by this

algorithm lies within a range from zero to one, the closest to one means that the jet is indeed a b -jet. Working-points in this discriminator variable can be defined depending on the rate of misidentifying a light-jet as a b -jet. A b -jet is defined in this work based on the so-called Medium (CSVv2M) working-point that accepts only jets whose CSV discriminator value is higher than 0.8, which corresponds to a 1% misidentification rate and 67% b -tagging efficiency.

The employment of substructure variables that describe the internal composition of boosted jets is a key element in this analysis, namely in the algorithm used to tag top-jets. The two properties employed in this analysis to tag top-jets are soft-drop mass declustering and N -subjettiness.

Soft-drop declustering [77] is a technique that recursively removes soft wide-angle radiation from a jet and it depends on two parameters: an angular exponent β and a soft threshold z_{cut} . This iterative algorithm can be summarized as follows:

- Given a jet of radius R_0 , recluster the jet to form a pairwise angular-ordered structure
- Break the jet j into two subjets j_1, j_2 by undoing the last stage of the clustering.
- Check if the subjets pass the soft-drop condition:

$$\frac{\min(p_{T,1}, p_{T,2})}{p_{T,1} + p_{T,2}} > z_{cut} \left(\frac{\Delta R_{1,2}}{R_0} \right)^\beta \quad (6.2)$$

- If they do not pass the condition, redefine j to be equal to the subjet with larger p_T and iterate the procedure
- If j can no longer be declustered, then j is the final soft-drop jet.

The jet shape variable N -subjettiness [78], denoted by τ_N , is designed to identify boosted hadronically-decaying objects like top-quarks which, if combined with a jet mass cut, can be extremely discriminating. For example, when a boosted top-quark decays hadronically in a single jet, it should be composed of three distinct – but not necessarily

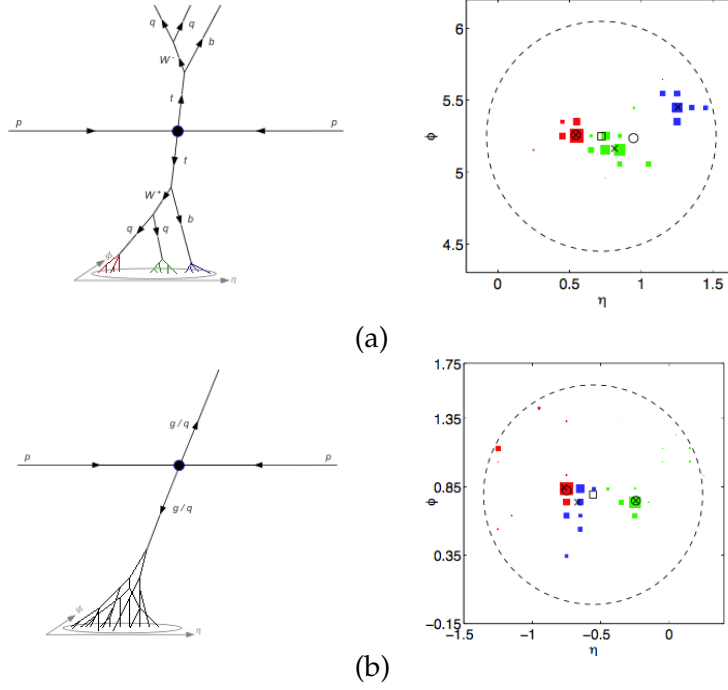


Figure 6.4: Hadronic decays of: (a) $t\bar{t}$ and (b) NTMJ dijet events. The cells are colored according to how the jet is divided into three subjets. The square indicates the total jet direction, the circles indicate the two subjets direction and the crosses indicate the three subjet directions. The discriminating variable τ_{32} measures the relative alignment of the jet energy along the crosses compared to the circles [78].

resolved– hard subjets with a combined invariant mass around 172 GeV. On the other hand, when a jet product of a Non-Top Multijet (NTMJ) event with the same invariant mass originates, it emerges from a single hard parton and acquires mass through large angle splittings. τ_N exploits this difference in the expected energy flow to differentiate between these two type of jets by counting the number or hard lobes of energy, as shown in Fig 6.4

N -subjettiness, is calculated as

$$\tau_N = \frac{1}{d_o} \sum_k p_{T,k} \min(\Delta R_{1,k}, \Delta R_{2,k}, \dots, \Delta R_{N,k}) \quad (6.3)$$

where k runs over the constituent particles in the jet, $p_{T,k}$ are their respective transverse momenta and $\Delta R_{J,k}$ is the separation between a candidate subjet J and a constituent particle k . The normalization factor is taken as

$$d_o = \sum_k p_{T,k} R_0 \quad (6.4)$$

here R_0 is the characteristic jet radius used in the clustering algorithm. Thus, it can be seen that τ_N quantifies how many subjets a particular jet contains. The ratio between a jet being likely to contain three subjets (τ_3), to it containing two (τ_2), is defined as $\tau_{32} = \tau_3/\tau_2$ and it is very effective to discriminate top-jets from NTMJ-jets.

Therefore, to top-tag a jet in this analysis, a combination of a cut on the soft-drop mass of the jet and the N -subjettiness ratio τ_{32} is used. Specifically, a jet would be top-tagged when: $105 \text{ GeV} < M_{sd} < 220 \text{ GeV}$, where M_{sd} is the soft-drop mass of the AK8 jet and $\tau_{32} < 0.67$.

6.3 Kinematic Event Selection

As mentioned before, we only consider cases where the final state objects contains a muon, missing transverse energy and jets, "muon+jets" channel. The event selection is described next.

6.3.1 Muon+jets Channel

At trigger level we require events that fire the `HLT_Mu50` combined in a logical "OR" with `HLT_TrkMu50`. These HLT paths were the lowest p_T unprescaled trigger available that did not have isolation requirements on the muon at trigger level. This trigger determines the p_T^μ cut applied next.

Offline, we select events with:

- Exactly one muon with $p_T^\mu > 55 \text{ GeV}$ and $|\eta| < 2.4$;
- Veto on additional muons or electrons;
- At least one AK4 jet with $p_T > 50 \text{ GeV}$ and $|\eta| < 2.4$;
- At least one AK4 jet with $p_T > 150 \text{ GeV}$ and $|\eta| < 2.4$;

- If an AK8 jet is found it is required to have $p_T > 500 \text{ GeV}$ and $|\eta| < 2.5$ and veto additional AK8 jets;
- $p_T^{miss} > 50 \text{ GeV}$;
- The event is accepted if either $\Delta R(\mu, j) > 0.4$ or $p_{T,rel}(\mu, j) > 20 \text{ GeV}$, where j stands for the nearest jet to the muon. The quantity $p_{T,rel}(\mu, j)$ is the relative transverse momentum of the muon with respect to the jet. This selection is called "2D-cut" and effectively reduces QCD multi-jet background more effectively without compromising the signal efficiency;
- $H_{T,lep} \equiv p_T^{miss} + p_T^\mu > 150 \text{ GeV}$.

6.4 Corrections to the Simulated Events

To take into account any differences between the recorded data and the simulated events, a number of corrections have to be applied. These take the name of scale factors (SF) because they attempt to scale the MC events to match the observed data. In this work, SFs were applied to try to correct for: pileup, trigger efficiencies, lepton identification efficiencies, b -tagging efficiency, and t -tagging efficiency.

6.4.1 Pile-up SF

The MC samples were generated beforehand the true data-taking pileup conditions were known. Each MC sample is reweighed such that the number of true pileup interactions in simulation matches the instantaneous luminosity profile in data with a minimum-bias cross section of 69.2 mb . Fig. 6.5 shows how this SF improves the shape of the number of primary vertices distribution.

6.4.2 Lepton ID SF

To measure the lepton identification efficiency in data and MC a dilepton control region is created. In particular the leptonic decay of Z bosons, $Z \rightarrow \ell\ell$, is the control region

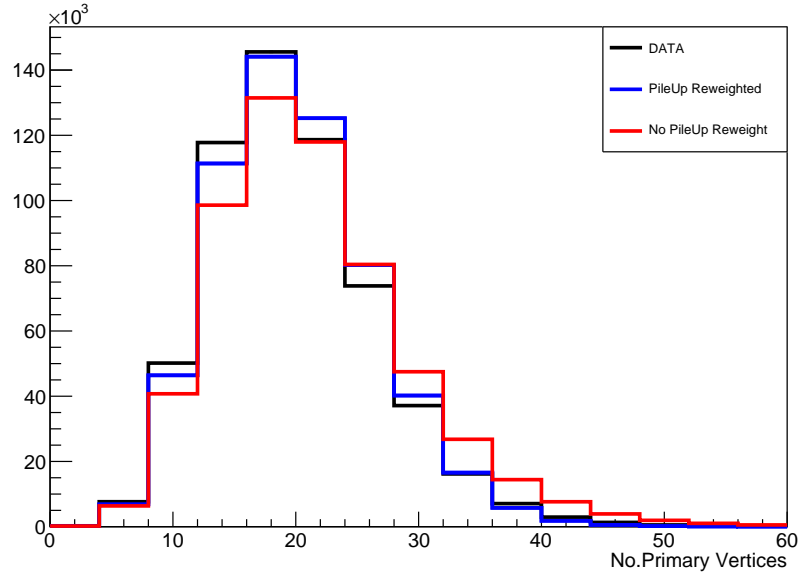


Figure 6.5: Effect of the Pile-up reweighting on a simulated $t\bar{t}$ sample after the baseline selection has been applied. The distributions have been scaled to the same area to highlight the shape comparison.

chosen. Events that contain two leptons whose reconstructed mass lies within the Z peak are used to measure the lepton identification efficiencies. One lepton – the tag – is required to pass very pure identification requirements, whereas the other lepton – the probe – is only required to pass loose identification requirements. Given that an event contains a tag candidate, then there could be a passing or failing probe. In both cases, the events are fit separately to the expected shape from the Z peak. The efficiency is computed from the ratio of the passing probes to the sum of passing and failing probes. The obtained SF values are obtained as a function of the muon's p_T and η , as seen in Fig.6.6.

6.4.3 Trigger SF

To account for the difference of the trigger performance in MC samples and data, a SF is applied. The scale factors for the muon trigger have been measured using the tag-and-probe approach mentioned in the previous section and are given as a function of the muon η and p_T , Fig 6.7.

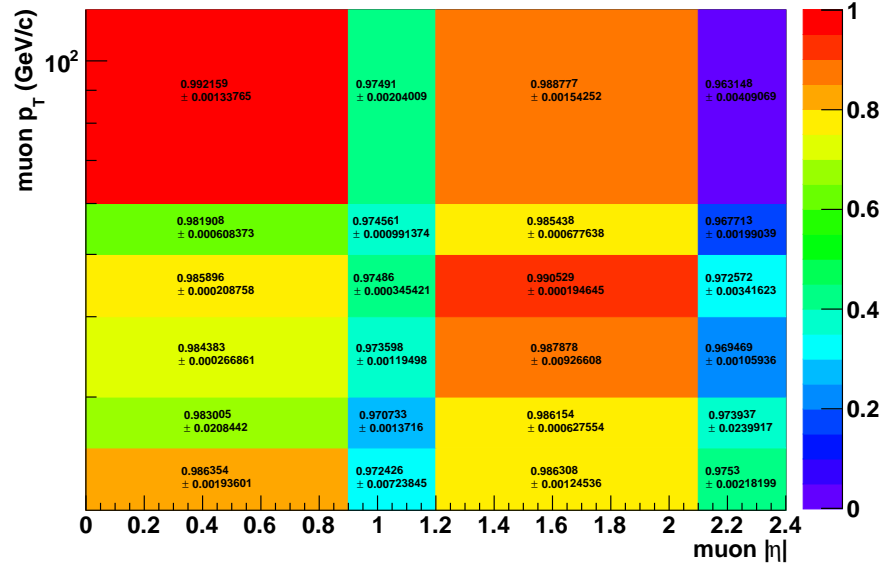


Figure 6.6: Scale Factors applied to the MC samples to take into account differences for the muon ID efficiency. These are given as a function of the muon p_T and η .

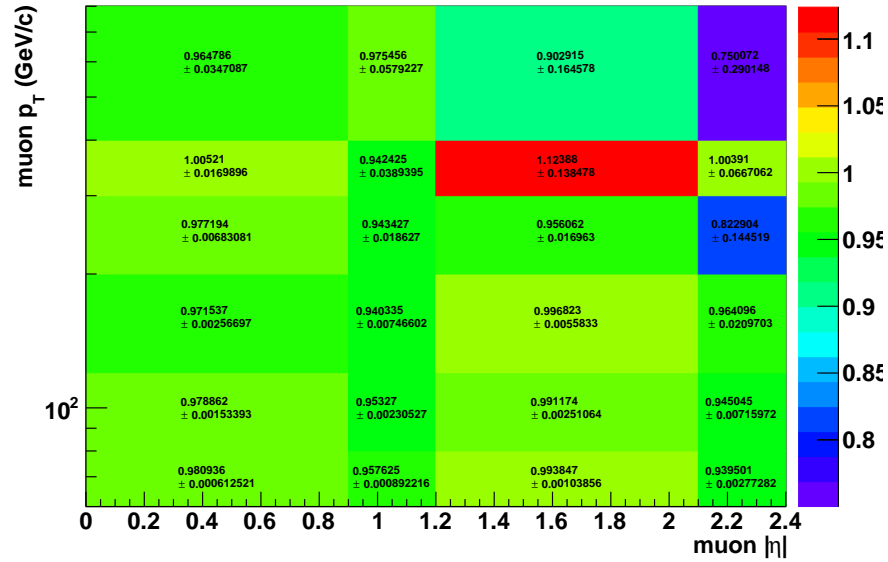


Figure 6.7: Scale Factors applied to the MC samples to take into account differences for the muon HLT efficiency. These are given as a function of the muon p_T and η .

6.4.4 b -tagging SF

The efficiency of the CSV algorithm used to identify b quarks has been extensively studied by the CMS collaboration. It depends on the p_T of the jets and their flavor (f): b -flavored jets, c -flavored jets, or light-flavored jets including jets originating from gluons. In this analysis, a SF is used to correct for discrepancies between the b -tagging efficiency of a jet in data and in simulated events. The SFs of tagging and not tagging a jet are derived as follows:

$$SF_{tagged}(f, p_T) = \frac{\epsilon_{data}(f, p_T)}{\epsilon_{MC}(f, p_T)} \quad , \quad SF_{untagged}(f, p_T) = \frac{1 - SF_{tagged}(f, p_T)\epsilon_{MC}(f, p_T)}{1 - \epsilon_{MC}(f, p_T)}. \quad (6.5)$$

These expressions summarize the b -tagging efficiency SF and the b -tagging mistag rate SF. Thus, for an event with N_{tagged} tagged and $N_{untagged}$ untagged jets, the total SF is given by

$$SF_{b-tagging} = \prod_i^{N_{tagged}} SF_{tagged}(f_i, p_{T,i}) \times \prod_j^{N_{untagged}} SF_{untagged}(f_j, p_{T,j}). \quad (6.6)$$

6.4.5 top-tagging SF

Similarly to the b -tagging section, in order to account for possible differences between data and MC for the performance of the top-tagging algorithm, MC events are reweighted using the SF formula of Eq.6.6. The quantities needed to determine such value are the t -tagging efficiencies in MC for light- and top-flavor jets. We call top-mistag rate the efficiency of the top-tagging algorithm on AK8 jets associated to the decay of a light quark.

The top-tagging efficiency scale factor, SF_{tagged} , is introduced as a free nuisance parameter in the statistical analysis since the selection of a control sample without overlapping with the signal region of this analysis is not feasible. On the other hand, the top-mistag rate SF, $SF_{untagged}$, can be derived from a control region (CR) dominated by W +jets production. This CR is defined by the following criteria:

- Same selection criteria of Sec. 6.3
- At least one AK8 jet with $p_T > 500$ GeV
- Veto events with at least one AK4 jet passing the CSVM b -tagging working point
- χ_ℓ^2 of Eq. 8.2 should be greater than 30

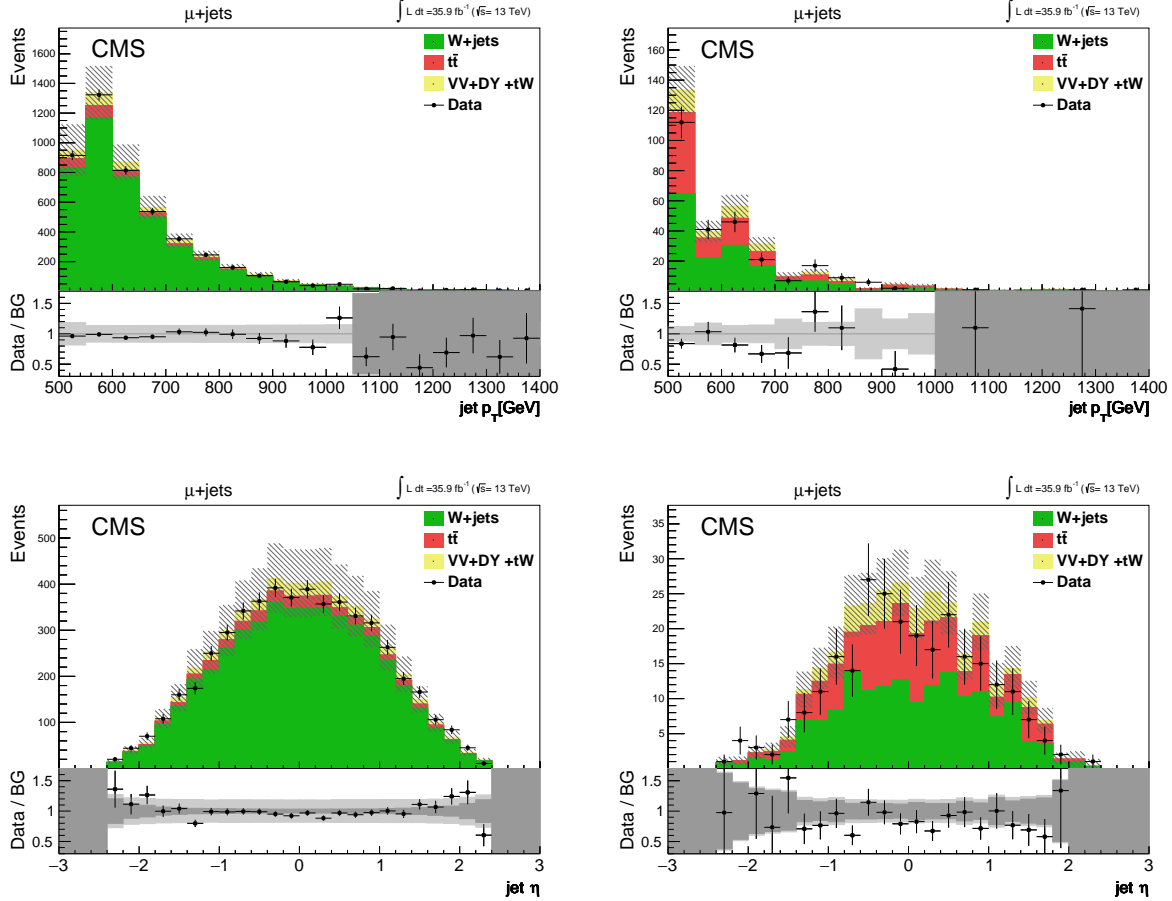


Figure 6.8: Data/MC distributions for the AK8 jets with $p_T > 500$ GeV and $|\eta| < 2.4$. In the CR used for the top-mistag rate measurement: (from top to bottom) jet p_T , jet η , jet mass. Plots for the μ +jets before any top-tagging requirement (after the top-tagging requirements) CR are shown on the left (right). The bottom plot of each figure shows the ratio of data over MC.

The inverted χ_ℓ^2 criteria ensures that this CR is disjunct to the signal region (SR) discussed in Chapter 7. The b -tag veto guarantees a sample dominated by W +jets as seen in Fig. 6.8. In events in which at least one AK8 jet is top-tagged, W +jets still accounts for most of the sample but the fraction of SM $t\bar{t}$ becomes non-negligible, Fig.6.8. For this rea-

son, when measuring the top-mistag rate in data, we subtract from the latter the expected yield for SM $t\bar{t}$ production

$$\epsilon_{mistag} = \frac{N_{data}^{tagged} - N_{t\bar{t}}^{tagged}}{N_{data} - N_{t\bar{t}}}, \quad (6.7)$$

where N_{data} ($N_{t\bar{t}}$) is the number of AK8 jets in this control sample for data (SM $t\bar{t}$ MC sample) and N_{data}^{tagged} ($N_{t\bar{t}}^{tagged}$) correspond to the number of those AK8 jets that are top-tagged in data (SM $t\bar{t}$ MC sample).

The values of the efficiencies in both, data and MC, are listed in Table 6.1 together with the SF.

top-mistag channel	ϵ_{data}	ϵ_{MC}	SF
μ +jets	0.031 ± 0.003	0.039 ± 0.002	0.805 ± 0.102

Table 6.1: top-mistag rates in data and MC and the corresponding SFs for AK8 jets in the W +jets control sample. The uncertainty is only statistical.

6.5 Kinematic Distributions

Figs. 6.9 - 6.10 show data/MC comparisons for events passing the selection described in Sec.6.3.1. The MC events have been corrected using all of the SFs described in the previous section.

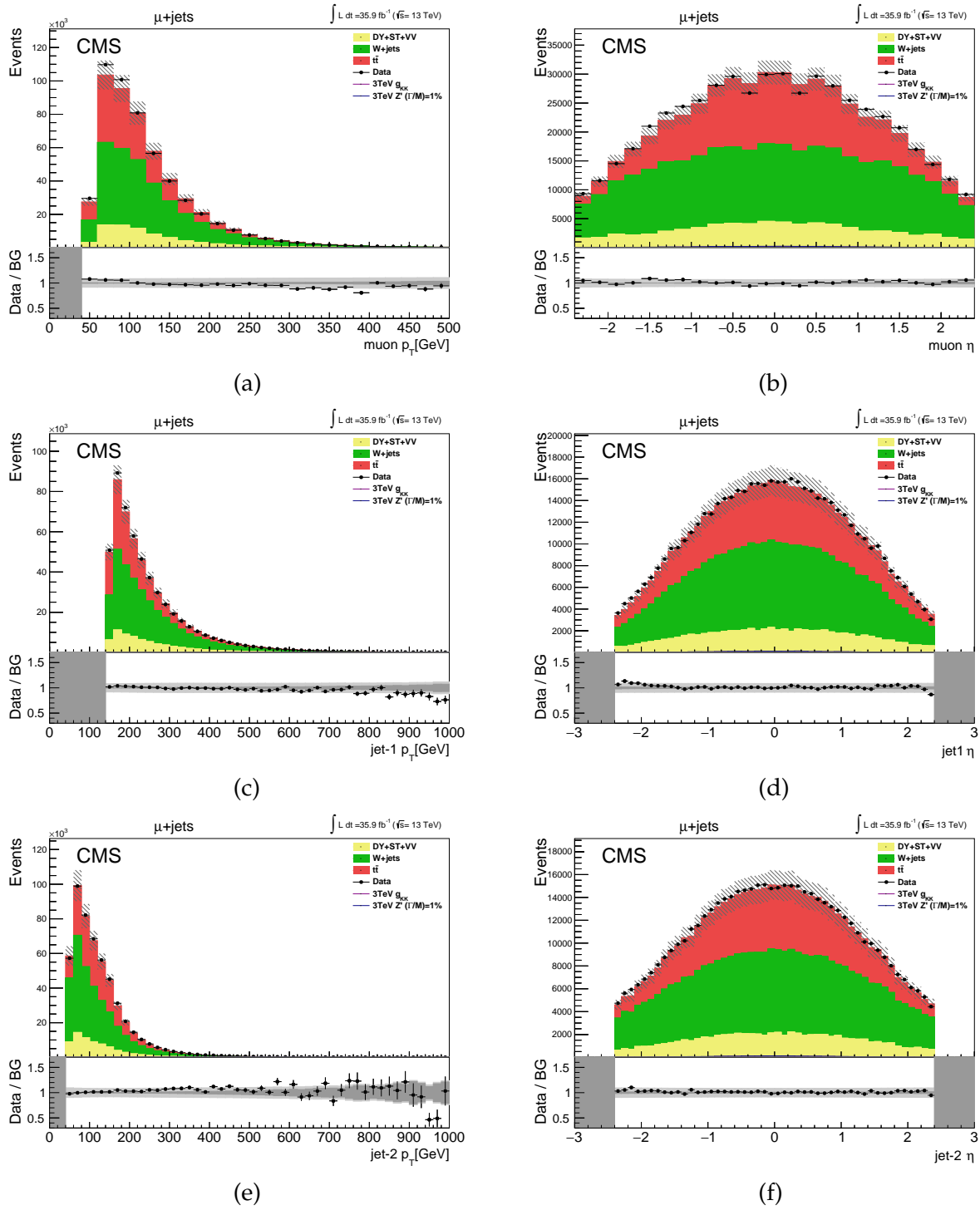
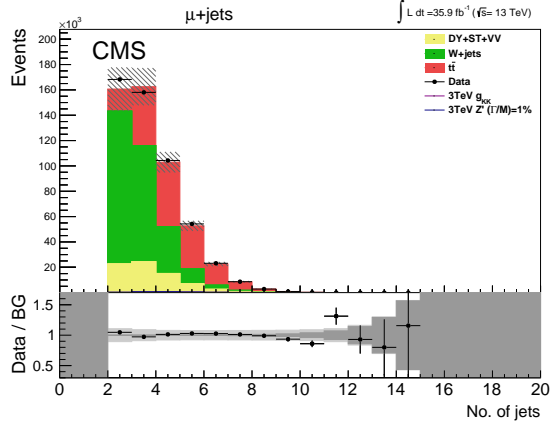
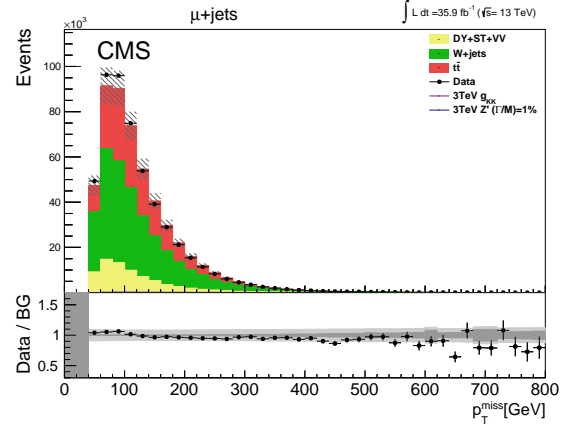


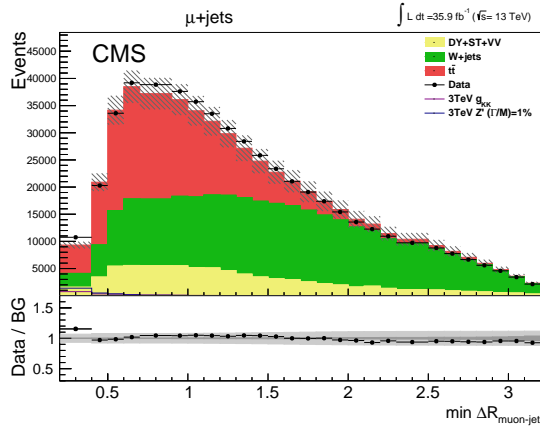
Figure 6.9: Data/MC comparison for (a) muon p_T , (b) muon η , (c) leading jet p_T , (d) leading jet η , (e) sub-leading jet p_T and (f) subleading jet η . The yields of the background processes are normalized to data using scale factors described in 8.2 and the signal MC samples are normalized to a cross section of 1 pb. The shaded band represents the MC statistical uncertainty and the uncertainty on the SM cross section.



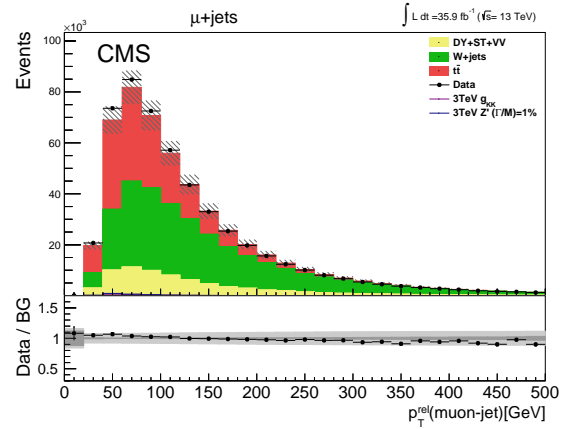
(g)



(h)



(i)



(j)

Figure 6.10: Data/MC comparison for (g) p_T^{miss} , (h) jet multiplicity, (i) ΔR_{min} and (j) $p_{T,rel}$. The yields of the background processes are normalized to data using scale factors described in 8.2 and the signal MC samples are normalized to a cross section of 1 pb. The shaded band represents the MC statistical uncertainty and the uncertainty on the SM cross section.

7. BOOSTED DECISION TREES FOR W +JETS SUPPRESSION

Following the baseline selection, more complex algorithms are needed to effectively reduce background sources. Machine-learning algorithms have proven to be a very powerful tool to handle complex categorization or regression tasks when multiple variables are needed to describe the events. Given that we have simulated events, we can clearly label an event as background or signal. Thus, it is suitable to use a supervised machine-learning algorithm. Supervised algorithms consist of a target or outcome variable which is to be predicted from a set of predictors from labeled training data.

In this chapter, the application of Boosted Decision Trees to reject W +jets events is described.

7.1 Introduction to Decision Trees

Among the several supervised machine-learning algorithms available, in this work we employ Decision Trees (DTs). A DT is a non-parametric method used for classification and also for regression that requires very little data preparation. It is able to handle both, categorical and numerical data. An schematic representation of a DT is shown in Fig.7.1 and its description is as follows:

- Start at the root of the tree with set of n events that are labeled as signal or background. Each event has a list of ℓ characteristic variables. A DT recursively partitions the data such that the events with the same labels are grouped together. Let's represent the events with ℓ dimensional vectors, \vec{x} , and associate them with their corresponding label, $y = B$ if it is a background event, or $y = S$ if it is a signal event.

- At the node m , we split the events based on variable j at a threshold c_m , which we define as $\xi = (j, c_m)$,

$$\begin{aligned} Q_{left}(\xi) &= (x, y) \mid x_j \leq c_m \\ Q_{right}(\xi) &= Q - Q_{left}, \end{aligned} \tag{7.1}$$

where Q represents the events available at node the m -th node of the tree.

- To select the threshold c_m and feature j that optimizes the separation given N_m events at node m , we first look at the impurity, defined as

$$G(Q, \xi) = \frac{n_{left}}{N_m} H(Q_{left}(\xi)) + \frac{n_{right}}{N_m} H(Q_{right}(\xi)), \tag{7.2}$$

where $H = \sum_k p_{m,k}(1 - p_{mk})$, and $p_{m,k}$ is the proportion of class k observations in node m , this is called the "Gini" impurity function. Next, we select the parameters that minimize the impurity, $\bar{\xi} = \operatorname{argmin}_{\xi} G(Q, \xi)$.

- Finally, recurse the subsets $Q_{left}(\bar{\xi})$ and $Q_{right}(\bar{\xi})$ until you reach the maximum allowable depth.

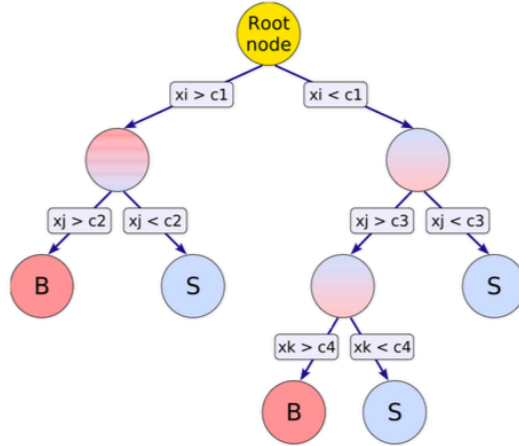


Figure 7.1: Schematic of a decision tree. This algorithm recursively partitions the data such that the events with the same labels are grouped together.

7.1.1 Boosted Decision Tree (BDT)

A BDT consists of an ensemble of DTs. The goal of ensemble methods is to combine the predictions of several base estimators in order to improve robustness. Boosting a DT is done as follows:

- Starts with unweighted events and build DTs as mentioned above.
- If at the end of the training an event is misclassified, then the weight of that event is increased (boosted).
- A second DT is built using the new weights (no longer equal) and we repeat the previous step. The process stops when the desired level of purity in the leaves is achieved.

There are different types of boosting based on the way the weights are updated in each iteration. In this work we use the AdaBoost [79].

7.2 BDT for W +jets Suppression

The most significant background source besides SM $t\bar{t}$ is W +jets. Jets in $t\bar{t}$ events are direct product of the top pair decay, while jets in W +jets events are produced in association with the W boson or from initial or final state radiation (ISR, FSR). For this reason the following jet-related variables are exploited to suppress this background:

- The number of jets;
- The reconstructed mass of the leading and sub-leading jet;
- $S_T \equiv H_T + H_{T,lep}$, where H_T represents the scalar sum of the p_T of the jets in the event;
- The CSV score of the leading and sub-leading jet;
- The shape variable S^{33} of the sphericity tensor $S^{\alpha\beta} = \frac{\sum_i p_i^\alpha p_i^\beta}{\sum_i |p_i|^2}$, where α, β correspond to the x, y , and z components of the momentum vectors of the jets;
- $\Delta R_{min}(\ell, j)$, the separation between the lepton and its closest jet;

- $p_{T,rel}(\ell, j)$, as introduced in Sec. 6.3.1;
- $\Delta R_{min}(\ell, j) \times p_T(j)$.

The reconstructed mass of the leading and sub-leading jets, S_T , $p_{T,rel}$, and $\Delta R_{min}(\ell, j) \times p_T(j)$ are normalized by the mass of the reconstructed $t\bar{t}$ system (these normalized variables will be denoted with a bar) . This is done to avoid introducing a mass bias during the BDT training.

7.2.1 BDT Training, Optimization and Validation

The ROOT TMVA package [80] along with scikit-learn python package [81] are used to perform the training, optimization and testing of the BDT.

For the BDT training, W +jets MC events were used as the background source, whereas all the different MC signal samples (Z' and g_{KK}) with different mass values were used as the signal source. The events were reweighted such that the ratio of background-to-signal events in the training sample was 50:50. The separation of the distributions of the selected variables used in this BDT approach can be seen in Fig. 7.2-7.3 .

The performance of the BDT was tested in depth. Hyper-parameters are parameters that are not directly learnt within estimators. But rather, they are passed as arguments to the constructor of the estimator classes. These are important to tune to achieve an optimal performance and avoid overtraining. We tuned four parameters that impact the BDT performance: the ada-boost, the number of trees, the maximum depth and the minimum samples per leaf. This was done via a grid-search method that tunes in parallel the values and returns those that provide the highest score. Fig 7.4 shows a 2D plot of the score as a function of pairs of variables.

To estimate how accurately this predictive model performs, we use a technique called cross-validation. The goal of this technique is to define a dataset to test the model in the training dataset in order to limit problems like overfitting and give an insight on how the model generalizes independent of the dataset. To perform the cross-validation, the data

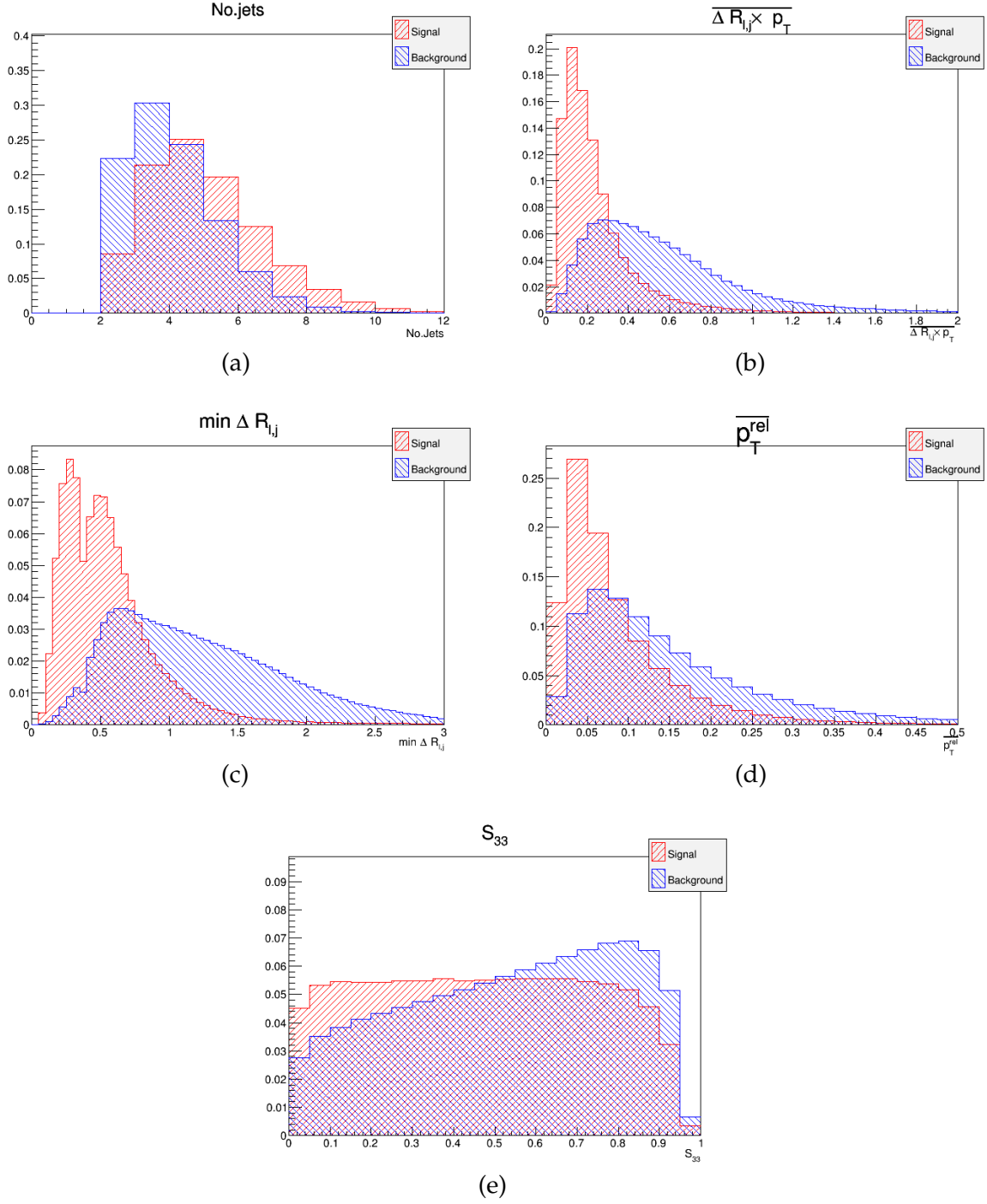


Figure 7.2: Separation between background and signal events of the variables used for the BDT training: (a) No. of jets, (b) $\overline{\Delta R_{min}(\ell, j)} \times p_T(j)$, (c) $\Delta R_{min}(\ell, j)$, (d) $\overline{p_{T,rel}(\ell, j)}$, and (e) S_{33} . The distributions are normalized to the total number of events of each sample. The variables denoted with a bar are normalized by the mass of the reconstructed $t\bar{t}$ system to avoid introducing a mass bias during the BDT training.

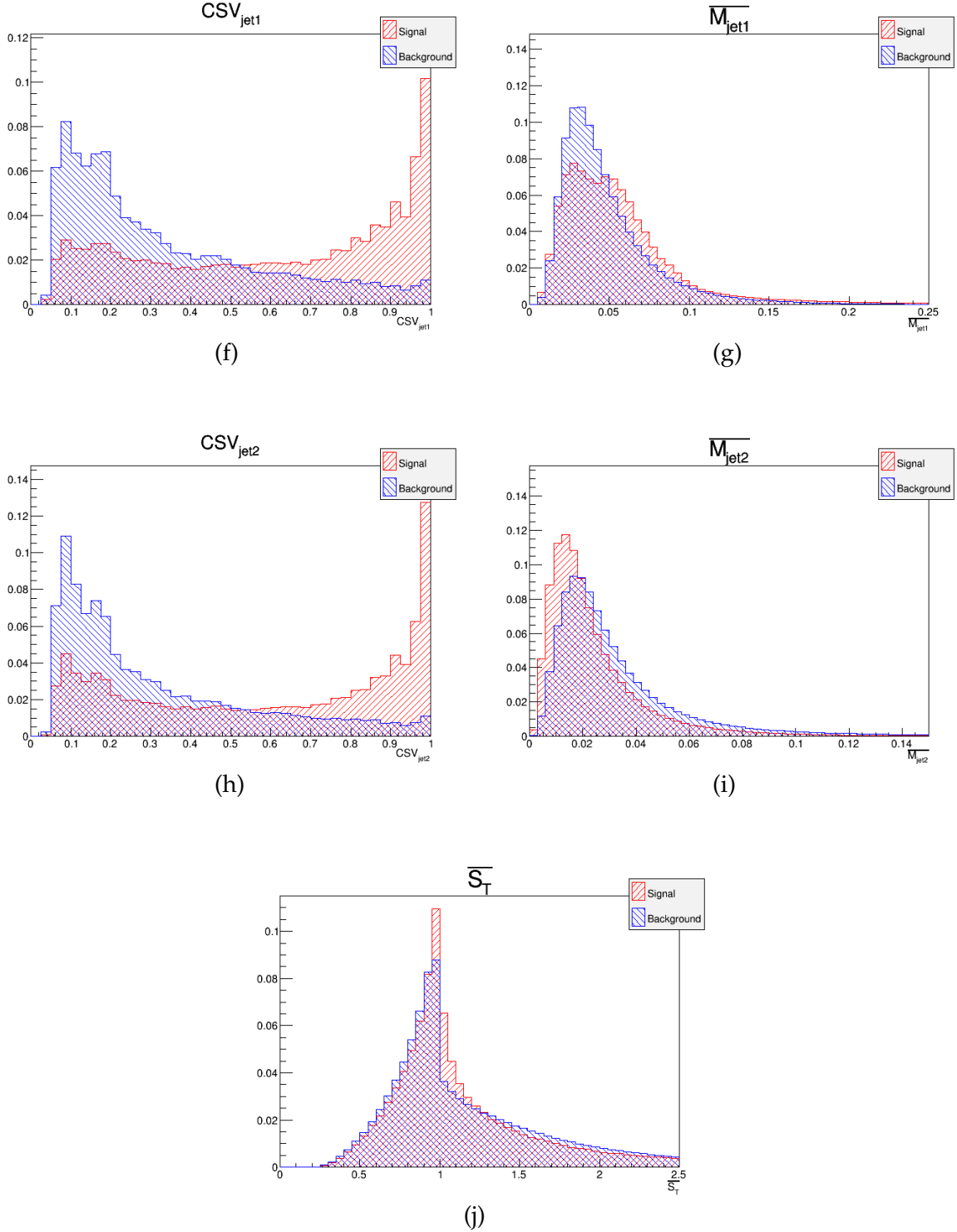


Figure 7.3: Separation between background and signal events of the variables used for the BDT training: (f) CSV score of leading jet, (g) $\overline{M}(j_1)$, (h) CSV score of sub-leading jet, (i) $\overline{M}(j_2)$, and (j) \overline{S}_T . The distributions are normalized to the total number of events of each sample. The variables denoted with a bar are normalized by the mass of the reconstructed $t\bar{t}$ system to avoid introducing a mass bias during the BDT training.

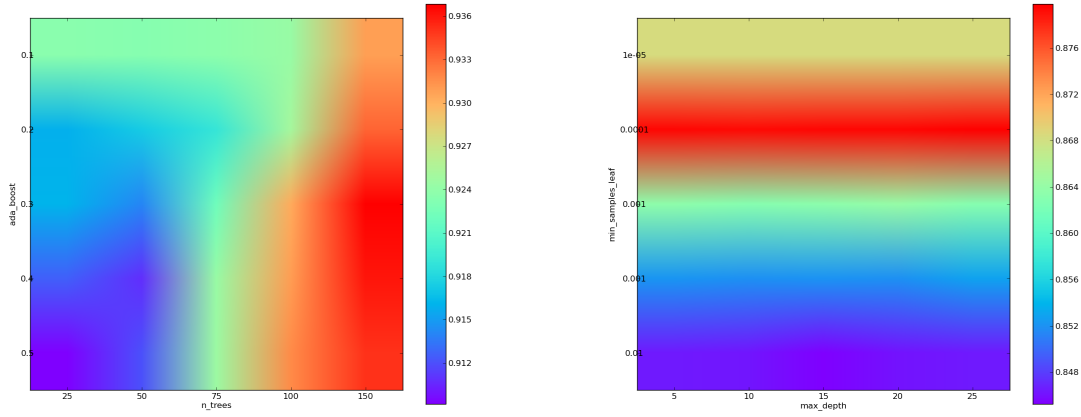


Figure 7.4: Score map of pairs of hyper-parameters used in the BDT training. On the left, the score is shown as a function of the ada-boost vs. the number of trees. On the right, the score is shown as a function of the minimum samples per leaf vs. the maximum depth per tree.

is partitioned into k complementary subsets (or folds), performing the analysis on $k - 1$ subsets, and validating the analysis in the remaining subset. This process repeats until each of the k folds is tested, see Fig.7.5. In summary, cross-validation averages measures of prediction error to derive a more accurate estimate of model prediction performance.

Using 10 folds the performance of this BDT was cross-validated. For each fold, the Receiver Operating Characteristic (ROC) curve and the area under this curve (AUC), were obtained. The ROC curve is created by plotting the true positive rate (TPR) against the false positive rate (FPR) at various threshold settings, thus the AUC is a measure of the accuracy of the BDT. As seen in Fig.7.6, the Receiver Operating Characteristic (ROC) curve for all folds are in agreement with each other and an average AUC ≈ 0.95 was obtained.

The distribution of the classifier variable, called "response", that the BDT outputs lies between -1 (background-like) and 1 (signal-like). The BDT response was obtained for the testing and training samples and a very good separation between background and signal events was observed, Fig.7.7.

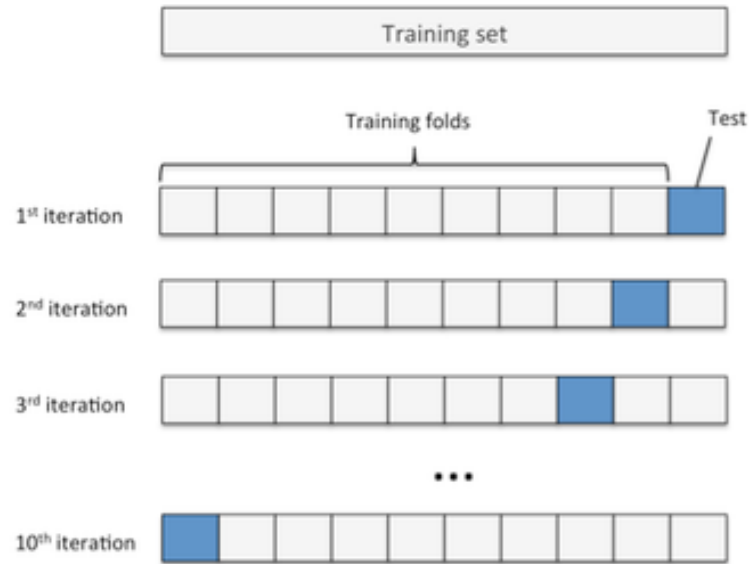


Figure 7.5: Schematic of a k -fold validation process. The data is partitioned in k complementary subsets, the training is done in $k - 1$ subsets and then tested on the remaining subset. This process is repeated until each the BDT is tested on each of the k subsets. For each subset, the accuracy of the BDT is measured.

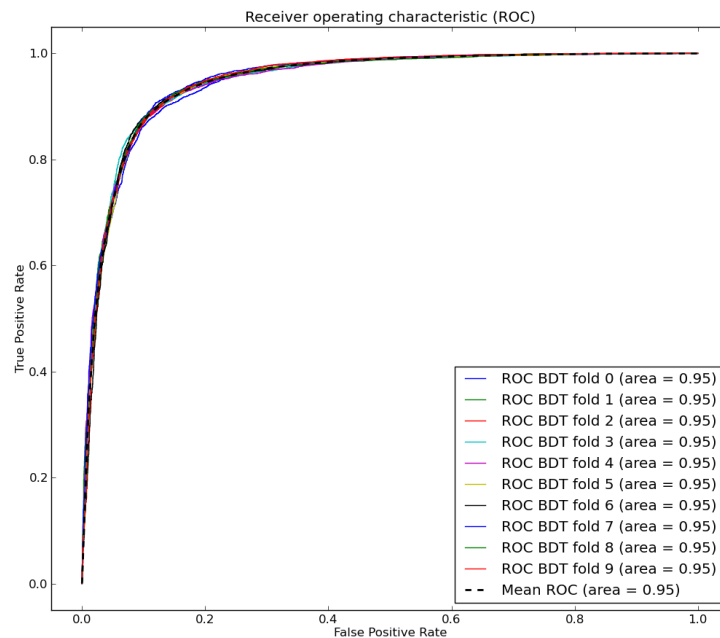


Figure 7.6: ROC curves for each of the 10 folds use to validate the performance of the BDT. All folds are in agreement with each other, showing a solid BDT training. The mean AUC was found to be 0.95.

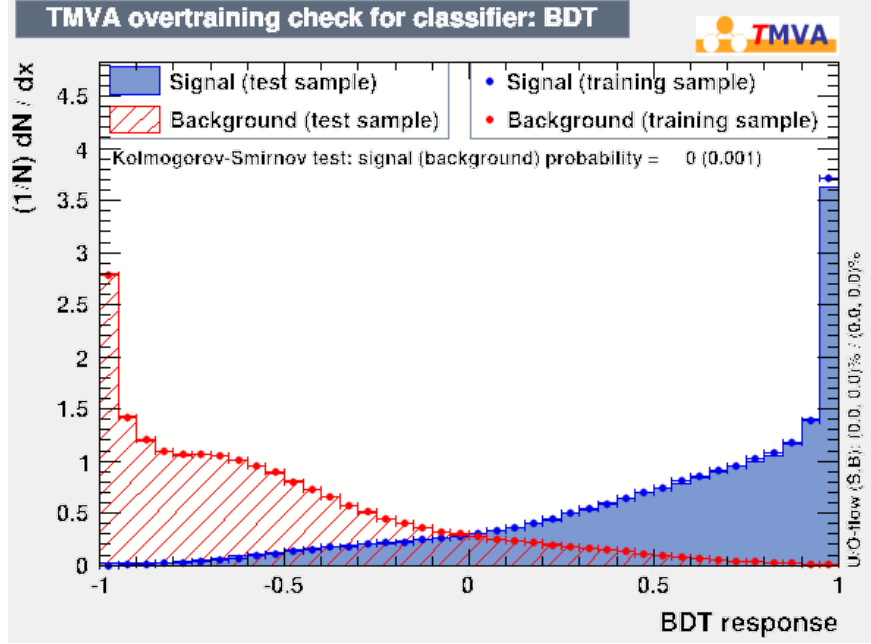


Figure 7.7: BDT classifier output distributions for signal and background events. Compatibility between dots (testing data) and histograms (training data) indicates that overtraining is not a problem.

7.2.2 BDT performance in Data and MC

As a last step, it is important to certify the performance of the BDT in data and in the background MC samples. Figs. 7.8-7.9 show the agreement between data and MC of the variables used in the BDT for events that passed the baseline selection of Sec. 6.3.1. In addition, a Kolmogorov-Smirnov (K-S) test [82] is used to compare these distributions and to ensure that only well modeled variables are used in the BDT. The values of such test are summarized in Table 7.1. The K-S statistic for all variables is low and none of them has a p-value lower than 0.05.

Fig. 7.10 shows the BDT response distribution. Based on this, we define the following working points; loose (BDT-L), corresponding to $\text{BDT} \geq -0.5$; medium (BDT-M), corresponding to $\text{BDT} \geq 0.0$; and tight (BDT-T), corresponding to $\text{BDT} \geq 0.5$. These working points mitigate the W +jets contamination approximately by 33%, 66%, and 90%,

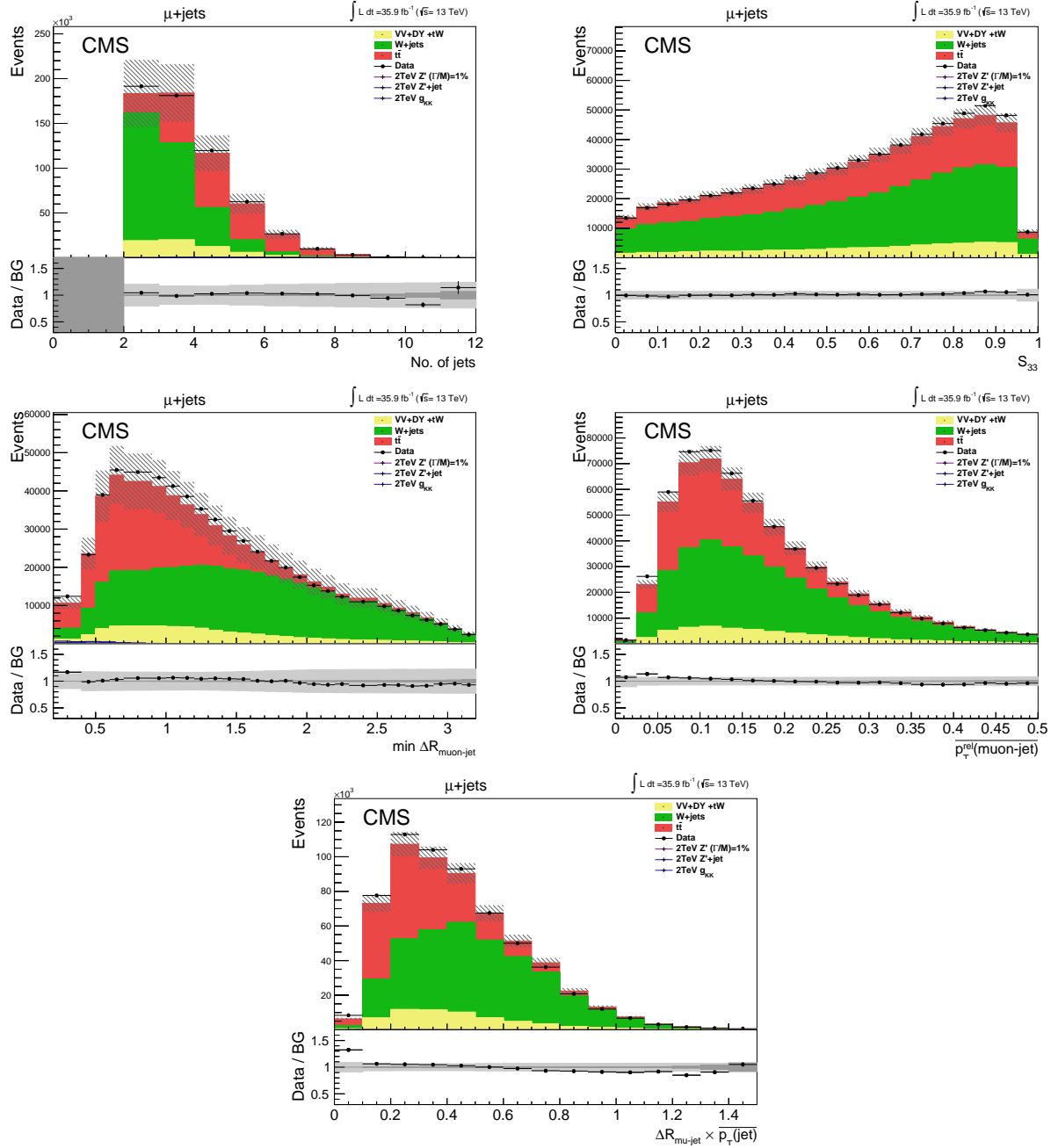


Figure 7.8: Data/MC comparison for the variables used in the BDT. The variables denoted with a bar are normalized by the mass of the reconstructed $t\bar{t}$ system. The yields of the background processes are normalized to data using scale factors described in 8.2 and the signal MC samples are normalized to a cross section of 1 pb. The shaded band represents the MC statistical uncertainty and the uncertainty on the SM cross section.

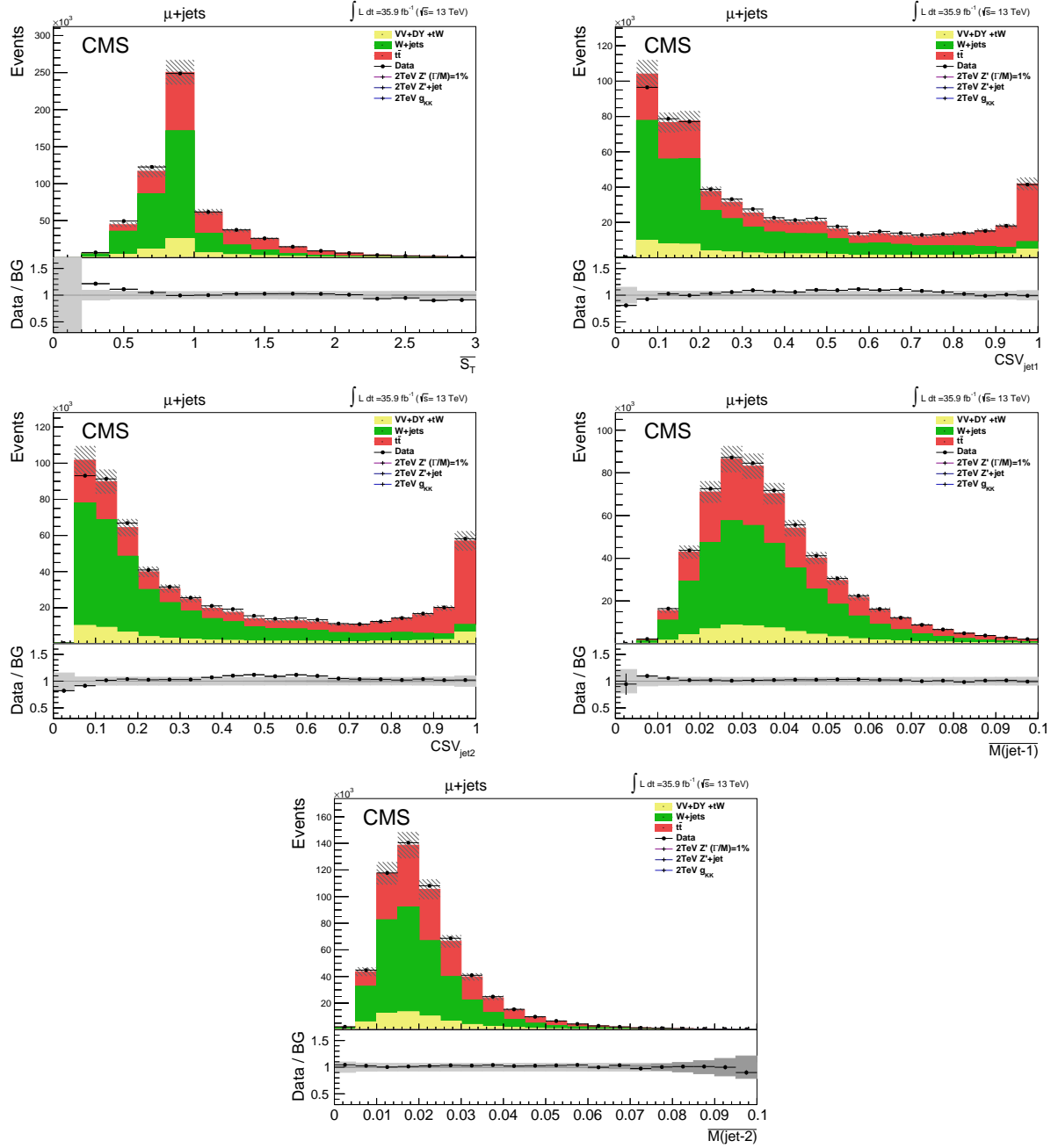


Figure 7.9: Data/MC comparison for the variables used in the BDT. The variables denoted with a bar are normalized by the mass of the reconstructed $t\bar{t}$ system. The yields of the background processes are normalized to data using scale factors described in 8.2 and the signal MC samples are normalized to a cross section of 1 pb. The shaded band represents the MC statistical uncertainty and the uncertainty on the SM cross section.

Variable	K-S statistic	p-value
$\overline{S_{33}}$	0.075	0.6093
$\overline{\Delta R \times p_T}$	0.070	0.6959
CSV-jet1	0.115	0.1267
CSV-jet2	0.105	0.1622
No.Jets	0.166	0.9913
$\overline{M(j_1)}$	0.065	0.7787
$\overline{M(j_2)}$	0.035	0.9996
$\overline{S_T}$	0.040	0.9966
$\min \Delta R$	0.070	0.6959
$\overline{p_{T,rel}}$	0.085	0.4485

Table 7.1: K-S test scores and p-values for the 10 variables used in the BDT for W+jets suppression.

respectively. As shown later, this analysis uses the BDT-T working point because it can successfully mitigate W+jets while enhancing the sensitivity of the analysis.

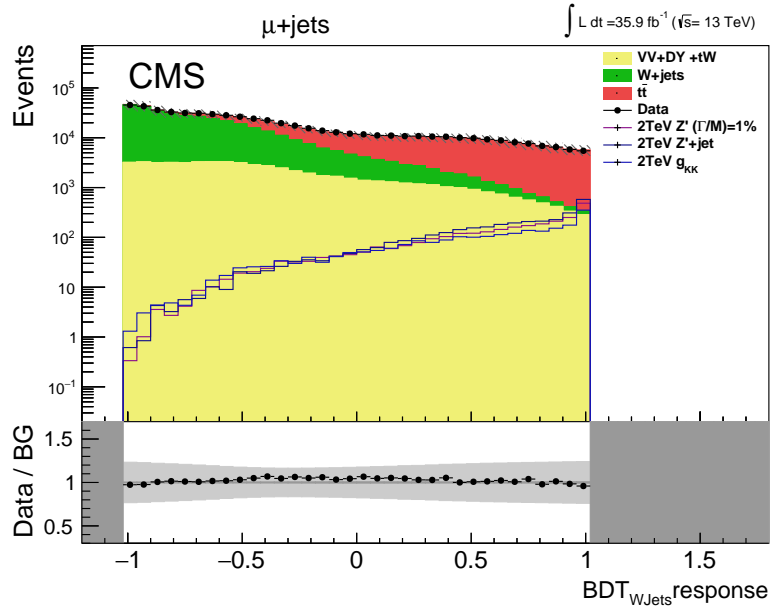


Figure 7.10: Data/MC comparison of the BDT response. The yields of the background processes are normalized to data using scale factors described in 8.2 and the signal MC samples are normalized to a cross section of 1 pb. The shaded band represents the MC statistical uncertainty and the uncertainty on the SM cross section.

8. EVENT RECONSTRUCTION AND FINAL BACKGROUND ESTIMATION

The invariant mass of the reconstructed $t\bar{t}$ system ($M_{t\bar{t}}$) is the observable used to search for the resonances described in previous chapters. In this chapter, we present its kinematical reconstruction using a χ^2 approach. Next, we define different regions used for the final background estimation based on two discriminators: the response of the BDT and the χ^2 of the reconstruction of the $t\bar{t}$ system. Finally, the sources of uncertainty that affect this analysis are introduced.

8.1 Kinematic Reconstruction of the $t\bar{t}$ System

The $t\bar{t}$ system is reconstructed by assigning the four-vectors of the reconstructed final-state objects (charged leptons, jets and p_T^{miss}) to the leptonic (t_ℓ) and hadronic (t_h) legs of the decay.

The charged lepton and p_T^{miss} are assigned to the leptonically decaying top-quark. p_T^{miss} is interpreted as the transverse component of the momentum of the neutrino. Assuming that the W boson was produced on-shell, a quadratic equation of the z -component of the momentum of neutrino can be derived (Appendix A):

$$p_z^\pm(\nu) = \frac{p_z(\ell)\zeta}{p_T^2(\ell)} \pm \sqrt{\frac{\zeta^2 p_z^2(\ell)}{p_T^4(\ell)} - \frac{E^2(\ell)p_T^2(\nu) - \zeta^2}{p_T^2(\ell)}}, \quad (8.1)$$

where $p(\ell)$ and $p(\nu)$ are the four momenta of the charged lepton and neutrino, respectively, while $\zeta = \frac{M_W^2}{2} + p_T(\ell)p_T(\nu)\cos\Delta\phi(\nu, \ell)$. This equation can have 0, 1 or 3 real solutions. In the absence of a real solution, the real part of the complex solution is used. If there are two real solutions then both cases are tested.

The next step is to assign the jets to one leg. For events where an AK8 jet passes the top-tagging selection, this jet is assigned to the hadronic side and the remaining AK4 jets with $\Delta R > 1.2$ from the top-tagged jet are listed as candidates for the leptonic leg. If no top-tagged jet is found, the available AK4 jets can be assigned to either leg of the decay.

A list of all possible combinations of the objects to reconstruct the $t\bar{t}$ system is made. Given the number of obtained solutions of the neutrino's momentum, $N_{\nu sol}$ and the number of jets found in the event, N_{jets} , it is easy to see that this list contains $N_{\nu sol} \times N_{jets} \times 2^{N_{jets}-1}$ possible choices. Once the four-momenta of t_ℓ and t_h are obtained, only one of the possible combinations is selected. The criteria used to choose the best combination is based on the idea that the reconstructed mass of t_ℓ and t_h , denoted by $m_{t_\ell}^{reco}$ and $m_{t_h}^{reco}$, respectively, should be close to the true top-quark mass. The goodness of fit test, known as χ^2 , is the criterion employed:

$$\chi_{t\bar{t}}^2 = \left(\frac{m_{t_\ell}^{reco} - m_{t_\ell}^{true}}{\sigma_{m_{t_\ell}}} \right)^2 + \left(\frac{m_{t_h}^{reco} - m_{t_h}^{true}}{\sigma_{m_{t_h}}} \right)^2 = \chi_\ell^2 + \chi_h^2, \quad (8.2)$$

and the combination of objects whose $\chi_{t\bar{t}}^2$ is the smallest is the selected one of the event. The parameters $m_{t_\ell}^{true} = 175$ GeV, $m_{t_h}^{true} = 177$ GeV, $\sigma_{m_{t_\ell}} = 19$ GeV and $\sigma_{m_{t_h}} = 16$ GeV are values derived from MC events where a $t\bar{t}$ pair is simulated and passes the same kinematic selection described above. In these events, we find the correct reconstruction hypothesis using a matching (based on the angular separation) between the reconstructed objects of the hypothesis and the corresponding particles at generator level from the $t\bar{t}$ decay. In events without a top-tagged jet, each AK4 jet associated to the hadronic decay is required to have $\Delta R < 0.4$ with respect to a given generated quark coming from the top decay; each of these generated quarks is required to be matched to an AK4 jet and more than one quark is allowed to be matched to the same jet. If the event contains a top-tagged jet, each of the quarks from the hadronic decay are required to have $\Delta R < 0.8$ with respect to the AK8 top-tagged jet. On the other hand, for the leptonic top, the AK4 jet

is required to have $\Delta R < 0.4$ with respect to the b quark from the generated leptonic top; the ΔR distance between reconstructed and generated lepton must be smaller than 0.1 and the distance between the generated neutrino and the missing transverse energy must be less than 0.3. If more than one hypothesis passes all of the above requirements, the one that has the smallest $\sum \Delta R$ between generated and reconstructed objects is chosen. The m_{t_ℓ} and m_{t_h} distributions for the correct $t\bar{t}$ hypothesis are fitted with a gaussian function. The mean value of the fitted distributions corresponds to $m_{t_{\ell,h}}^{true}$ and the width to $\sigma_{m_{t_{\ell,h}}}$.

Fig. 8.1 shows the $\chi_{t\bar{t}}^2$ distribution of events after the baseline selection.

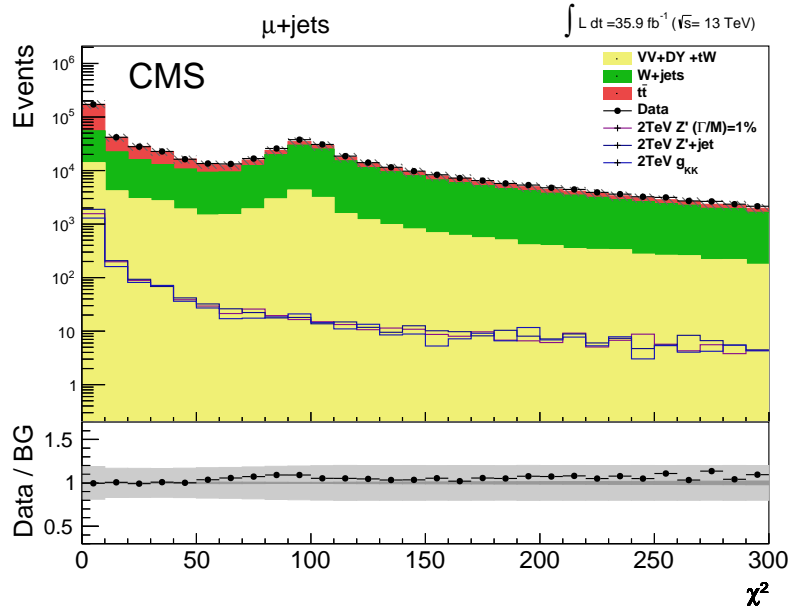


Figure 8.1: Data/MC comparison of the $\chi_{t\bar{t}}^2$ distribution after the baseline selection. The shoulder around 100 is due to events with a failed reconstructed W . The yields of the background processes are normalized to data using scale factors described in 8.2 and the signal MC samples are normalized to a cross section of 1 pb. The shaded band represents the MC statistical uncertainty and the uncertainty on the SM cross section.

Having reconstructed the $t\bar{t}$ system, we can use the invariant mass,

$$M_{t\bar{t}} = \sqrt{(E_t + E_{\bar{t}})^2 - (\vec{p}_t + \vec{p}_{\bar{t}})^2}, \quad (8.3)$$

spectrum to perform the search.

8.2 Final Event Selection and Categorization

The working point of the BDT for W +jets suppression along with the $\chi_{t\bar{t}}^2$ discriminator cut define the final kinematical region where the search is ultimately performed. They also allow to define the kinematic regions needed for the background estimation process described in the next section.

Using a $\chi_{t\bar{t}}^2 < 30$ cut significantly reduces contributions from all background sources, except from SM $t\bar{t}$, while improving the sensitivity of the analysis [26]. Furthermore, events can be separated into different categories based on the jet-tagging options. Also in [26], 3 categories were found to be the optimal choice; "1T" category, corresponded to events where a jet was top-tagged; "0T1B", corresponded to events where no top-tagged jets are found but at least one b -tagged jet was; "0T0B", corresponded to events where no b -tagged nor top-tagged jets were found. In this analysis, given that the BDT mitigates W +jets (the largest background in the 0T0B category) and uses the CSV score of the b -tagging algorithm, it is possible to have only two categories "1T" (events with one top-tagged jet) and "0T" (events without a top-tagged jet).

The next step is to optimize the BDT working point. To do so, we first take the number of expected background events B and the number of expected signal events S and look at the Figure of Merit (F.o.M),

$$F.o.M = S/\sqrt{S+B}, \quad (8.4)$$

for the different working points for the different signal samples. This can be summarized in Table 8.1. It can be seen that the BDT-T working point offers the best performance.

The choice of this BDT working point is even more evident based on expected limits (discussed in Chapter 8). Fig 8.2 shows the expected limits for different working points and categorizations. Also by obtaining the the expected limits, we cross-checked that with the BDT-T working point, the chosen $\chi_{t\bar{t}}^2 < 30$ threshold was still the optimal. As

Category	Sample	F.o.M (BDT-T)	F.o.M (BDT-M)	F.o.M (BDT-L)	F.o.M (No BDT)
0T	Z' [2 TeV] (1%)	12.30	10.21	7.90	6.55
1T	Z' [2 TeV] (1%)	36.27	34.39	31.91	30.60
0T	Z' [3 TeV] (1%)	7.03	5.30	4.01	3.31
1T	Z' [3 TeV] (1%)	20.69	18.27	16.44	15.68
0T	Z' [4 TeV] (1%)	8.65	6.41	4.75	3.92
1T	Z' [4 TeV] (1%)	22.55	19.79	17.75	16.91
0T	Z' [2 TeV] (10%)	5.86	5.09	3.92	3.28
1T	Z' [2 TeV] (10%)	17.07	16.15	14.65	13.85
0T	Z' [3 TeV] (10%)	12.43	10.15	7.58	6.31
1T	Z' [3 TeV] (10%)	32.20	29.53	26.71	25.54
0T	Z' [4 TeV] (10%)	6.41	5.13	3.85	3.19
1T	Z' [4 TeV] (10%)	16.71	14.67	13.08	12.44
0T	Z'+jet [2 TeV]	13.99	11.98	8.95	7.42
1T	Z'+jet [2 TeV]	40.91	39.50	36.16	34.69
0T	Z'+jet [3 TeV]	17.31	13.33	9.62	7.95
1T	Z'+jet [3 TeV]	44.66	40.52	36.73	35.22
0T	Z'+jet [4 TeV]	18.32	13.51	9.63	7.94
1T	Z'+jet [4 TeV]	42.46	38.06	34.29	32.83
0T	KK gluon [2 TeV]	4.71	4.26	3.31	2.77
1T	KK gluon [2 TeV]	14.49	13.57	12.39	11.80
0T	KK gluon [3 TeV]	5.36	4.41	3.36	2.80
1T	KK gluon [3 TeV]	14.10	13.04	11.79	11.21
0T	KK gluon [4 TeV]	4.71	4.01	3.09	2.57
1T	KK gluon [4 TeV]	12.4	11.64	10.42	9.94

Table 8.1: Figure of Merit values for the different working points of the BDT for each of the categories.

seen in Fig. 8.3, the expected limits remain rather stable at different $\chi_{t\bar{t}}^2$ thresholds, though at higher masses, $\chi_{t\bar{t}}^2 < 30$ proves to be in fact the optimal.

8.3 Sources of Uncertainty and Background Estimation

Uncertainties that arise from the nature of the measurement apparatus, assumptions made through the analysis and the models used to make inferences are called systematic. These sources of systematic uncertainty can impact the reconstructed $M_{t\bar{t}}$ distribution in two ways: in an overall uniform basis (normalization) or in a "per-range" basis (shape).

Moreover, we can group them in the following sets:

- **Physics Object Uncertainties:** They arise due to uncertainties on the experimental calibration.

* **Muon ID and HLT efficiencies:** We vary the muon ID $SF(p_T, \eta)$ and muon HLT $SF(p_T, \eta)$ by $\pm 1\sigma$.

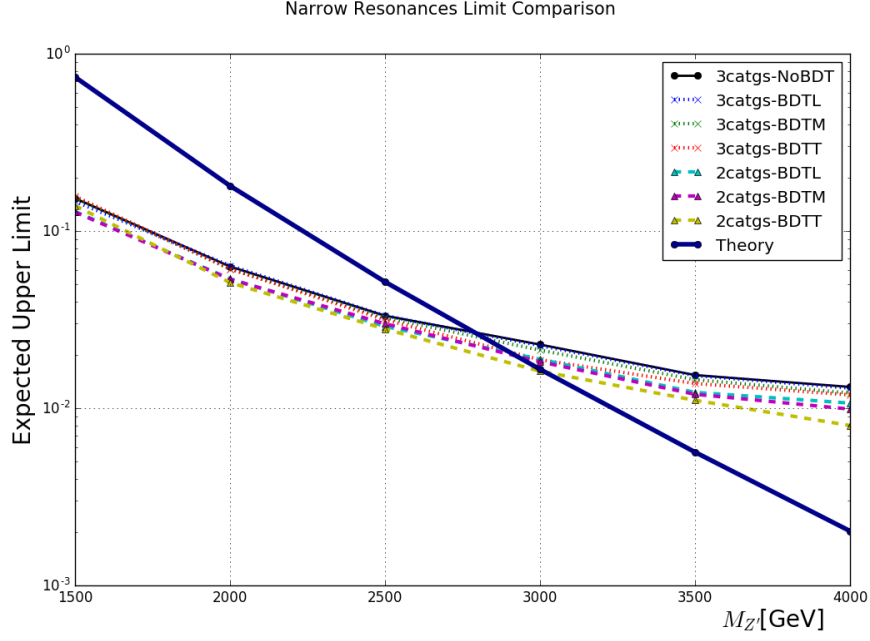


Figure 8.2: Comparison of the expected upper limits on the cross section times branching fraction for a narrow Z' for different BDT working points and categorization options.

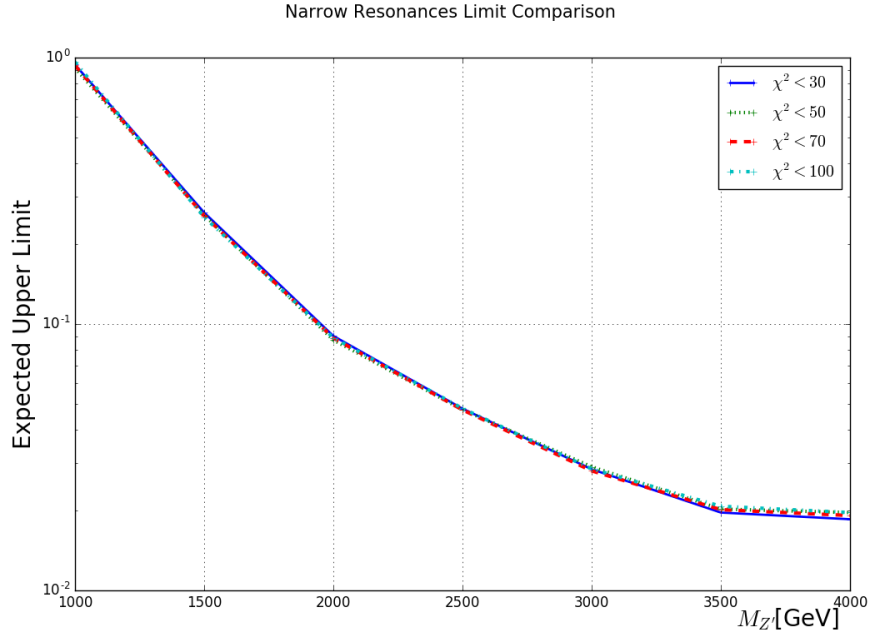


Figure 8.3: Comparison of the expected upper limits on the cross section times branching fraction for a narrow Z' for different χ^2_{tt} thresholds. The limits remain stable, but at higher masses a cut on 30 proves to be the optimal choice.

- * **Jet Energy Scale (JES) and Jet Energy Resolution (JER):** We vary the JES and JER by $\pm 1\sigma$ for AK4 and AK8 jets as a function of their p_T and η simultaneously. The variation is propagated to the p_T^{miss} .
- * **b -tagging:** For each jet flavor, the corresponding systematic uncertainty is obtained by applying a $\pm 1\sigma$ variation on the SF value of Eq. 6.6. The uncertainties of SF_b and SF_c are treated as fully correlated, whereas the uncertainty on SF_l (b -mistag rate) is treated as uncorrelated.
- * **top-tagging:** The systematic error associated to the top-tagging efficiency is left unconstrained during the fit. For the mis-identification efficiency the SF was obtained in Sec. 6.4.5 and the associated uncertainty is only statistical.
- **Beam Related Uncertainties:** There are two sources of uncertainty associated with the LHC beam performance
 - * **Integrated Luminosity:** The uncertainty on the total integrated luminosity recorded by CMS in the 2016 Run at $\sqrt{s} = 13$ TeV is 2.7%
 - * **Pileup Reweighting:** The systematic uncertainty associated to this correction is evaluated by varying the minimum bias cross section by 5%.
- **Theoretical Uncertainties:** The models used to generate the MC samples have their own limitations and assumptions
 - * **PDFs:** Simulated samples for the background processes are generated using PDFs from the NNPDF 3.0 set. The corresponding systematic uncertainty in the measurement is determined according to the procedure described in [83].
 - * **Q^2 -scale for $t\bar{t}$ and W +jets production:** The effect due to missing higher orders in the simulation of these SM backgrounds is estimated by varying the renormalization μ_R and factorization μ_F scales used in the simulation.
 - * **SM cross sections:** The systematic uncertainties on the normalization of the background processes are considered to be a conservative 25%. Their final val-

ues and uncertainties are determined from the background fit explained in the next chapter.

Table 8.2 summarizes all of the sources of systematic uncertainty that affect this analysis and Appendix C shows more details of their impact on the systematic variation on the $M_{t\bar{t}}$ distributions.

source of systematic uncertainty	uncertainty	type
$t\bar{t}$ cross section	8%	Normalization
W +jets cross section	6%	Normalization
Single top cross section	16%	Normalization
Z +jets cross section	15%	Normalization
Diboson cross section	6%	Normalization
Luminosity	2.6%	Normalization
PileUp reweighting	$\pm 1\sigma$	Normalization and Shape
Muon ID	$\pm 1\sigma$	Normalization and Shape
Muon trigger	$\pm 1\sigma$	Normalization and Shape
Jet Energy Scale	$\pm 1\sigma$	Normalization and Shape
Jet Energy Resolution	$\pm 1\sigma$	Normalization and Shape
b -tagging	$\pm 1\sigma$	Normalization and Shape
b -mistagging	$\pm 1\sigma$	Normalization and Shape
top-tagging	unconstrained	Normalization and Shape
top-mistagging	$\pm 20\%$	Normalization and Shape
Q^2 -scale ($t\bar{t}$, W +jets)	$\pm 1\sigma$	Normalization and Shape
PDFs	NNPDF 3.0	Normalization and Shape

Table 8.2: List of systematic uncertainties considered in the statistical analysis.

Different backgrounds contribute in a different extent to the total background yield based on the choice of $\chi_{t\bar{t}}^2$ and BDT working point. To provide a better handle to normalize the backgrounds, we create two regions:

- **“Blind” Signal Region (SR):** Events where the $M_{t\bar{t}} < 2 \text{ TeV}$, $\chi_{t\bar{t}}^2 < 30$, and passing the BDT-T working point.
- **“Blind” Control Region (CR):** Events where the $M_{t\bar{t}} < 2 \text{ TeV}$, $\chi_{t\bar{t}}^2 < 30$, and not passing the BDT-T working point. This region is kinematically similar to the signal region but is enriched with W +jets, DY, Single Top and Diboson events.

These regions are said to be “blinded” to masses where we expect to be sensitive to signal events ($M_{t\bar{t}} > 2 \text{ TeV}$), thus we only use the low-mass region of the distribution to

avoid picking up signal events in the fit. The final background estimates in this search are determined by fitting the background-only hypothesis to the data. This is done with a binned maximum-likelihood estimation (MLE) – described in the next chapter. For this fit we use the $M_{t\bar{t}}$ distributions in the CR and SR simultaneously. In the fitting procedure, three parameters are left unconstrained: the SM cross sections for $t\bar{t}$, W +jets, and the SF for the top-tagging efficiency. Leaving these parameters free to float in the fit allows to improve the flexibility of the background model and, also, it allows to determine their normalizations with a data-driven procedure. All the remaining systematic uncertainties, described above, are included in the fit as nuisance parameters. For each of these nuisance parameters, a log-normal distribution is used as prior constraint in the MLE.

Fig. 8.4 shows the results of the post-fit parameters in the CR, SR and when both were fit simultaneously. No post-fit parameter lies outside of 2σ of its prior uncertainty. Also, the results of fitting both CR and SR simultaneously are consistent with those obtained with each regions individually. By comparing the three cases, it is possible to see how different parameters are constrained by certain observables. As expected, the combined fit provides the best constraining power for each of the fit parameters, compared to the two sub-fits.

After the ML fit, the expected yields for SM backgrounds in the search region ($\chi^2_{t\bar{t}} < 30$, and BDT response ≥ 0.5) show good agreement to the observed data and no significant deviations from the SM predictions, as seen in Table 8.3 and Fig. 8.5.

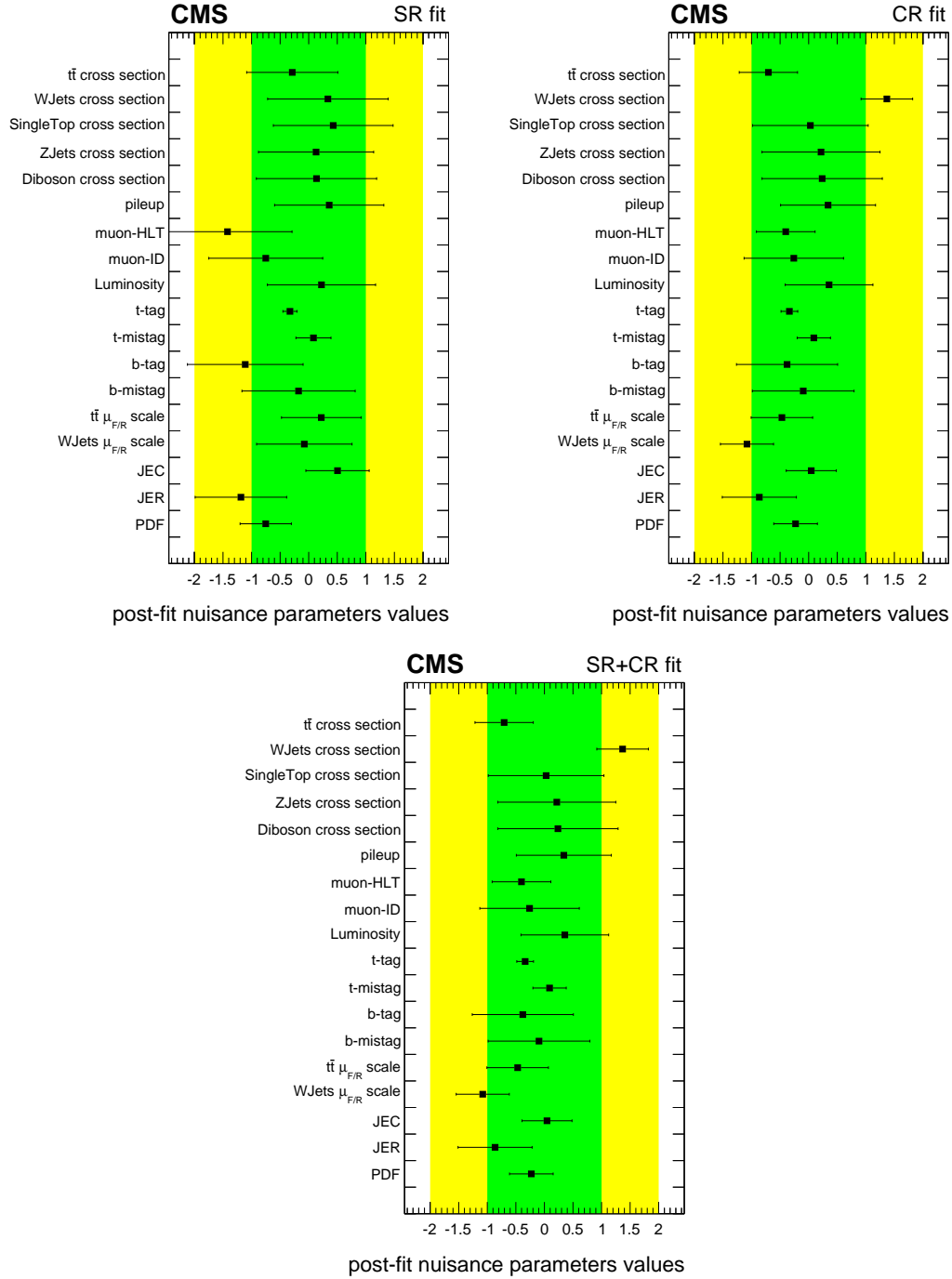


Figure 8.4: Post-fit values of the nuisance parameters of the background model. The fit parameters are expressed as deviations from their pre-fit values (zero), in units of the corresponding prior uncertainty. The 1 σ and 2 σ bands of each parameter are shown. On the top left the fit was done using only the SR. On the top right the fit was done using only the CR. On the bottom, both CR and SR were used.

Process	0T	1T
$t\bar{t}$	35036 ± 2808	1119 ± 99
W +jets	1008 ± 105	30 ± 4
$DY + ST + VV$	2324 ± 349	32 ± 6
Total Background	38368 ± 2831	1181 ± 99
DATA	38346	1187
$Z'(M_{Z'} = 1.0 \text{ TeV}, w = 1\%)$	535	13
$Z'(M_{Z'} = 2.0 \text{ TeV}, w = 1\%)$	866	625
$Z'(M_{Z'} = 3.0 \text{ TeV}, w = 1\%)$	1089	708
$Z'(M_{Z'} = 4.0 \text{ TeV}, w = 1\%)$	1049	648
$Z'(M_{Z'} = 5.0 \text{ TeV}, w = 1\%)$	1096	516
$Z'(M_{Z'} = 1.0 \text{ TeV}, w = 10\%)$	488	31
$Z'(M_{Z'} = 2.0 \text{ TeV}, w = 10\%)$	798	503
$Z'(M_{Z'} = 3.0 \text{ TeV}, w = 10\%)$	944	573
$Z'(M_{Z'} = 4.0 \text{ TeV}, w = 10\%)$	883	499
$Z'(M_{Z'} = 5.0 \text{ TeV}, w = 10\%)$	753	378
$Z'(M_{Z'} = 1.0 \text{ TeV}, w = 30\%)$	450	56
$Z'(M_{Z'} = 2.0 \text{ TeV}, w = 30\%)$	706	426
$Z'(M_{Z'} = 3.0 \text{ TeV}, w = 30\%)$	755	442
$Z'(M_{Z'} = 4.0 \text{ TeV}, w = 30\%)$	693	385
$Z'(M_{Z'} = 5.0 \text{ TeV}, w = 30\%)$	657	337
$Z'+\text{jet}(M_{Z'} = 1.0 \text{ TeV}, w = 1\%)$	742	44
$Z'+\text{jet}(M_{Z'} = 2.0 \text{ TeV}, w = 1\%)$	1030	746
$Z'+\text{jet}(M_{Z'} = 3.0 \text{ TeV}, w = 1\%)$	1260	812
$Z'+\text{jet}(M_{Z'} = 4.0 \text{ TeV}, w = 1\%)$	1332	748
$g_{KK}(M_{g_{KK}} = 1.0 \text{ TeV}, w = 1\%)$	446	29
$g_{KK}(M_{g_{KK}} = 2.0 \text{ TeV}, w = 1\%)$	663	426
$g_{KK}(M_{g_{KK}} = 3.0 \text{ TeV}, w = 1\%)$	763	429
$g_{KK}(M_{g_{KK}} = 4.0 \text{ TeV}, w = 1\%)$	678	368
$g_{KK}(M_{g_{KK}} = 5.0 \text{ TeV}, w = 1\%)$	632	327

Table 8.3: Number of expected background events compared to the observed events in each category. The expected yields have been obtained after the MLE. The reported uncertainties on each background both the statistical error and the posterior uncertainties.

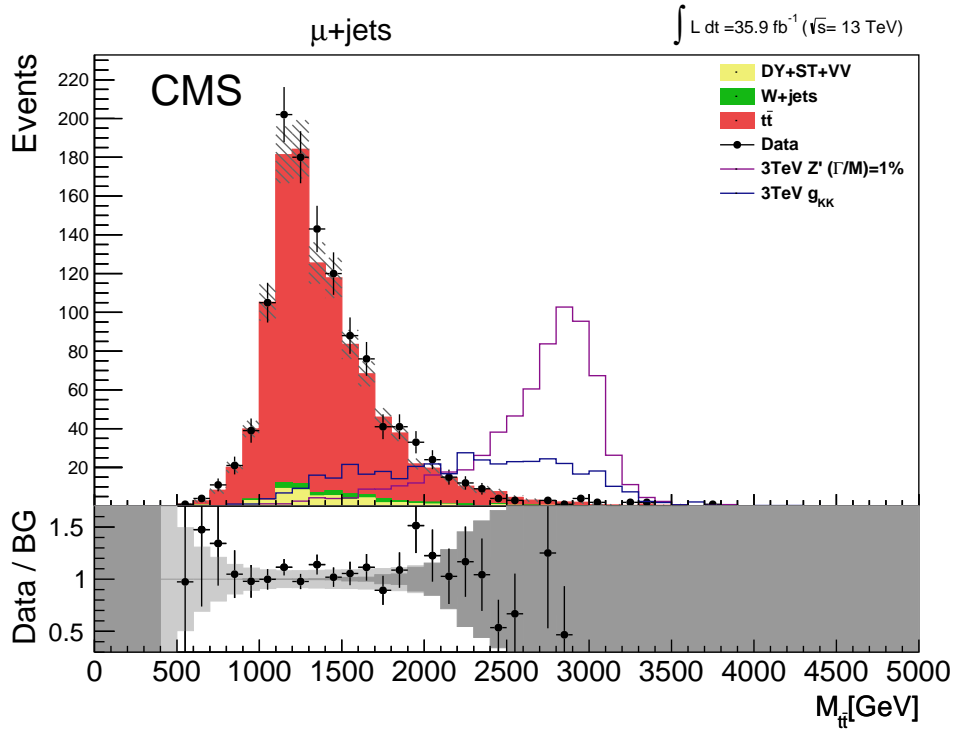
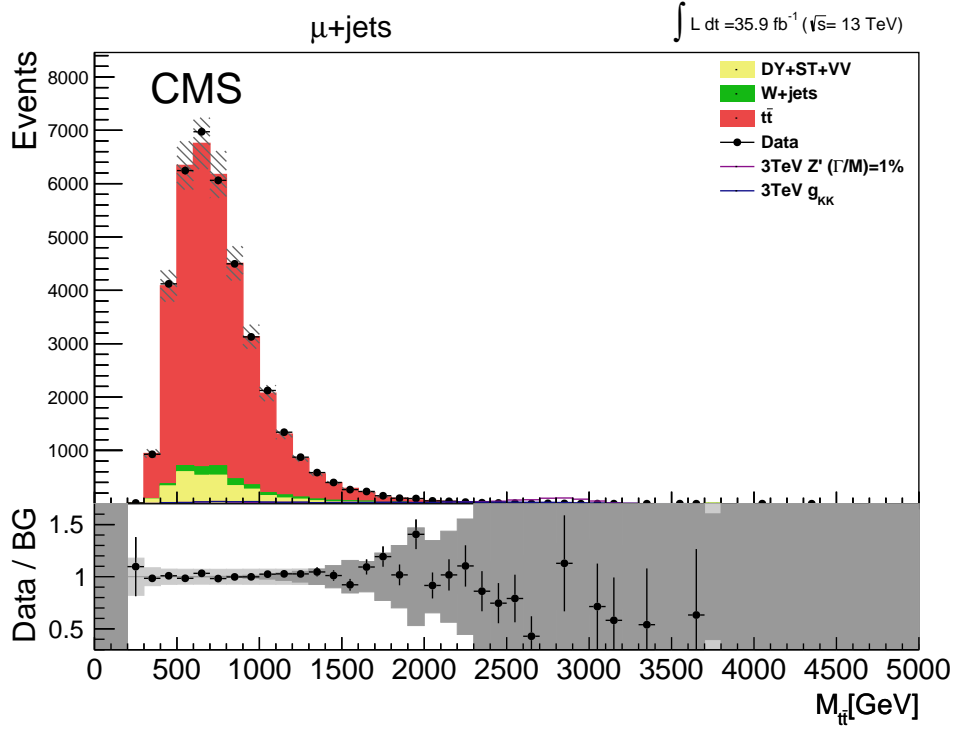


Figure 8.5: Data/MC comparison of the $M_{t\bar{t}}$ distributions for the 0T (top) and 1T (bottom) categories. The events pass the BDT-T working point and $\chi^2_{t\bar{t}} < 30$. The yields of the background processes are normalized to data using scale factors obtained by the MLE and the signal MC samples are normalized to a cross section of 1 pb. The shaded band represents the MC statistical uncertainty and the uncertainty on the SM cross section.

9. STATISTICAL ANALYSIS

A key task in particle physics is to be able to discriminate between two or more hypotheses based on the experimental data. In this case we want to determine whether the sample of events is composed of background only, which we can identify to the null hypothesis H_0 , or rather of a mixture of background plus signal events which we can identify as the alternative hypothesis H_1 . A test statistic allows to quantify the agreement of the observed data to either of the hypotheses.

In this chapter the statistical modeling employed as well as the test statistics chosen and the determination of the confidence levels is described.

9.1 Bayesian Probability and Likelihoods

A Bayesian approach allows to define in a quantitative way the probabilities associated to the knowledge of unknown parameters, allowing to assign a probability to the possibility that a given parameter lies within a certain interval. The mathematical tools needed to achieve such goal start from Bayes' theorem

Bayes' Theorem

Bayes' Theorem states that

$$P(A|B) = \frac{P(B|A)P(A)}{P(B)}, \quad (9.1)$$

where the probability $P(A)$ is the probability of event A before the knowledge that B has happened and it is called the prior and $P(A|B)$ is the same probability of the same event A having the information that B occurred and it is called the posterior.

Likelihood

The likelihood function $\mathcal{L}(\vec{x}|\vec{\theta})$ is defined as the probability density at a certain point $\vec{x} = (x_1, \dots, x_n)$ that depends on a set of parameters $\vec{\theta} = (\theta_1, \dots, \theta_m)$. It follows from Eq. 9.1 that we can define the posterior Bayesian probability distribution function of $\vec{\theta}$, given the observation \vec{x} to be

$$P(\vec{\theta}|\vec{x}) = \frac{\mathcal{L}(\vec{x}|\vec{\theta})\pi(\vec{\theta})}{\int \mathcal{L}(\vec{x}|\vec{\theta})\pi(\vec{\theta})d\vec{\theta}}, \quad (9.2)$$

where $\pi(\vec{\theta})$ is the prior of the parameters $\vec{\theta}$ and represents our degree of belief about those parameters before the observation of \vec{x} .

Furthermore, if we have N repeated measurements $\vec{x}_1, \dots, \vec{x}_N$, we can consider the likelihood corresponding to the total samples, assuming they are independent of each other, as the product of the individual likelihoods

$$\mathcal{L}(\vec{x}_1, \dots, \vec{x}_N|\vec{\theta}) = \prod_{i=1}^N \mathcal{L}(\vec{x}_i|\vec{\theta}). \quad (9.3)$$

9.2 Statistical Modeling

The observable employed to test hypotheses and set upper limits is the $M_{t\bar{t}}$ distribution, which is given in a set of histograms corresponding to the 2 different tagged categories. The number of entries in each bin of each histogram obeys a Poisson distribution whose expected number of entries in each bin can be determined by the theoretical predictions and also depends on the unknown parameter we ultimately would like to estimate. Hence, using Eq. 9.3, in this case the likelihood function that characterizes the set

of experimental observables is given by

$$\mathcal{L}(\vec{x}_1, \dots, \vec{x}_N | \vec{\theta}) = \prod_{i=1}^N \frac{e^{-r_i} r_i^{n_i}}{n_i!}, \quad (9.4)$$

where $r_i = r_i(\vec{\theta})$ represents the expected rate in the i -th bin. Given the expected backgrounds, we can describe the rate as

$$r_i(\vec{\theta}) = \sum_k \lambda_{k,i}(\vec{\theta}) t_{k,i}, \quad (9.5)$$

where $t_{k,i}$ corresponds to the rate of entries produced by the k -th physics process or template in the i -th bin and the coefficient $\lambda_{k,i}$ scales the overall normalization of the k -th template. In the instance where the rate can be considered to come from background plus signal processes, it can be rewritten as

$$r_i(\mu, \vec{\theta}) = \mu s_i + \sum_k \lambda_{k,i}(\vec{\theta}) t_{k,i}, \quad (9.6)$$

where s_i is the signal rate and μ is the normalization often called signal strength. The set of parameters, $\vec{\theta}$, are called nuisance parameters and they can be assigned to the systematic uncertainties that affect the rates and shapes of the templates. For most cases the nuisance parameters follow a normal distribution $\theta_l \sim \mathcal{N}(0, 1)$, however the rates are modified by the functional form $\lambda(\vec{\theta})$, Eq. 9.7. Given the template-based approach, where each of the templates is accompanied by its corresponding shifted template t_k^\pm due to the $\pm 1\sigma$ variation of each systematic uncertainty, we use a quadratically matched asymmetric log-normal description for the scale coefficients,

$$\lambda_{k,i}(\theta_l) = \exp \left[\frac{1}{2} (\sigma_{k,i,l}^+ + \sigma_{k,i,l}^-) \theta_l + \frac{1}{2} (\sigma_{k,i,l}^+ - \sigma_{k,i,l}^-) \theta_l^2 \right], \quad (9.7)$$

and the parameters,

$$\sigma^{\pm}_{k,i,l} = \pm \ln(t^{\pm}_{k,i,l}/t_{k,i}), \quad (9.8)$$

are derived from the log-ratio of the shifted and nominal templates for each uncertainty l .

Given the limited size of the MC samples that estimate the background and signal rates, the Barlow-Beeston [84], [85] lite method is employed. This method allows to account for an additional statistical uncertainty by adding one additional nuisance parameter for each bin, ν_i , that follows a normal distribution. Adding all these extra parameters makes the following computations hard and unstable, thus the likelihood has to be first evaluated at the maximum-likelihood point,

$$\mathcal{L}_{\mathcal{P}}(\vec{x}|\mu, \vec{\theta}) = \sup_{\vec{\nu}}[\mathcal{L}(\vec{x}|\mu, \vec{\theta}, \vec{\nu})], \quad (9.9)$$

this maximized likelihood functions sometimes receives the name of "profile"-likelihood, hence the sub-index \mathcal{P} .

9.2.1 Test Statistic

Statistical tests are used to choose between the two competing hypotheses H_0 and H_1 . Given the statistical modeling described above, the test statistic used in this work is based on the log-likelihood ratio,

$$t = 2 \ln \frac{\mathcal{L}_{\mathcal{P}}(\vec{x}|\mu \neq 0, \vec{\theta})}{\mathcal{L}_{\mathcal{P}}(\vec{x}|\mu = 0, \vec{\theta})}, \quad (9.10)$$

where the numerator represents the alternative hypothesis H_1 ($\mu \neq 0$), whereas the denominator corresponds to H_0 ($\mu = 0$). This test expresses how many times more likely the data are under one model than the other. This likelihood ratio test can then be used to compute a p -value.

9.2.2 Limit Setting

In the case when no convincing new signal is observed, it is interesting to quote as result of the search for the new phenomena the upper limit on the expected yield of the hypothetical new signal. Upper limits are set requiring that the p -value < 0.05 , corresponding to a 95% confidence level (CL). In this Bayesian approach, the first step is to marginalize those nuisance parameters of the posterior probability of Eq. 9.2,

$$P(\mu|\vec{x}) = \int_{\vec{\theta}} d\vec{\theta} \mathcal{L}_{\mathcal{P}}(\vec{x}|\mu, \vec{\theta}) \pi(\mu, \vec{\theta}), \quad (9.11)$$

where the prior distributions associated to the signal strength and nuisance parameters are assumed to be Gaussian distributions centered in zero and with unit variance. Then, the upper limit of the signal strength μ^{up} can be computed requiring that the marginal posterior probability corresponding to the interval $[0, \mu^{up}[$ is equal to CL,

$$0.95 = \int_0^{\mu^{up}} d\mu P(\mu|\vec{x}). \quad (9.12)$$

9.3 Computation

The previously described statistical model can be evaluated using the `theta` framework [86], which allows a template-based statistical modeling and inference that focuses on problems in high-energy physics.

To make the numerical computation more stable in the regions where the expected rates are low, the templates are rebinned such that the statistical uncertainty from the sum of the background templates in each bin is less than 30%. The marginalization of Eq. 9.11 is done numerically using a Markov Chain Monte-Carlo method.

To compute the expected upper limits, several toy-models are generated without signal. In each of these models, random numbers for $\vec{\theta}$ are generated following a normal distribution. These values are used to generate a set of possible choices of μ . The next

step is to use this generated value of μ to estimate the number of counts n per bin using the Poisson distribution: $n = \text{Pois}(\mu)$. The expected limit is determined by the mean upper limit in these toy experiments. Additionally, the median central 68% and 95% of the upper limits for the toy models define the $\pm 1\sigma$ and $\pm 2\sigma$ bands around the expected limit.

10. RESULTS

Given that the expected background agrees within its uncertainty with the analyzed data, we use Eq. 9.12 to derive the 95% CL upper limits on the cross section times branching ratio for the various benchmark models of heavy resonances mentioned before.

We use the $M_{t\bar{t}}$ spectrum in the two categories 1T and 0T as the input templates of the statistical model mentioned in the previous chapter.

The extracted limits are obtained as a function of the resonance mass. Tables 10.1-10.5 show the expected and observed 95% CL limits on the production cross section times branching ratio of the five models considered in this analysis as a function of their mass. These limits are shown in Figs. 10.1-10.5. In these plots the red dashed line indicates the theoretical cross section, the light blue dashed line indicates the expected limit, the one (and two) σ deviations from the expected limit are shown as the two light (dark) bands around it, and the observed limit is represented by the continuous black line.

Moreover, we exclude a mass range for a particular resonance when the predicted cross section is higher than the excluded limit. These mass limits for the five models are shown in Table 10.6.

Limits for the Z' model ($w = 1\%$)

$M_{Z'}$ (TeV)	Expected (pb)	Exp. $\pm 1\sigma$ (pb)	Exp. $\pm 2\sigma$ (pb)	Observed (pb)
0.50	199	95.8 – 527	56.9 – 1070	513
1.00	0.748	0.535 – 1.05	0.4 – 1.43	0.397
1.50	0.172	0.121 – 0.242	0.0903 – 0.338	0.139
2.00	0.0608	0.0425 – 0.0864	0.031 – 0.117	0.117
2.50	0.0287	0.0202 – 0.0417	0.015 – 0.0588	0.0225
3.00	0.0169	0.0116 – 0.0257	0.00867 – 0.035	0.0139
3.50	0.0117	0.0081 – 0.0169	0.00603 – 0.0238	0.0122
4.00	0.0093	0.0065 – 0.0133	0.00477 – 0.0188	0.00968
4.50	0.0083	0.0058 – 0.0118	0.00438 – 0.0166	0.00887
5.00	0.0095	0.0067 – 0.0143	0.00474 – 0.0196	0.0101

Table 10.1: Expected and observed 95% CL lower mass limits for the Z' model with 1% relative widths .

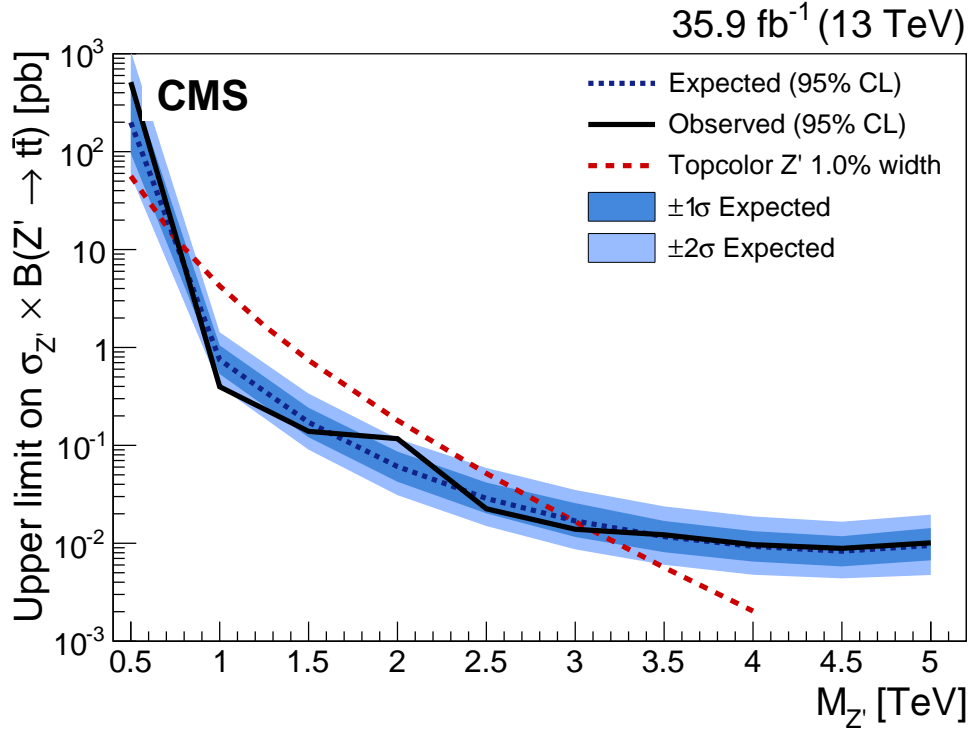


Figure 10.1: Expected and observed 95% CL limits on the production cross section times branching ratio of the narrow Z' model.

Limits for the Z' model ($w = 10\%$)

$M_{Z'}$ (TeV)	Expected (pb)	Exp. $\pm 1\sigma$ (pb)	Exp. $\pm 2\sigma$ (pb)	Observed (pb)
0.50	88.1	49.3 – 173	32.2 – 373	140
1.00	1.06	0.75 – 1.50	0.56 – 2.00	0.58
1.50	0.266	0.186 – 0.382	0.133 – 0.516	0.227
2.00	0.105	0.072 – 0.152	0.051 – 0.200	0.196
2.50	0.052	0.037 – 0.078	0.027 – 0.105	0.038
3.00	0.030	0.021 – 0.044	0.015 – 0.061	0.023
3.50	0.024	0.016 – 0.036	0.012 – 0.048	0.023
4.00	0.021	0.015 – 0.032	0.011 – 0.045	0.020
4.50	0.024	0.016 – 0.035	0.013 – 0.049	0.022
5.00	0.032	0.022 – 0.047	0.016 – 0.069	0.032

Table 10.2: Expected and observed 95% CL lower mass limits for the Z' model with 10% relative widths .

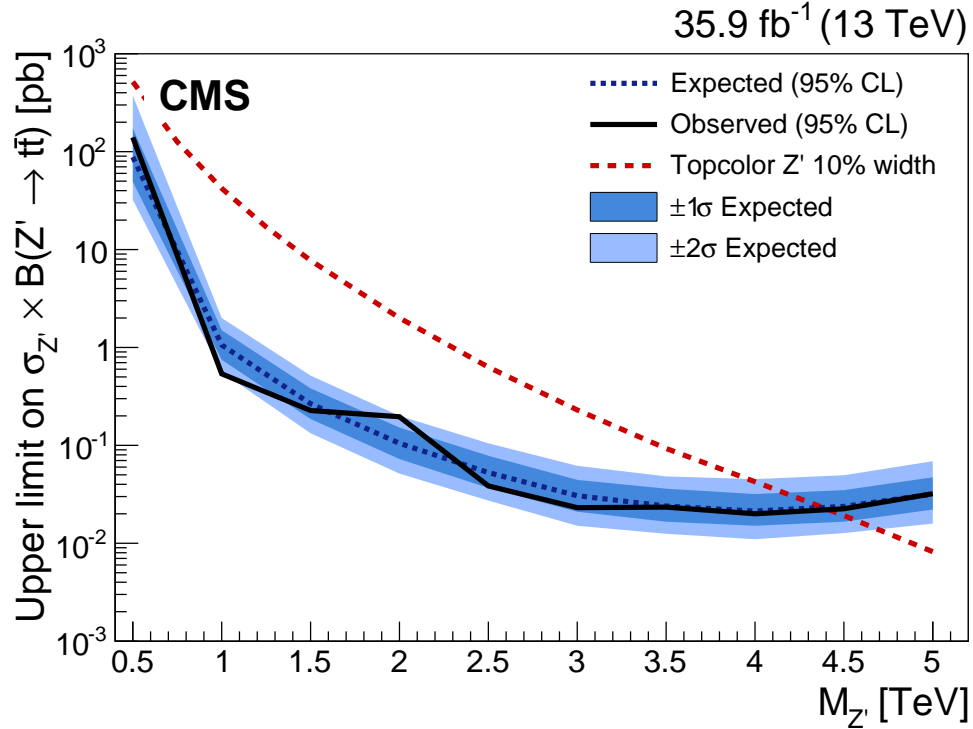


Figure 10.2: Expected and observed 95% CL limits on the production cross section times branching ratio of the wide Z' model.

Limits for the Z' model ($w = 30\%$)

$M_{Z'}$ (TeV)	Expected (pb)	Exp. $\pm 1\sigma$ (pb)	Exp. $\pm 2\sigma$ (pb)	Observed (pb)
1.00	1.420	0.970 – 2.090	0.717 – 2.96	0.815
2.00	0.154	0.106 – 0.216	0.078 – 0.30	0.282
3.00	0.062	0.043 – 0.093	0.031 – 0.13	0.052
4.00	0.050	0.035 – 0.071	0.026 – 0.10	0.055
5.00	0.057	0.041 – 0.084	0.029 – 0.12	0.068

Table 10.3: Expected and observed 95% CL lower mass limits for the Z' model with 30% relative widths .

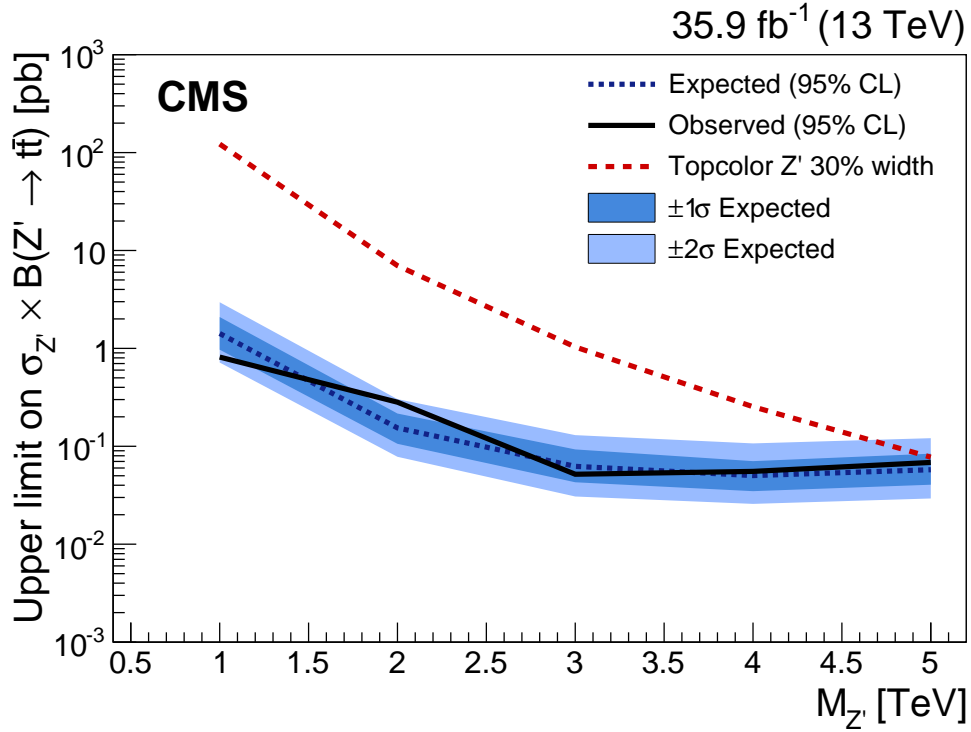


Figure 10.3: Expected and observed 95% CL limits on the production cross section times branching ratio of the extra-wide Z' model.

Limits for the Z' +jet model

$M_{Z'}$ (TeV)	Expected (pb)	Exp. $\pm 1\sigma$ (pb)	Exp. $\pm 2\sigma$ (pb)	Observed (pb)
0.5	36.5	21.5 – 67	13.3 – 162	55.6
1.0	0.834	0.600 – 1.2	0.455 – 1.72	0.48
1.5	0.208	0.146 – 0.297	0.101 – 0.392	0.152
2.0	0.075	0.053 – 0.108	0.037 – 0.146	0.128
2.5	0.040	0.026 – 0.056	0.018 – 0.079	0.027
3.0	0.023	0.016 – 0.034	0.012 – 0.048	0.02
3.5	0.019	0.012 – 0.027	0.008 – 0.037	0.013
4.0	0.015	0.011 – 0.023	0.007 – 0.031	0.011

Table 10.4: Expected and observed 95% CL lower mass limits for the Z' +jet model.

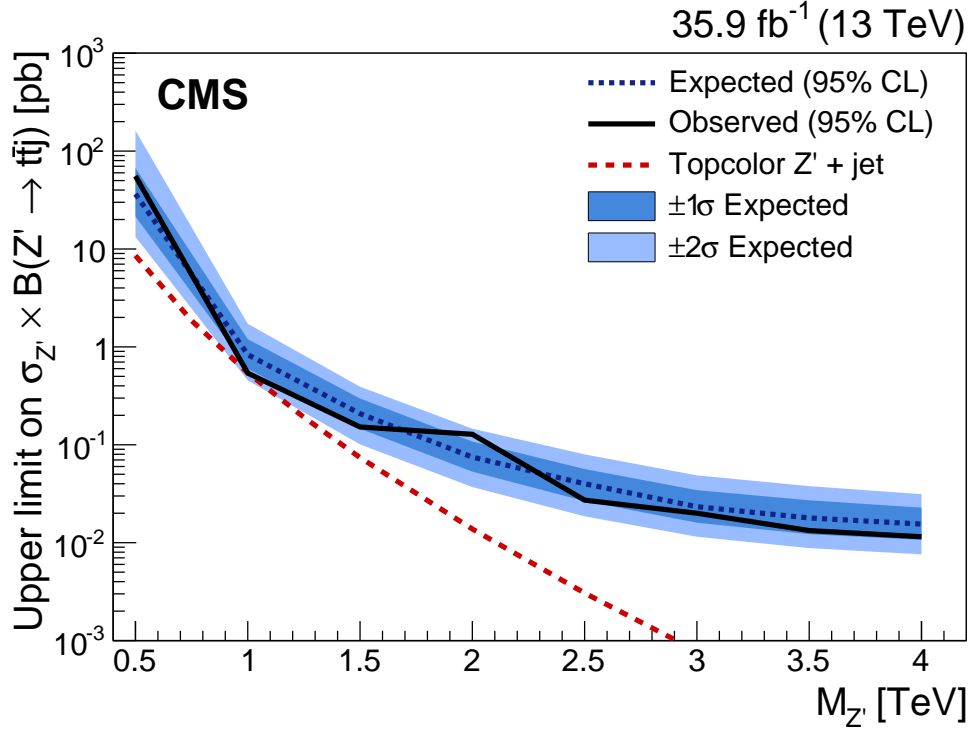


Figure 10.4: Expected and observed 95% CL limits on the production cross section times branching ratio of the Z' +jet model.

Limits for the KK gluon model

$M_{Z'}$ (TeV)	Expected (pb)	Exp. $\pm 1\sigma$ (pb)	Exp. $\pm 2\sigma$ (pb)	Observed (pb)
1.0	1.280	0.874 – 1.83	0.649 – 2.570	0.689
2.0	0.150	0.102 – 0.220	0.075 – 0.303	0.261
3.0	0.055	0.037 – 0.079	0.027 – 0.113	0.051
4.0	0.043	0.029 – 0.064	0.023 – 0.095	0.037
5.0	0.048	0.033 – 0.069	0.025 – 0.101	0.042

Table 10.5: Expected and observed 95% CL lower mass limits for the KK gluon model.

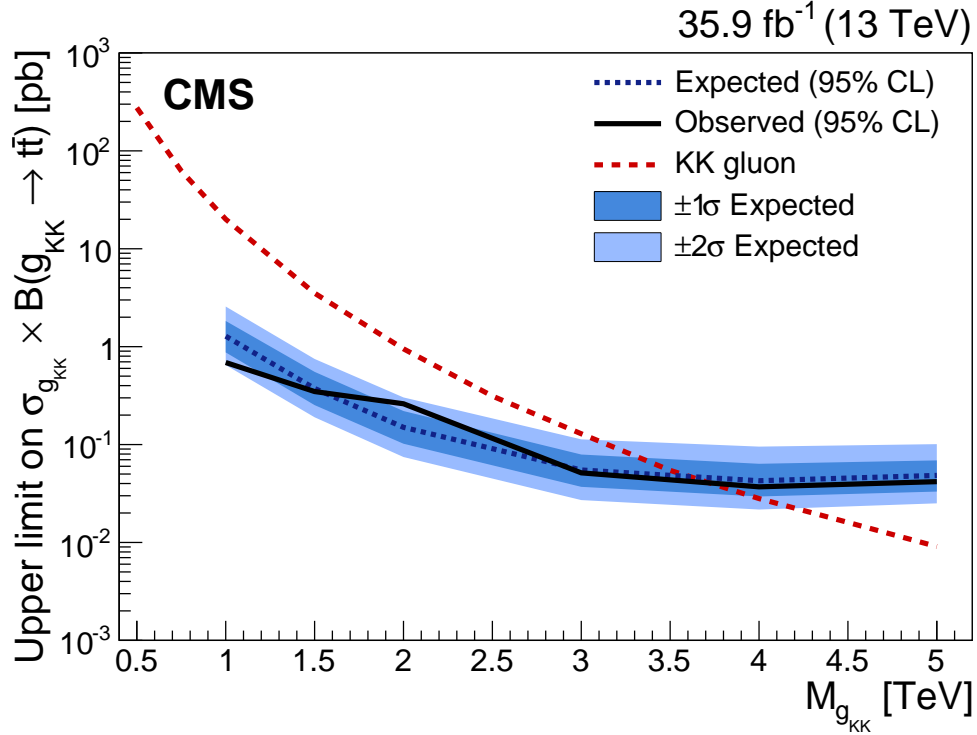


Figure 10.5: Expected and observed 95% CL limits on the production cross section times branching ratio of the KK gluon model.

Signal model	Observed Mass Limit [TeV]	Expected Mass Limit [TeV]
narrow Z' (1% width)	3.10	3.05
wide Z' (10% width)	4.45	4.40
extra-wide Z' (30% width)	5.00	5.00
KK gluon	3.75	3.70

Table 10.6: Expected and observed 95% CL upper mass limits for the three models studied in this analysis.

11. SUMMARY AND OUTLOOK

This thesis presents a search for heavy resonances decaying to $t\bar{t}$ in the muon+jets channel using 35.9 fb^{-1} of data recorded by the CMS experiment in 2016. The analysis was designed to have high sensitivity at resonance masses above 1 TeV, where final state objects can overlap because of the high Lorentz boost of the top quark decay products. The employment of a boosted decision tree to reduce non $t\bar{t}$ background along with the usage of the jet substructure variables to identify top-jets significantly improved the sensitivity of the analysis.

No evidence of these high-mass resonances was found in the $M_{t\bar{t}}$ spectrum. In particular, we searched for five signal models: a Z' boson with a 1%, 10% and 30% relative width, a Z' boson with a 1% relative width produced in association with a jet, and a Kaluza-Klein resonant gluon in a Randall-Sundrum model. Using a Bayesian statistical model, limits on their production cross section times branching fraction were set with a 95% CL. Furthermore, this thesis excludes 1% Z' resonances below 3.10 TeV, 10% Z' resonances below 4.45 TeV, 30% Z' resonances below 5 TeV, Kaluza-Klein gluons below 3.75 TeV, and finally no mass limit could be set for the 1% Z' resonance model produced in association with a jet. The obtained results present a significant limit improvement compared to the latest results by CMS [26] and ATLAS [27].

In the near future, the observed limits can be further improved by a couple hundred GeV when the results of the 2016 dataset on electron+jet channel and the hadronic channel are combined to this result. Finally, in 2017 the LHC is aiming to reach an integrated

luminosity of 45 fb^{-1} . If this new data is combined with the 2016 data, the sensitivity of this search would be further improved.

The next step, that has not been attempted before, would be to separate the irreducible SM $t\bar{t}$ background from the resonant signal. Given that the p_T of the resonant tops are expected to peak around half of the mass of the resonance, a suitably strong p_T cut has very small effect on the signal and would be quite effective in suppressing the SM $t\bar{t}$ background. Moreover, the angular distributions of the top jets could be exploited since a more significant contribution of SM $t\bar{t}$ would be located in the forward region of the detector.

A. RECONSTRUCTION OF THE NEUTRINO'S MOMENTUM

In order to reconstruct the leptonic leg of the $t\bar{t}$ system, t_ℓ , we need to determine the neutrino's momentum. In this analysis, we assume that the missing transverse momentum is completely associated to the neutrino. To determine the z -component of its momentum, we assume that its mother W boson was produced on shell. Thus, if p^μ represents the four momentum of a particle, by momentum conservation we have that

$$p^\mu(W) = p^\mu(\ell) + p^\mu(\nu_\ell) \quad (\text{A.1})$$

Taking its squared value

$$p^2(W) = p^\mu(\ell)p_\mu(\ell) + p^\mu(\nu_\ell)p_\mu(\nu_\ell) + p^\mu(\ell)p_\mu(\nu_\ell) + p^\mu(\nu_\ell)p_\mu(\ell) \quad (\text{A.2})$$

Simplifying in the rest frame of the W

$$M^2(W) = M^2(\ell) + M^2(\nu_\ell) + 2(E(\ell)E(\nu_\ell) - \vec{p}(\ell) \cdot \vec{p}(\nu_\ell)) \quad (\text{A.3})$$

With the negligible masses of the neutrino, we can write

$$E(\nu_\ell) = \sqrt{p_T^2(\nu_\ell) + p_z^2(\nu_\ell)} \quad (\text{A.4})$$

Thus, plugging B.4 into B.3, and also neglecting the lepton mass it follows that

$$\frac{M^2(W)}{2} = E(\ell)\sqrt{p_T^2(\nu_\ell) + p_z^2(\nu_\ell)} - (p_T(\ell)p_T(\nu_\ell)\cos(\Delta\phi(\nu_\ell, \ell)) + p_z(\ell)p_z(\nu_\ell)) \quad (\text{A.5})$$

Define

$$\zeta = \frac{M_W^2}{2} + p_T(\ell)p_T(\nu_\ell)\cos\Delta\phi(\nu_\ell, \ell) \quad (\text{A.6})$$

Using B.6 definition and rearranging B.5, we get

$$\zeta^2 + p_z^2(\ell)p_z^2(\nu_\ell) + 2\zeta p_z(\ell)p_z(\nu_\ell) = E^2(\ell)(p_T^2(\nu_\ell) + p_z^2(\nu_\ell)) \quad (\text{A.7})$$

Which is a quadratic equation that can be solved for $p_z(\nu_\ell)$

$$p_z^\pm(\nu_\ell) = \frac{p_z(\ell)\zeta}{p_T^2(\ell)} \pm \sqrt{\frac{\zeta^2 p_z^2(\ell)}{p_T^4(\ell)} - \frac{E^2(\ell)p_T^2(\nu_\ell) - \zeta^2}{p_T^2(\ell)}} \quad (\text{A.8})$$

B. KINEMATIC DISTRIBUTIONS

This appendix includes data/MC comparisons for several kinematic quantities relevant to the analysis. For each variable, the distributions are shown for the two categories, 1T and 0T. The plots are obtained after the baseline selection, $\chi^2_{tt} < 30$, $\text{BDT} < 0.5$ and after correcting the MC samples with the scale factors for normalization derived through the MLE.

In each plot, the error band associated to the total background expectation includes the MC statistical uncertainty and the post-fit uncertainties on the SM cross sections. The signal templates are normalized to a cross section of 1 pb.

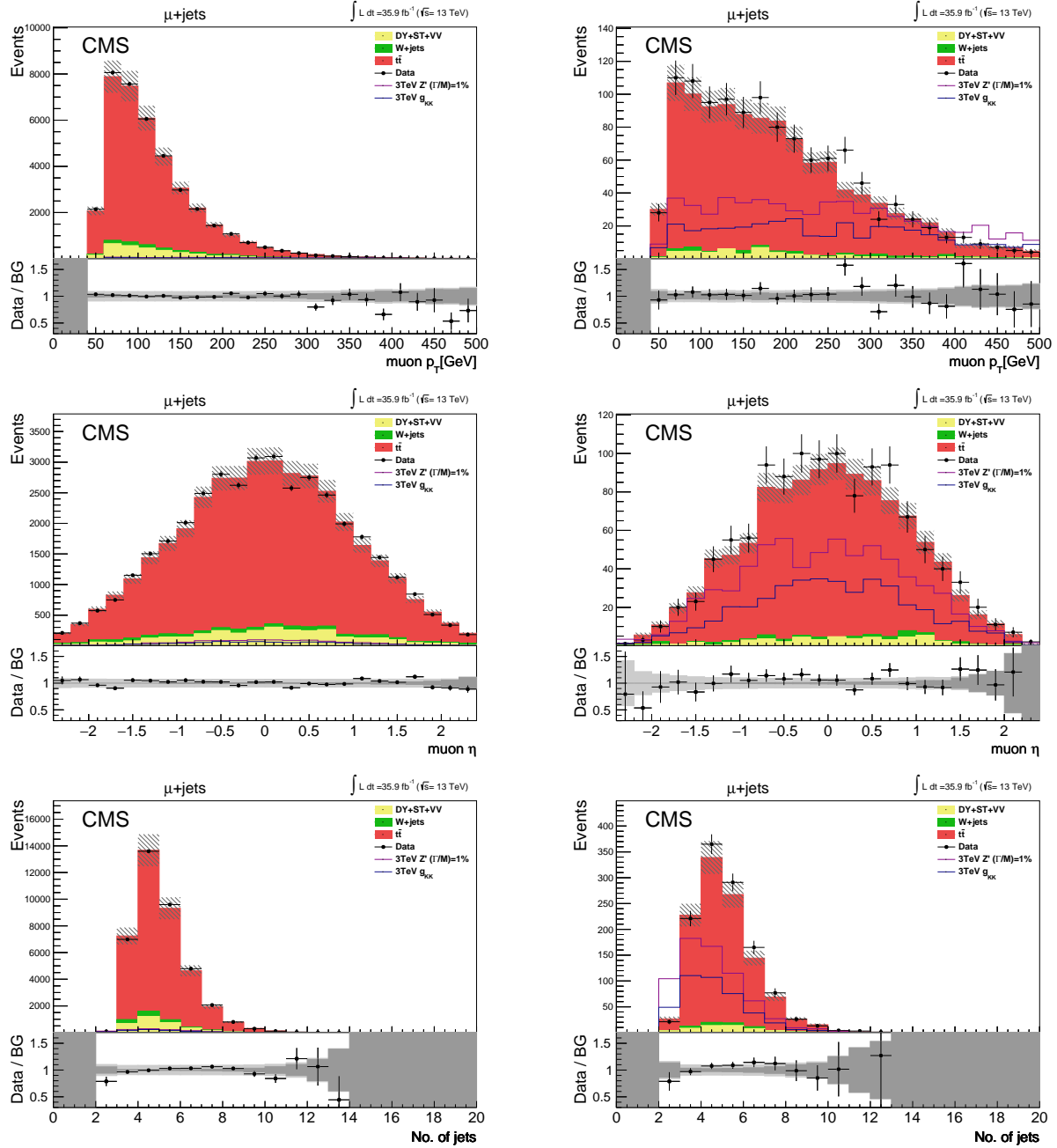


Figure B.1: Data/MC comparison of for events passing the baseline selection, after cutting on the χ^2_{tt} and BDT discriminators. Distributions are shown separately the 0T category (left) and 1T category on the right. The background distributions are obtained from the MLE. The error associated to the background expectation includes the MC statistical uncertainty and post-fit uncertainties on the SM cross sections. The signal templates are normalized to a cross section of 1 pb.

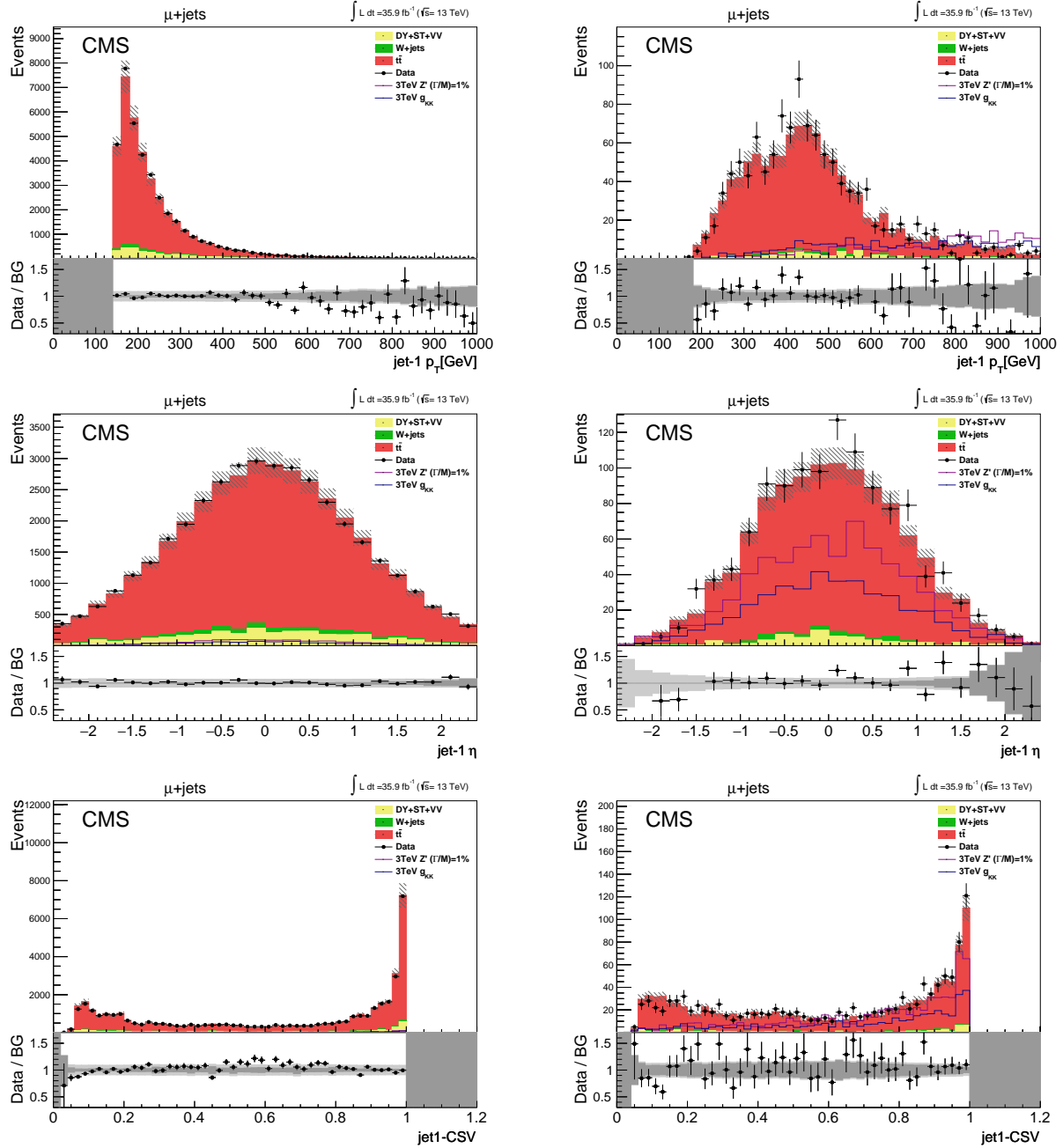


Figure B.2: Data/MC comparison of for events passing the baseline selection, after cutting on the $\chi^2_{t\bar{t}}$ and BDT discriminators. Distributions are shown separately the 0T category (left) and 1T category on the right. The background distributions are obtained from the MLE. The error associated to the background expectation includes the MC statistical uncertainty and post-fit uncertainties on the SM cross sections. The signal templates are normalized to a cross section of 1 pb.

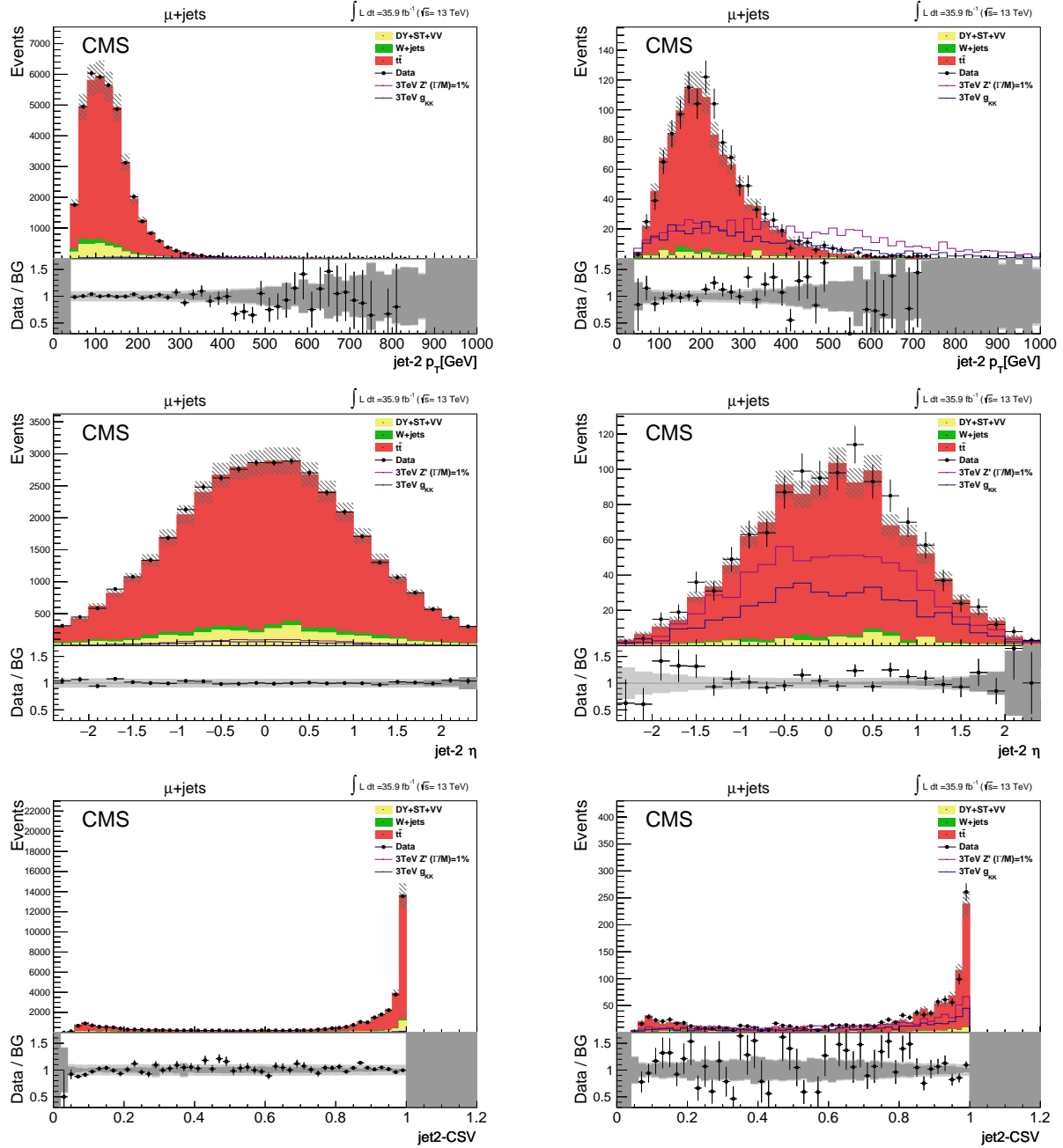


Figure B.3: Data/MC comparison of for events passing the baseline selection, after cutting on the $\chi^2_{t\bar{t}}$ and BDT discriminators. Distributions are shown separately the 0T category (left) and 1T category on the right. The background distributions are obtained from the MLE. The error associated to the background expectation includes the MC statistical uncertainty and post-fit uncertainties on the SM cross sections. The signal templates are normalized to a cross section of 1 pb.

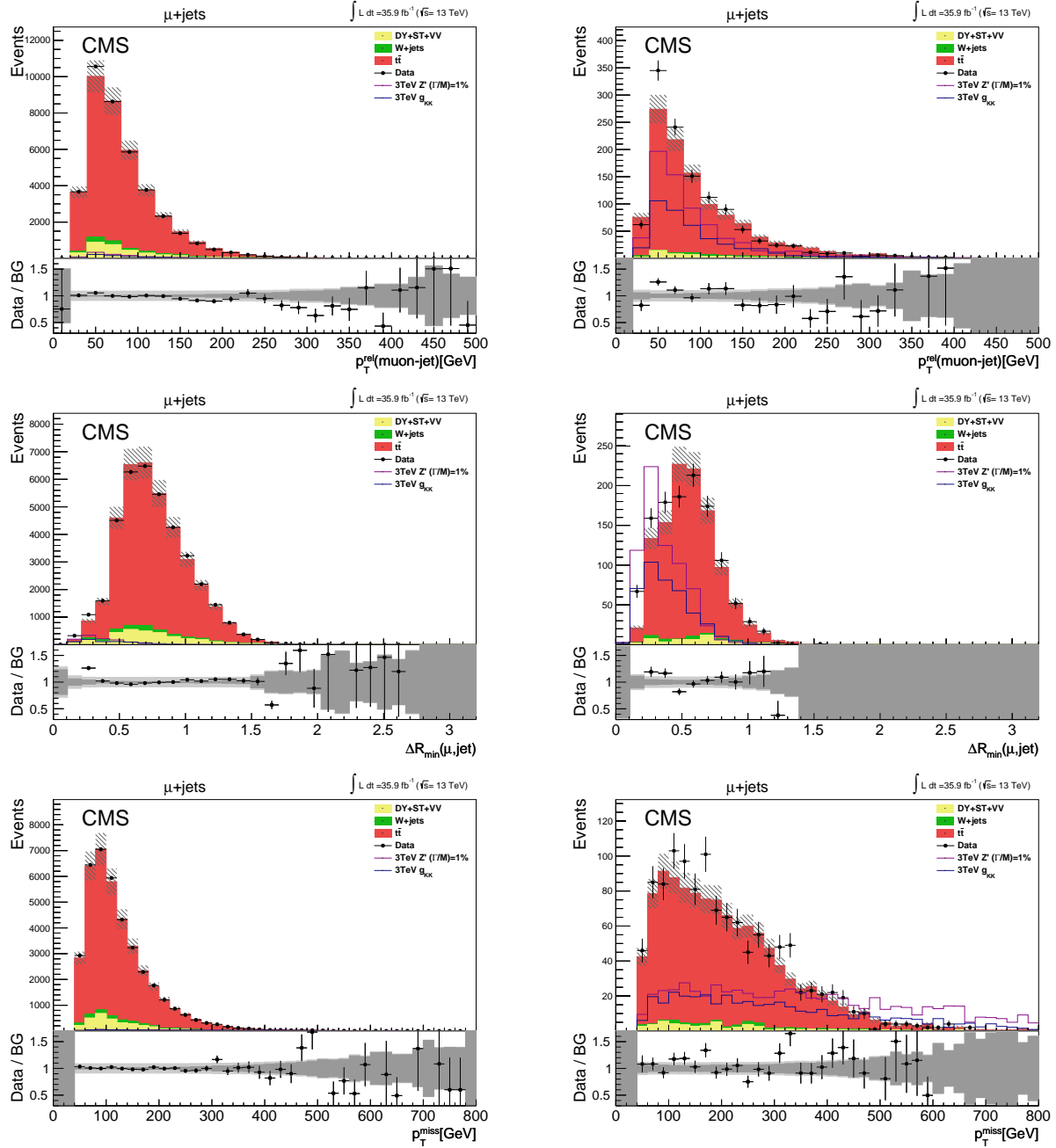


Figure B.4: Data/MC comparison of for events passing the baseline selection, after cutting on the χ^2_{tt} and BDT discriminators. Distributions are shown separately the 0T category (left) and 1T category on the right. The background distributions are obtained from the MLE. The error associated to the background expectation includes the MC statistical uncertainty and post-fit uncertainties on the SM cross sections. The signal templates are normalized to a cross section of 1 pb.

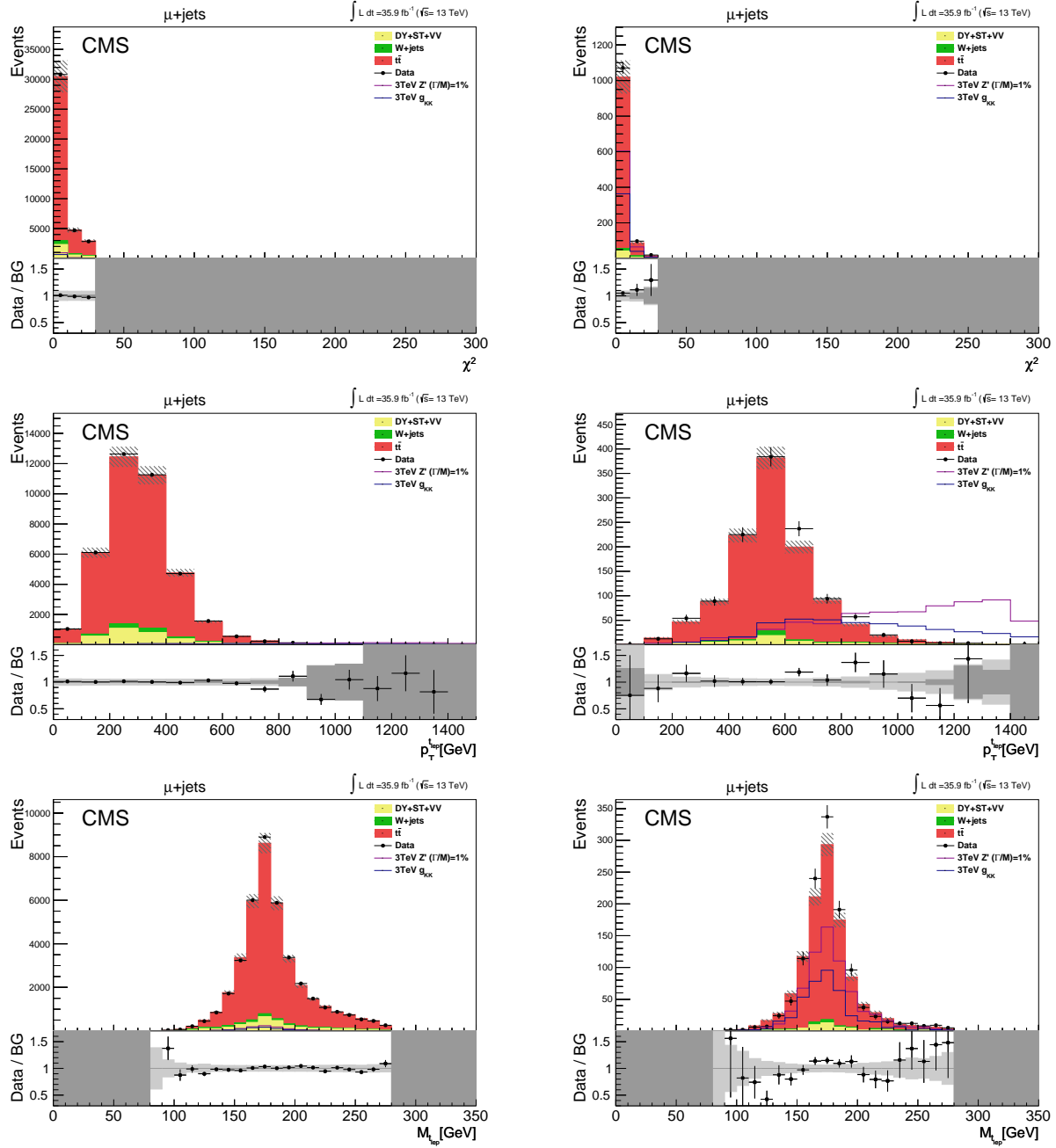


Figure B.5: Data/MC comparison of for events passing the baseline selection, after cutting on the χ^2_{tt} and BDT discriminators. Distributions are shown separately the 0T category (left) and 1T category on the right. The background distributions are obtained from the MLE. The error associated to the background expectation includes the MC statistical uncertainty and post-fit uncertainties on the SM cross sections. The signal templates are normalized to a cross section of 1 pb.

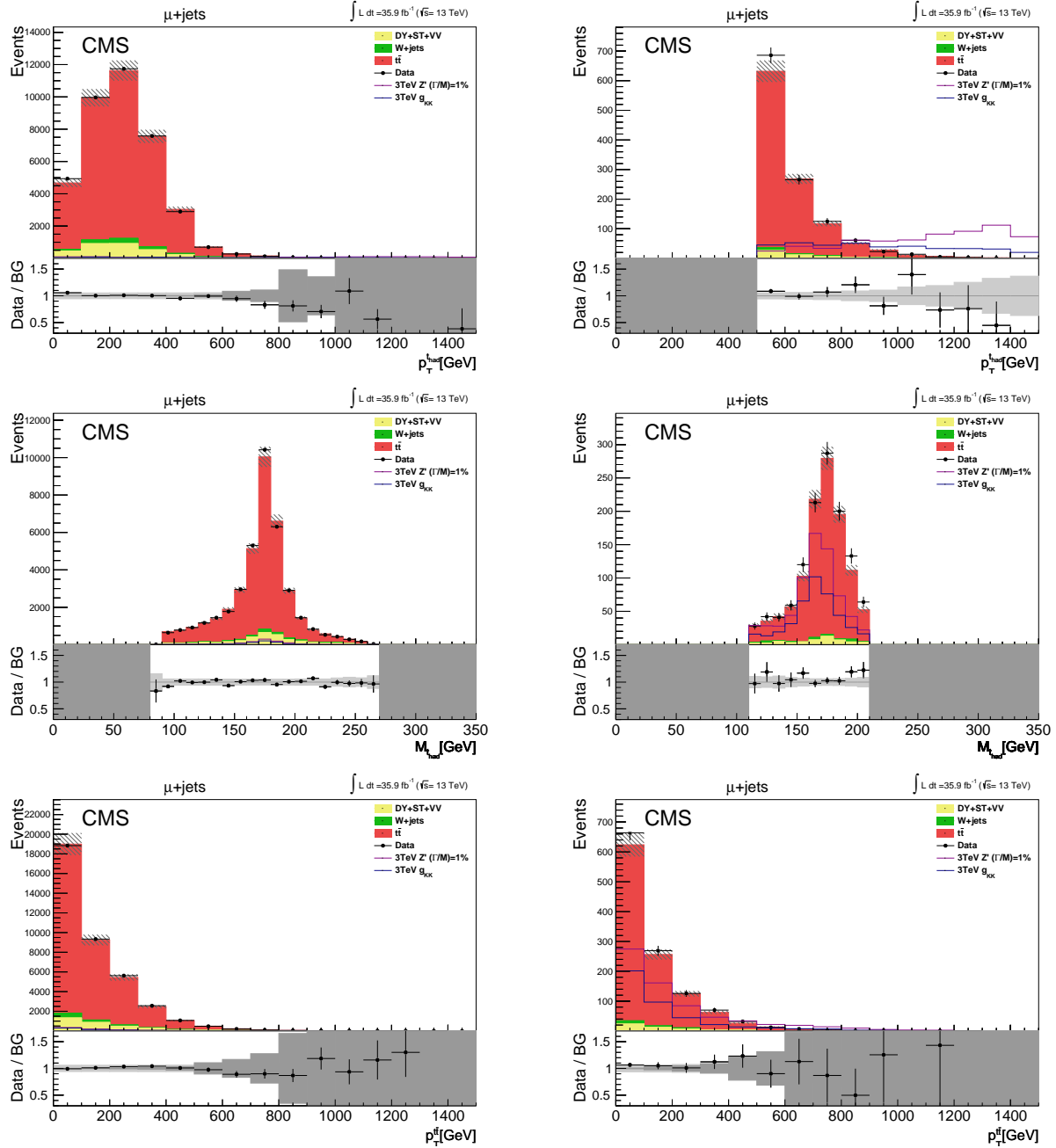


Figure B.6: Data/MC comparison of for events passing the baseline selection, after cutting on the χ^2_{tt} and BDT discriminators. Distributions are shown separately the 0T category (left) and 1T category on the right. The background distributions are obtained from the MLE. The error associated to the background expectation includes the MC statistical uncertainty and post-fit uncertainties on the SM cross sections. The signal templates are normalized to a cross section of 1 pb.

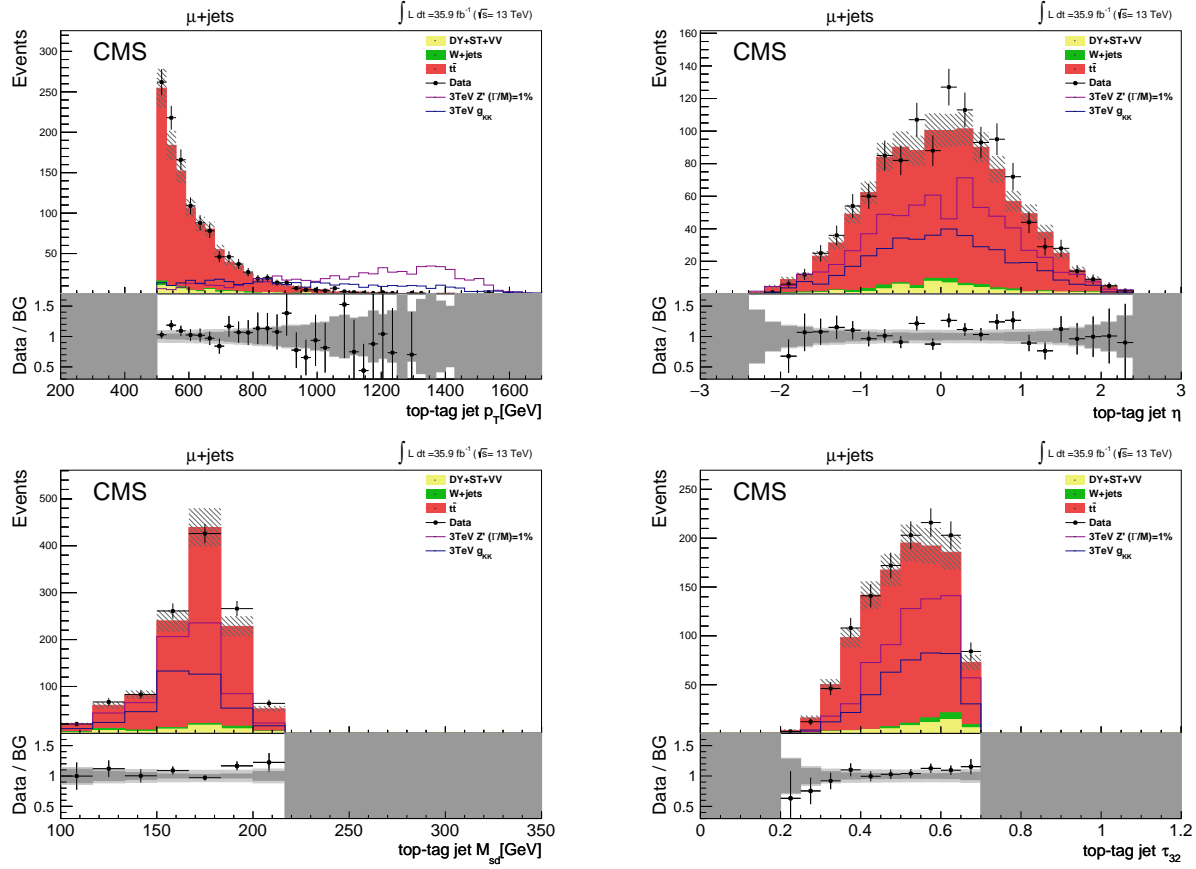


Figure B.7: Data/MC comparison of for events passing the baseline selection, after cutting on the $\chi^2_{t\bar{t}}$ and BDT discriminators. Distributions relevant to the T1 category are shown. The background distributions are obtained from the MLE. The error associated to the background expectation includes the MC statistical uncertainty and post-fit uncertainties on the SM cross sections. The signal templates are normalized to a cross section of 1 pb.

C. SYSTEMATIC UNCERTAINTY TEMPLATES

In this appendix we show the templates used to model the $\pm 1\sigma$ variation of the systematic uncertainties.

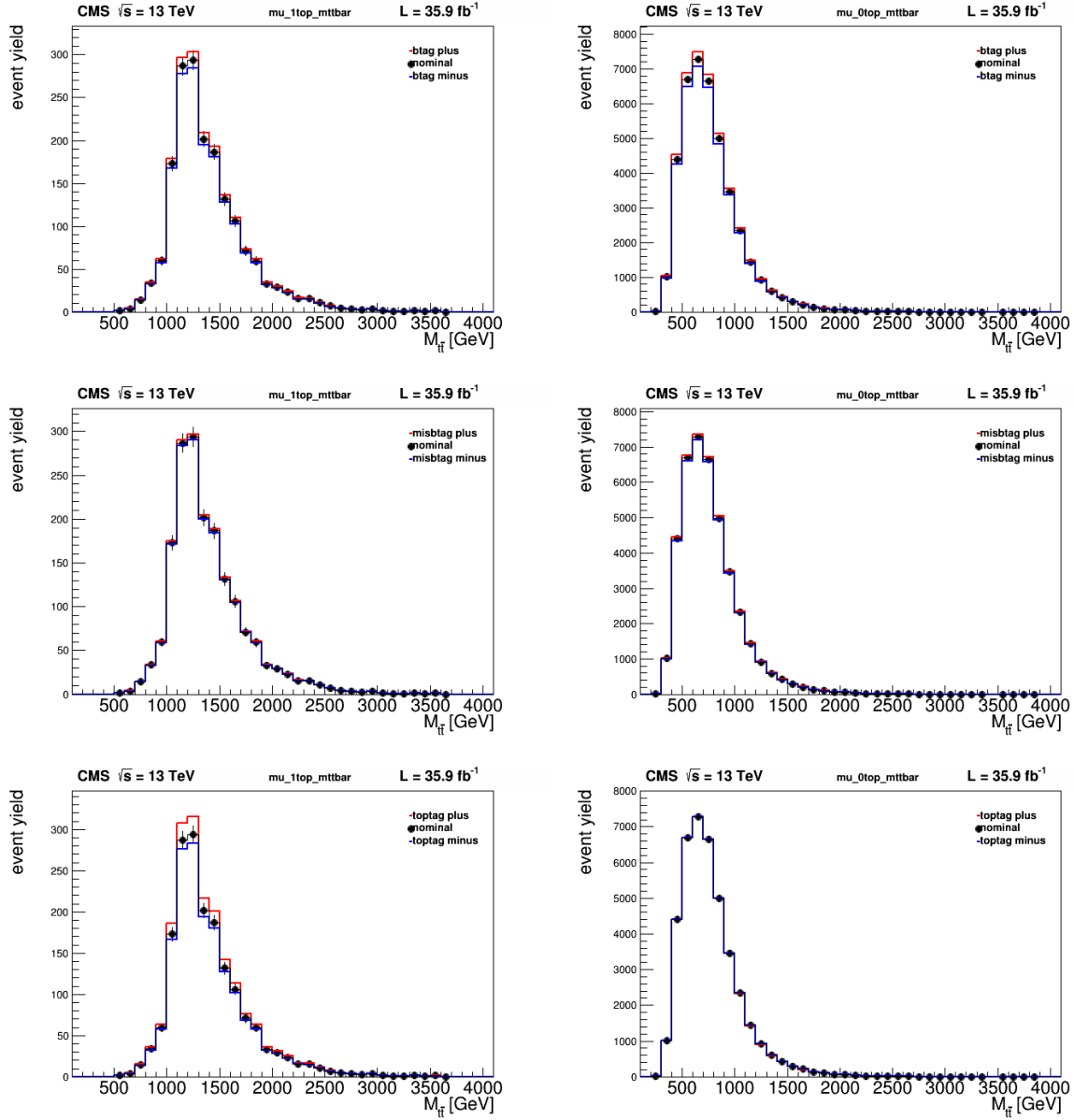


Figure C.1: $\pm 1\sigma$ systematic variation on the $M_{t\bar{t}}$ distribution in $t\bar{t}$ MC events. Plots are shown for the two final categories in the muon channel: 1T on the left and 0T on the right. The nominal distribution (black line) is plotted with its statistical uncertainty, the $+1\sigma$ shift up (red) and -1σ shift down (blue) templates account for differences in both shape and normalization with respect to the nominal sample.

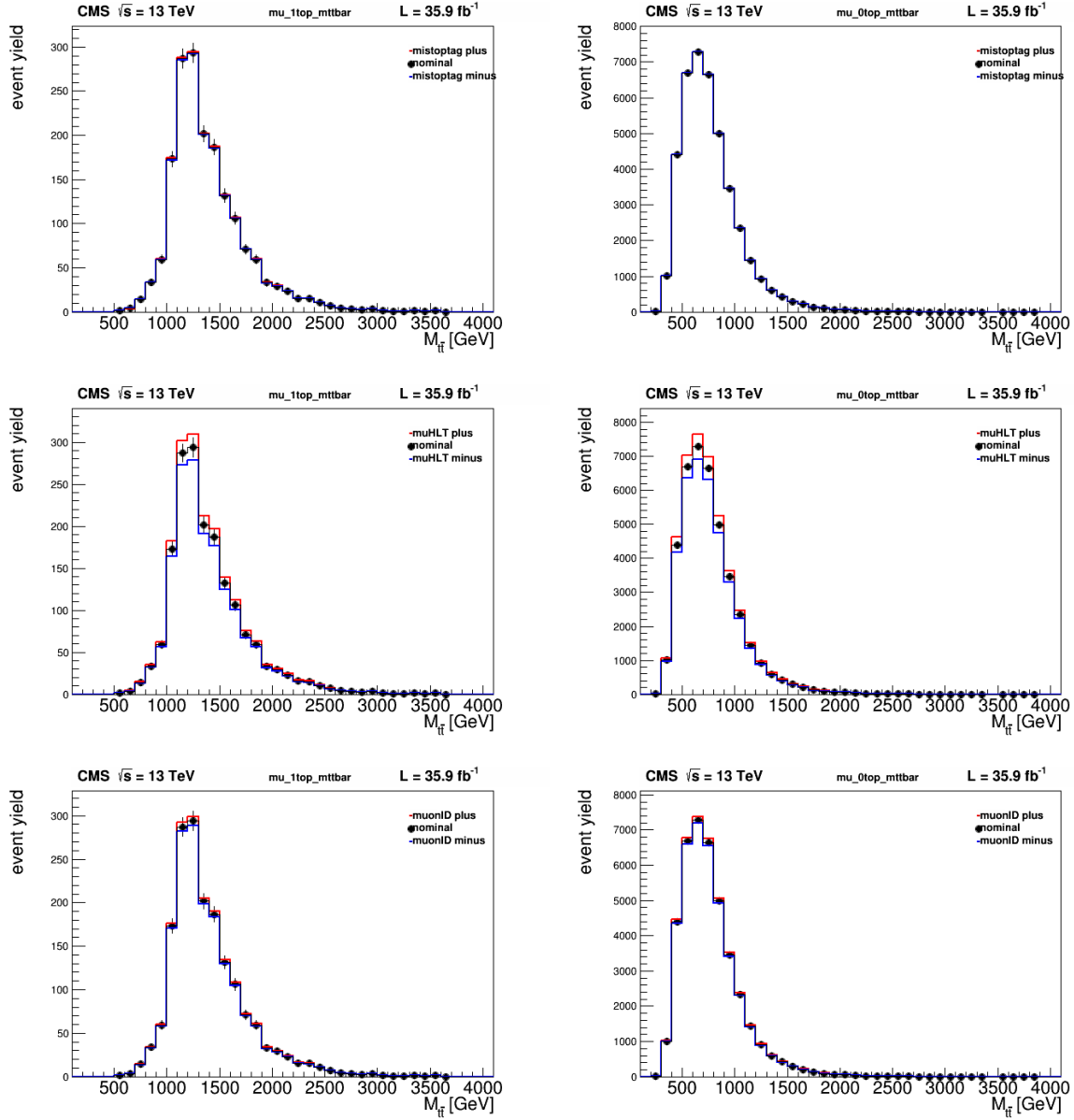


Figure C.2: $\pm 1\sigma$ systematic variation on the $M_{t\bar{t}}$ distribution in $t\bar{t}$ MC events. Plots are shown for the two final categories in the muon channel: 1T on the left and 0T on the right. The nominal distribution (black line) is plotted with its statistical uncertainty, the $+1\sigma$ shift up (red) and -1σ shift down (blue) templates account for differences in both shape and normalization with respect to the nominal sample.

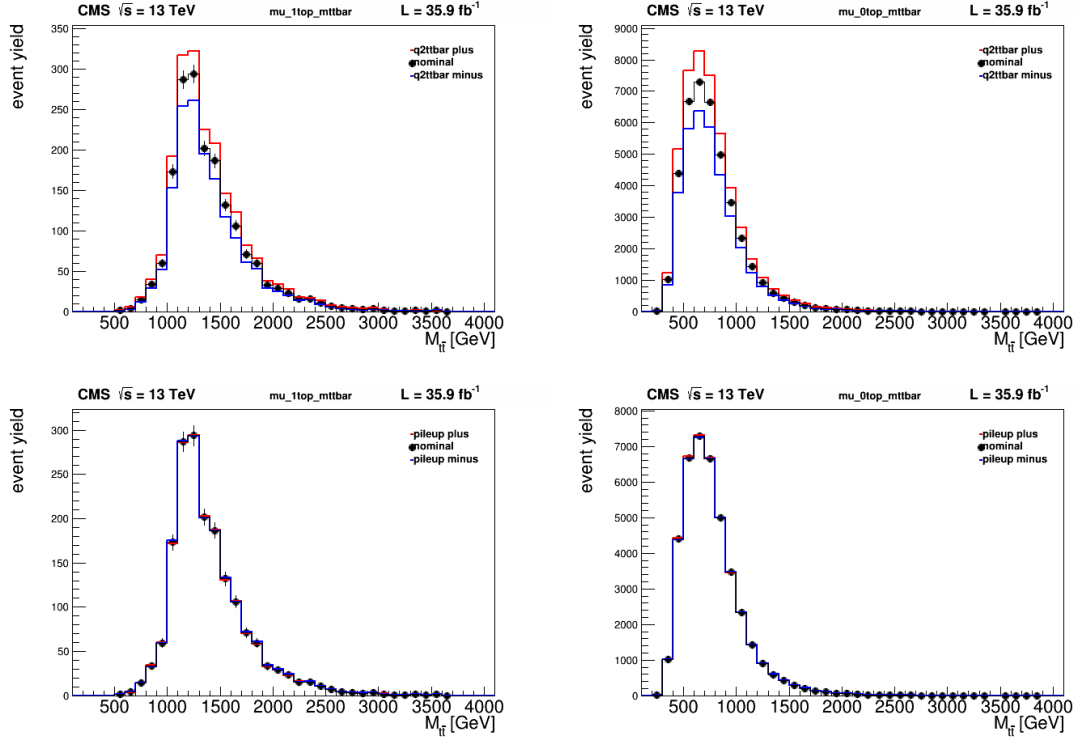


Figure C.3: $\pm 1\sigma$ systematic variation on the $M_{t\bar{t}}$ distribution in $t\bar{t}$ MC events. Plots are shown for the two final categories in the muon channel: 1T on the left and 0T on the right. The nominal distribution (black line) is plotted with its statistical uncertainty, the $+1\sigma$ shift up (red) and -1σ shift down (blue) templates account for differences in both shape and normalization with respect to the nominal sample.

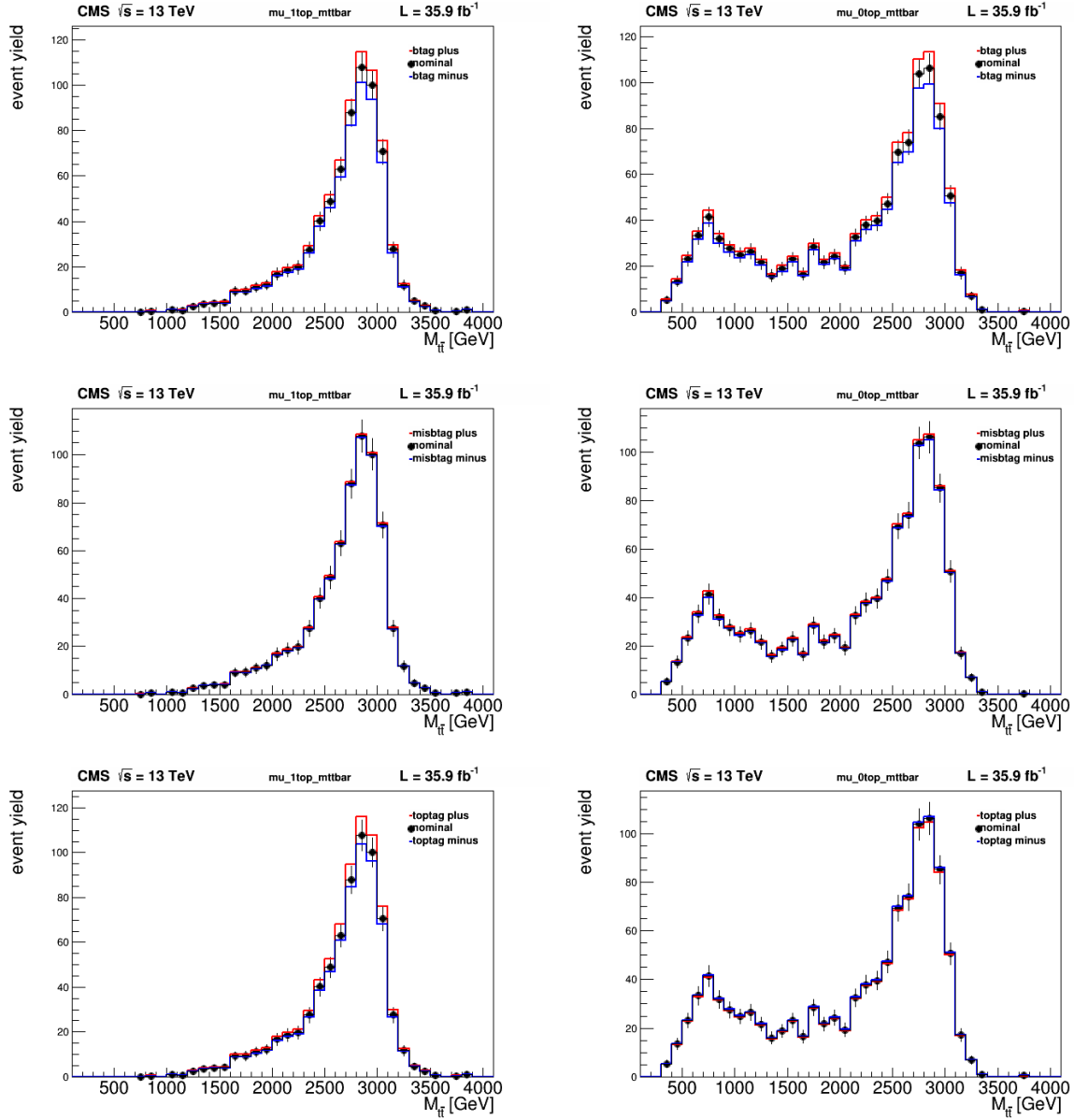


Figure C.4: $\pm 1\sigma$ systematic variation on the $M_{t\bar{t}}$ distribution in a narrow 3 TeV Z' MC sample. Plots are shown for the two final categories in the muon channel: 1T on the left and 0T on the right. The nominal distribution (black line) is plotted with its statistical uncertainty, the $+1\sigma$ shift up (red) and -1σ shift down (blue) templates account for differences in both shape and normalization with respect to the nominal sample.

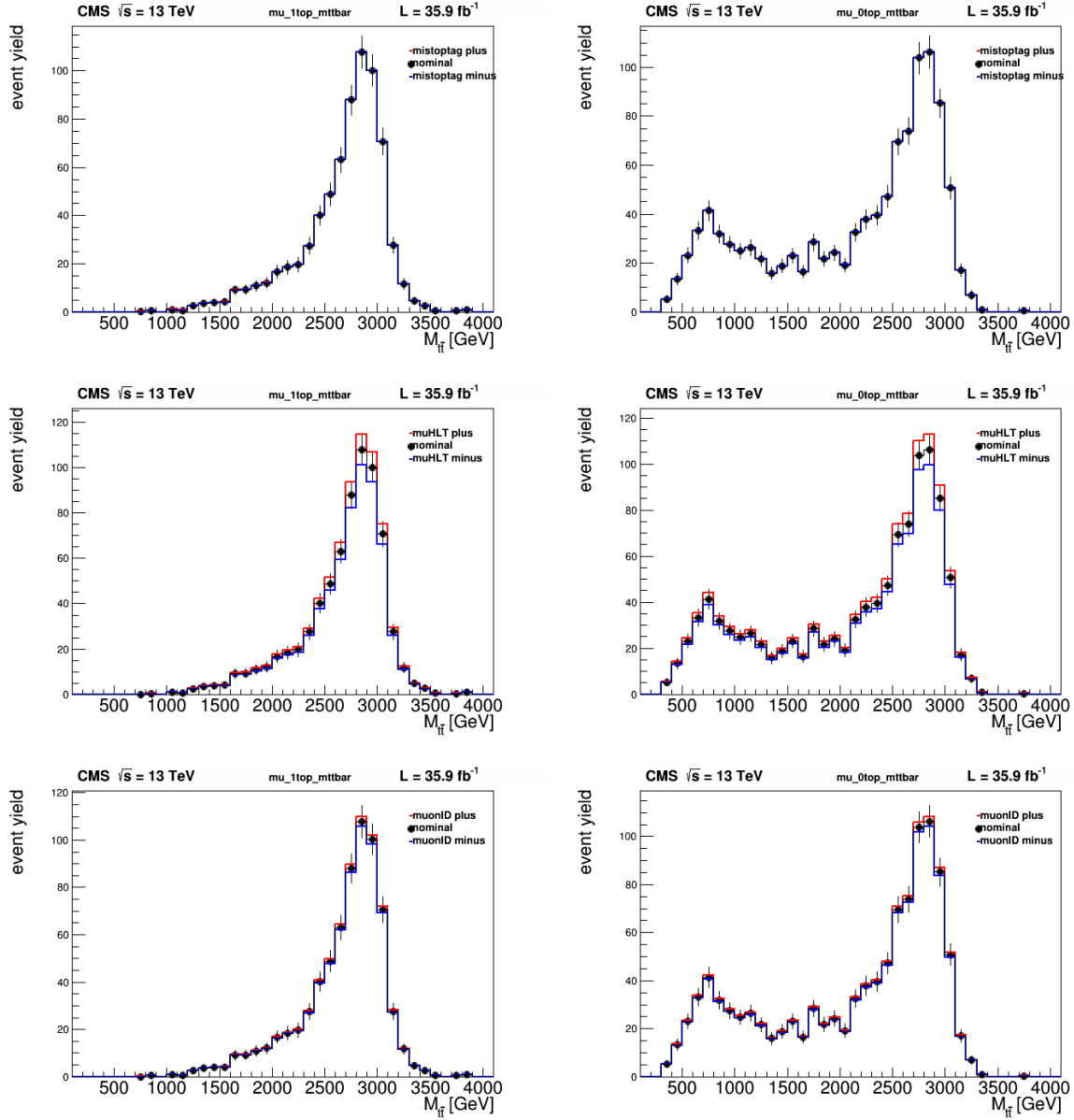


Figure C.5: $\pm 1\sigma$ systematic variation on the $M_{t\bar{t}}$ distribution in a narrow 3 TeV Z' MC sample. Plots are shown for the two final categories in the muon channel: 1T on the left and 0T on the right. The nominal distribution (black line) is plotted with its statistical uncertainty, the $+1\sigma$ shift up (red) and -1σ shift down (blue) templates account for differences in both shape and normalization with respect to the nominal sample.

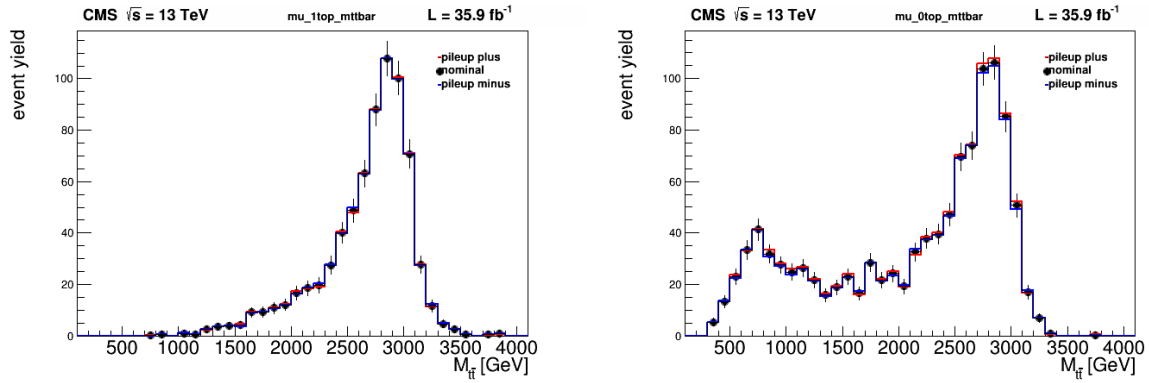


Figure C.6: $\pm 1\sigma$ systematic variation on the $M_{t\bar{t}}$ distribution in a narrow 3 TeV Z' MC sample. Plots are shown for the two final categories in the muon channel: 1T on the left and 0T on the right. The nominal distribution (black line) is plotted with its statistical uncertainty, the $+1\sigma$ shift up (red) and -1σ shift down (blue) templates account for differences in both shape and normalization with respect to the nominal sample.

CITED LITERATURE

- [1] Dodd, J.E. The ideas of particle physics. An introduction to scientists. *Cambridge University Press*, 1984.
- [2] Halzen, F. and Martin, A. D. Quarks and Leptons: An Introductory Course in Modern Particle Physics. *Wiley*, 1984.
- [3] Glashow, S.L. Partial Symmetries of Weak Interactions. *Nucl. Phys.*, 22:579–588, 1961.
- [4] Weinberg, S. A Model of Leptons. *Phys. Rev. Lett.*, 19:1264–1266, 1967.
- [5] Callan, Jr., Curtis, G., Dashen, R., and Gross, D. Toward a Theory of the Strong Interactions. *Phys. Rev. D*, 17:2717, 1978.
- [6] Politzer, H. D. Asymptotic Freedom: An Approach to Strong Interactions. *Phys. Rept.*, 14:129–180, 1974.
- [7] Wilczek, F. Quantum field theory. *Rev. Mod. Phys.*, 71:S85–S95, 1999.
- [8] Noether, E. Invariant Variation Problems. *Gott. Nachr.*, 1918:235–257, 1918.
- [9] Feynman, R. P. A relativistic cut-off for classical electrodynamics. *Phys. Rev. Lett.*, 74:939–946, 1948.
- [10] Aitchison, I. J. R. and Hey, A. J. *Gauge Theories in Particle Physics: A Practical Introduction*. 1989.
- [11] Altarelli, G. Collider Physics within the Standard Model: a Primer. *CERN-PH-TH-2013-020*, 2013.
- [12] Higgs, P. W. Broken symmetries and the masses of gauge bosons. *Phys. Rev. Lett.*, 13:508–509, 1964.
- [13] Englert, F., and Brout, R. Broken symmetry and the mass of gauge vector mesons. *Phys. Rev. Lett.*, 13:321, 1964.
- [14] Cabibbo, N. Unitary symmetry and leptonic decays. *Phys. Rev. Lett.*, 10:531, 1963.
- [15] Kobayashi, M. and Maskawa, T. Cp violation in the renormalizable theory of weak interaction.

- [16] ScienceNode. A standard infographic of the SM. Wikimedia Commons, Apr 2014. https://sciencenode.org/img/Standard_model_infographic.png.
- [17] ATLAS Collaboration. Observation of a new particle in the search for the Standard Model Higgs boson with the ATLAS detector at the LHC. *Phys. Lett. B.*, 716:1–29, 2012.
- [18] CMS Collaboration. Observation of a new boson at a mass of 125 GeV with the CMS experiment at the LHC. *Phys. Lett. B.*, 716:30–61, 2012.
- [19] ATLAS, CDF, CMS, and the D0 Collaborations. First combination of Tevatron and LHC measurements of the top-quark mass. *arXiv:1403.4427*, 2014.
- [20] Dicus, D., Stange, A., and Willenbrock, S. Higgs decay to top quarks at hadron colliders. *Phys. Lett. B.*, 333:126 – 131, 1994.
- [21] Rosner, J. L. Prominent decay modes of a leptophobic Z' . *Phys. Lett. B.*, 387:113 – 117, 1996.
- [22] Lynch, K. R., Simmons, E. H., Narain, M., and Mrenna, S. Finding Z' bosons coupled preferentially to the third family at LEP and the Tevatron. *Phys. Rev. D.*, 63:035006, 2001.
- [23] Agashe, K., Belyaev, A., Krupovnickas, T. Perez, G., and Virzi, J. LHC Signals from Warped Extra Dimensions. *Phys. Rev. D.*, 77:015003, 2008.
- [24] Davoudiasl, H., Hewett, J. L., and Rizzo, T. G. Phenomenology of the randall-sundrum gauge hierarchy model. *Phys. Rev. Lett.*, 84:2080–2083, 2000.
- [25] Frampton, P.H, and Glashow, S.L. Chiral color: An alternative to the standard model. *Phys. Lett. B.*, 190:157 – 161, 1987.
- [26] CMS Collaboration. Search for $t\bar{t}$ resonances in highly-boosted lepton+jets and fully hadronic final states in proton-proton collisions at $\sqrt{s} = 13$ TeV. *JHEP*, 07:001, 2017.
- [27] ATLAS Collaboration. A search for $t\bar{t}$ resonances using lepton-plus-jets events in proton-proton collisions at $\sqrt{s} = 8$ TeV with the ATLAS detector. *JHEP*, 08:148, 2015.
- [28] Randall, L., and Sundrum, R. Large mass hierarchy from a small extra dimension. *Phys. Rev. Lett.*, 83:3370–3373, 1999.
- [29] Tanedo, P.
<https://www.classe.cornell.edu/~pt267/images/illustrations/RSBrane.png>, 2012.
- [30] K. Agashe et al. LHC Signals from Warped Extra Dimensions. *Phys. Rev. D.*, 77:015003, 2008.
- [31] Dimopoulos, S., and Susskind, L. Mass Without Scalars. *Nucl. Phys. B*, 155, 1979.

- [32] Susskind, L. Dynamics of Spontaneous Symmetry Breaking in the Weinberg-Salam Theory. *Phys. Rev. D*, 20:2619, 1979.
- [33] Dugan, M., Georgi, H., and Kaplan, D. Anatomy of a Composite Higgs Model. *Nucl. Phys. B*, 254:299, 1985.
- [34] Hill, C. T. Topcolor assisted technicolor. *Phys. Lett. B*, 345:483–489, 1995.
- [35] Harris, R. M., Hill, C. T., and Parke, S.J. Cross-section for topcolor Z-prime decaying to t anti- t : Version 2.6. *FERMILAB-FN-0687*, 1999.
- [36] Greiner, N., Kong, K., Park, J., Park, S. C., and Winter, J. Model-Independent Production of a Top-Philic Resonance at the LHC. *JHEP*, 04:029, 2015.
- [37] Höche, S. Introduction to parton-shower event generators. 2014.
- [38] Salam, G. P. Elements of QCD for hadron colliders. *High-energy physics. Proceedings, 17th European School*, 2010.
- [39] Particle Data Group. 2016 Review of Particle Physics. *Chin. Phys.*, C40(10), 2016.
- [40] Campbell, J.M., Huston, J. W., and Stirling, W. J. Hard Interactions of Quarks and Gluons: A Primer for LHC Physics. *Rept. Prog. Phys.*, 70:89, 2007.
- [41] Webber, B. R. Fragmentation and hadronization. *Int. J. Mod. Phys.*, A15S1:577–606, 2000.
- [42] Evans, L. and Bryant, P. LHC Machine. *JINST*, 3:S08001, 2008.
- [43] Haffner, J. The CERN accelerator complex. *Complexe des accélérateurs du CERN.* , 2013.
- [44] CMS Collaboration. The CMS experiment at the CERN LHC. *JINST*, 3:S08004. 361, 2008.
- [45] ATLAS Collaboration. The ATLAS Experiment at the CERN Large Hadron Collider. *JINST*, 3:S08003, 2008.
- [46] CMS Collaboration. Tracker Technical Design Report. *CERN-LHCC-98-06, CMS-TDR-5*, 1998.
- [47] CMS Collaboration. The Electromagnetic Calorimeter Technical Design Report. *CERN-LHCC-97-33, CMS-TDR-4*, 1997.
- [48] CMS Collaboration. The Hadron Calorimeter Technical Design Report. *CERN-LHCC-97-31*, 1997.
- [49] CMS Collaboration. Muon Technical Design Report. *CERN-LHCC-97-32*, 1997.
- [50] CMS Collaboration. The CMS trigger system. *JINST*, 12, 2017.

- [51] Cadamuro, L. The CMS Level-1 trigger system for LHC Run II. *JINST*, 12, 2017.
- [52] CMS Collaboration. The upgrade of the CMS Global Trigger. *JINST*, 11:C02029, 2016.
- [53] V. Gori. The CMS high level trigger. *International Journal of Modern Physics: Conference Series*, 31:1460297, 2014.
- [54] Beaudette, F. The CMS Particle Flow Algorithm. In *Proceedings, International Conference on Calorimetry for the High Energy Frontier (CHEF 2013)*, pages 295–304, 2013.
- [55] CMS Collaboration. Description and performance of track and primary-vertex reconstruction with the CMS tracker. *JINST*, 9, 2014.
- [56] Adam, W., Mangano, B., Speer, T., and Todorov, T. Track reconstruction in the CMS tracker. *CERN-CMS-NOTE-2006-041*, 2005.
- [57] Fruhwirth, R. Application of kalman filtering to track and vertex fitting. *Nucl. Instrum. Meth.*, A262:444–450, 1987.
- [58] CMS Collaboration. Particle-Flow Event Reconstruction in CMS and Performance for Jets, Taus, and MET. *CMS-PAS-PFT-09-001*, 2009.
- [59] Adam, W., and Frhwirth, R., Strandlie, A., and Todorov, T. Reconstruction of Electrons with the Gaussian-Sum Filter in the CMS Tracker at the LHC. *CMS-NOTE-2005-001*, 2005.
- [60] Cacciari, M., Salam, G. P., and Soyez, G. The Anti-k(t) jet clustering algorithm. *JHEP*, 04:063, 2008.
- [61] CMS Collaboration. Summaries of CMS cross section measurements. <https://twiki.cern.ch/twiki/bin/view/CMSPublic/PhysicsResultsCombined>.
- [62] Nason, P. A new method for combining NLO QCD with shower Monte Carlo algorithms. *JHEP*, 11:040, 2004.
- [63] Frixione, S., Nason, P., and Oleari, C. Matching NLO QCD computations with Parton Shower simulations: the POWHEG method. *JHEP*, 11:070, 2007.
- [64] Alwall, J., Frederix, R., Frixione, S., Hirschi, V., Maltoni, F., Mattelaer, O., Shao, H. S., Stelzer, T., Torrielli, P., and Zaro, M. The automated computation of tree-level and next-to-leading order differential cross sections, and their matching to parton shower simulations. *JHEP*, 07:079, 2014.
- [65] Sjöstrand T., Mrenna S., and Skands P. A Brief Introduction to PYTHIA 8.1. *Comput. Phys. Commun.*, 178, 2008.
- [66] CMS Collaboration. <http://cms-sw.github.io/>.

- [67] GEANT4 Collaboration. Geant4 — a simulation toolkit. *Nucl. Instrum. Meth. A*, 506:250, 2003.
- [68] NNPDF Collaboration. Parton distributions for the LHC Run II. *JHEP*, 04:040, 2015.
- [69] Amsler, C. Review of particle physics. *Phys. Lett. B.*, 667, 2008.
- [70] Sjöstrand, T. .
<http://home.thep.lu.se/~torbjorn/pythia81html/ExtraDimensionalProcesses.html>.
- [71] Bonciani, R., Jezo, T., Klasen, M., Lyonnet, F., and Schienbein, I. Electroweak top-quark pair production at the LHC with Z' bosons to NLO QCD in POWHEG. *JHEP*, 02:141, 2016.
- [72] R. M. Harris and S. Jain. Cross sections for leptophobic topcolor Z' decaying to top-antitop. *Eur. Phys. J. C*, 72:2072, 2012.
- [73] Gao, J., Li, C. S., Li, B. H., Yuan, C.P., and Zhu, H. X. Next-to-leading order QCD corrections to the heavy resonance production and decay into top quark pair at the LHC. *Phys. Rev. D.*, 82:014020, 2010.
- [74] Chabanat, E and Estre, N. Deterministic Annealing for Vertex Finding at CMS. 2005.
- [75] CMS Collaboration. Identification of b-quark jets with the CMS experiment. *JINST*, 8:P04013, 2013.
- [76] CMS Collaboration. Identification of b quark jets at the CMS Experiment in the LHC Run 2. *CMS-PAS-BTV-15-001*, 2016.
- [77] Larkoski, A. J., Marzani, S., and Soyez, G., and Thaler, J. Soft Drop. *JHEP*, 05:146, 2014.
- [78] Thaler, J. and Van Tilburg, K. Identifying Boosted Objects with N-subjettiness. *JHEP*, 03:015, 2011.
- [79] Y. Freund and R. E. Schapire. Experiments with a new boosting algorithm.
- [80] Hoecker, A., Speckmayer, P., Stelzer, J., Therhaag, J., Von Toerne, E., and Voss, H. TMVA: Toolkit for Multivariate Data Analysis. *PoS, ACAT*:040, 2007.
- [81] Pedregosa, F., Varoquaux, G., Gramfort, A., Michel, V., Thirion, B., Grisel, O., Blondel, M., Prettenhofer, P., Weiss, R., Dubourg, V., Vanderplas, J., Passos, A., Cournapeau, D., Brucher, M., Perrot, M., and Duchesnay, E. Scikit-learn: Machine learning in Python. *Journal of Machine Learning Research*, 12:2825–2830, 2011.
- [82] M.A. Stephens. Edf statistics for goodness of fit and some comparisons. *Journal of the American Statistical Association*, 69(347):730–737, 1974.
- [83] The PDF4LHC Working Group. The PDF4LHC Working Group Interim Report. 2011.

- [84] Barlow, R. J. and Beeston, C. Fitting using finite Monte Carlo samples.
Comput.Phys.Commun., 77(MAN-HEP-93-1):219–228, 1993.
- [85] Conway, J. Nuisance Parameters in Likelihoods for Searches. Presentation at
PhyStat 2011, 2011.
- [86] Ott, J. Theta-auto testing documentation.
<http://www-ekp.physik.uni-karlsruhe.de/~ott/theta/theta-auto/>.

VITA

Name	Irving Daniel Sandoval Gonzalez
Education	Ph.D., Physics University of Illinois at Chicago, Chicago, Illinois 2017 B.S., Physics and Mathematics with Minor in Nuclear Engineering Instituto Politecnico Nacional, Mexico City, Mexico 2011
Experience	Research Assistant (CMS Experiment) University of Illinois at Chicago, USA 2012 – 2017 NSF PIRE Program, Summer Research Abroad ETH Zürich 2013 Teaching Assistant University of Illinois at Chicago, USA 2012 Summer Internship Fermi National Laboratory, USA 2010
Publications	CMS Collaboration, “Search for $t\bar{t}$ resonances in highly-boosted lepton+jets and fully hadronic final states in proton-proton collisions at $\sqrt{s} = 13$ TeV” arXiv:1704.03366, 2017. CMS Collaboration, “Search for resonant $t\bar{t}$ production in proton-proton collisions at $\sqrt{s}=8$ TeV” Phys. Rev. D., 93:012001, 2016. CMS Collaboration, “Search for $t\bar{t}$ resonances in all-hadronic and semileptonic final states in pp collisions at $\sqrt{s} = 8$ TeV” Phys. Rev. Lett., 111(21):211804, 2013.

Presentations	<p>“Qualification of the modules for the upgrade of the CMS FPIX detector” American Physical Society April Meeting, Washington D.C., USA 2017</p> <p>“Overview of the Compact Muon Solenoid Phase 1 Forward Pixel Upgrade” 38th International Conference on High Energy Physics, Chicago, USA 2016</p> <p>“Search for resonant $t\bar{t}$ production with the CMS experiment” Lake Louise Winter School, Lake Louise, Canada 2016</p> <p>“Search for top-antitop quark resonances” US LHC Association Meeting, Fermi National Laboratory, USA 2015</p> <p>“Search for $t\bar{t}$ resonances at CMS” Phenomenology Symposium, Pittsburgh, USA 2015</p> <p>“Search for $t\bar{t}$ resonances in semileptonic final states in pp collisions at $\sqrt{s} = 8$ TeV” American Physical Society April Meeting, Savannah, USA 2014</p>
	<p>Conference Proceedings I. Sandoval, “Overview of the Compact Muon Solenoid Phase 1 Forward Pixel Upgrade” 38th International Conference on High Energy Physics</p>
	<p>Awards Travel Award American Physical Society Division of Particles and Fields 2017</p> <p>Travel Award Physics Department of the University of Illinois at Chicago 2016</p> <p>Travel Award American Physical Society Division of Particles and Fields 2014</p> <p>Academic Excellence Instituto Politecnico Nacional 2011</p>

Workshops

Data Science in High Energy Physics
Fermilab, USA, 2017
Participant

Machine Learning Hands-on Advanced Tutorial Session
Fermilab, USA, 2017
Participant

PyROOT Hands-on Advanced Tutorial Session
Fermilab, USA, 2017
Participant

Beyond 2 Generations Physics Analysis Group
Fermilab, USA, 2016
Participant

CMS Pixel Detector Phase 1 Upgrade
CERN, Switzerland, 2016
Participant

CMS Data Analysis School
Fermilab, USA, 2015
Facilitator

Beyond 2 Generations Physics Analysis Group
CERN, Switzerland, 2015
Participant

CMS Phase I Pixel Upgrade Workshop
Visegrad, Hungary, 2015
Participant

CTEQ QCD and Electroweak Phenomenology
University of Pittsburgh, USA, 2015
Participant

CMS Pixel Detector Phase 1 Upgrade
CERN, Switzerland, 2014
Participant

Hadron Collider Physics Summer School
Fermilab, USA, 2014
Participant

CMS Data Analysis School
Fermilab, USA, 2014
Participant

Jet Substructure Hands-on Advanced Tutorial Session
Fermilab, USA, 2014
Participant

Statistics Hands-on Advanced Tutorial Session
Fermilab, USA, 2014
Participant